For Reference

NOT TO BE TAKEN FROM THIS ROOM

Ex libris
UNIVERSITATIS
ALBERTAENSIS

QUAECUMQUE VERA
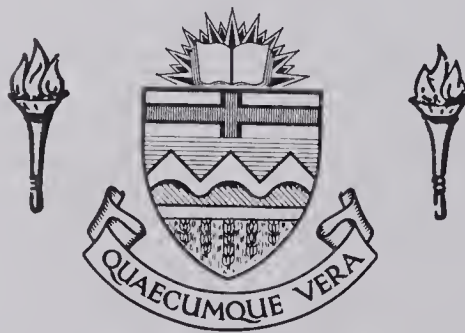
THE UNIVERSITY OF ALBERTA

POLARIZATION OF FAST NEUTRONS FROM ^{40}Ca(d,n)^{41}Sc

by

Dale Alan Gedcke

A THESIS

SUBMITTED TO THE FACULTY OF GRADUATE STUDIES

IN PARTIAL FULFILLMENT OF THE REQUIREMENTS FOR THE DEGREE

OF DOCTOR OF PHILOSOPHY

DEPARTMENT OF PHYSICS

EDMONTON, ALBERTA

September, 1967

UNIVERSITY OF ALBERTA

FACULTY OF GRADUATE STUDIES

The undersigned certify that they have read, and recommend to the
Faculty of Graduate Studies for acceptance, a thesis entitled POLARIZATION
OF FAST NEUTRONS FROM ^{40}Ca(d,n)^{41}Sc, submitted by Dale Alan Gedcke in
partial fulfillment of the requirements for the degree of Doctor of
Philosophy.

TABLE OF CONTENTS

LIST OF TABLES

LIST OF FIGURES

$\dagger$Page numbers refer to the page immediately preceding the figure and its caption.

ABSTRACT

Neutron polarizations were measured in the $^{40}Ca(d,n)^{41}Sc$ reaction
for neutron groups leading to the ground, 1.718 MeV, and 2.415 MeV
states of ^{41}Sc. The deuteron bombarding energy was 5.974 ± 0.039 MeV.
Polarization angular distributions were measured at 10° intervals from
a reaction angle of 0° to 120° (lab). This work was performed as part
of a cooperative project undertaken by several groups to study the
application of DWBA reaction theory to the reactions $^{40}Ca(d,d)^{40}Ca$,
$^{40}Ca(d,n)^{41}Sc$, and $^{40}Ca(d,p)^{41}Ca$ at identical deuteron bombarding
energies. DWBA stripping calculations have been compared to the polari-
zations measured in this part of the project, and to the differential
cross-sections for $^{40}Ca(d,n)^{41}Sc$ previously measured by another group.
The $^{40}Ca(d,n)^{41}Sc_{gnd}$ polarization and differential cross-section have
been interpreted to require a deuteron spin-orbit potential depth of
approximately 13 MeV.

A description of the neutron polarimeter developed for the measure-
ment of neutron polarizations in the energy range from 2 to 20 MeV is
given.

Recent advances in fast timing techniques with scintillation detectors
are discussed in detail.

ACKNOWLEDGMENTS

NOTATION

The following list gives some of the symbols used in the text in the order of their appearance.

d	Deuteron
n	Neutron
p	Proton
A	Target nucleus
B	Residual nucleus
x	Emitted particle
y	Captured particle
T	Transition amplitude
$\chi_d^{(+)}(\vec{k}_d, \vec{r}_d)$	Deuteron elastic scattering wave function in the incoming channel
$\chi_x^{(-)}(\vec{k}_x, \vec{r}_x)$	Elastic scattering wave function for the particle in the outgoing channel
V'	The interaction potential inducing the stripping reaction
$\vec{k}$	The momentum vector for a particle $\vec{k} = \vec{p}/\hbar$, where $\vec{p} = m\vec{v}$
$U(r)$	The general optical model potential
$U_c(r)$	The Coulomb potential
V	The depth of the real part of the optical potential
W	The depth of the imaginary part of the optical potential
$V_S \equiv V_{SO}$	The depth of the spin-orbit part of the optical potential
$\vec{L}$	The orbital angular momentum of a particle
$\vec{\sigma}$	The Pauli spin operator for a particle
$r_o = \dfrac{r}{A^{\frac{1}{3}}}$	The reduced radius of the optical potential

r	The radius of the optical potential
A	The mass number of the nucleus
Z	The number of protons in a nucleus
e	The charge on an electron
$f(r,r_o,a)$	The Saxon-Woods potential shape
V_{np}	The neutron-proton potential
ℓ	The orbital angular momentum of a particle
s	The spin of a particle
j	The total angular momentum of a particle
$A_{\ell sj}$	The spectroscopic coefficient
$\beta_{sj}^{\ell m m_x m_d}$	The reduced amplitude
J_A	The total angular momentum of the target nucleus A
M_A	The magnetic quantum number for J_A
$\left.\begin{array}{l} J_B \\ M_B \end{array}\right\}$	See J_A and M_A but for the residual nucleus B
$\psi_{J_B M_B}$	The wavefunction for the final nucleus B
$\psi_{J_A M_B}$	The wavefunction for the target nucleus A
$S_{\ell j}$	The spectroscopic factor
ψ_d	The deuteron wavefunction
$\phi_d(r_{np})$	The radial part of the deuteron wavefunction
$\dfrac{d\sigma(\theta)}{d\Omega}$	The differential cross-section for the reaction angle θ
$P_x(\theta)$	The polarization of the outgoing particles, x, at the reaction angle θ
Im	The imaginary part of . . .
Q	The energy required to balance the conservation of energy equation in a nuclear reaction.

R	The number of counts in the right detector
L	The number of counts in the left detector
$\varepsilon = \dfrac{R-L}{R+L}$	The asymmetry in the scattering of neutrons from the cryostat
A_{eff}	The effective analysing power of the polarimeter
t	Neutron flight time
S	Neutron flight path length
m_n	Neutron mass
$\left.\dfrac{\Delta E}{E}\right\|_{\Delta S}$	The relative energy resolution due to detector thickness ΔS
$\left.\dfrac{\Delta E}{E}\right\|_{\Delta t}$	The relative energy resolution due to the detector intrinsic time resolution Δt
DDL	Double delay line clipped
DL	Single delay line clipped
DCA	Dual channel analyser
TAC	Time-to-amplitude converter
ADC	Amplitude-to-digital converter
"Walk"	The systematic variation of the time at which pulses of different amplitudes cross a finite pulse height discriminator threshold.

CHAPTER 1

(d,n) AND (d,p) STRIPPING REACTIONS

1.1 Introduction

In the past few years the DWBA (distorted wave Born approximation) form of reaction theory has been subjected to increasingly close scrutiny. Comprehensive studies of direct interactions are becoming more feasible due to the amount of information currently available on the optical model description of neutron and proton elastic scattering. There is still a shortage of comprehensive data on deuteron elastic scattering. However, it is now possible to perform experiments which test the applicability of DWBA theory to (d,p) and (d,n) stripping reactions with a minimum of ambiguity in the results. Unfortunately, to minimize the ambiguity a great deal of correlated experimental data is required. In this laboratory several groups have cooperated in studying (d,d) elastic scattering, (d,n) and (d,p) stripping differential cross-sections, and polarizations in the exit channels of the (d,n) and (d,p) stripping reactions for a common target nucleus. By performing each of these experiments at the same deuteron bombarding energies a large amount of correlated data is provided. Since each set of experiments measures a different aspect of the interrelated reactions with the target nucleus the full complement of data places severe restrictions on the predictions that the DWBA theory must produce.

This thesis reports on the measurement of the neutron polarization in the ^{40}Ca(d,n)^{41}Sc reaction at a nominal deuteron bombarding energy of 6 MeV. The work was intended as a contribution to the study of the ^{40}Ca(d,d)^{40}Ca, ^{40}Ca(d,n)^{41}Sc, and ^{40}Ca(d,p)^{41}Ca reactions in cooperation with other groups in this laboratory (Gr 67, Le 68, Gr 67a, Le 67). Justification for this choice of reactions is given in section 1.4.

For the purpose of convenient reference a brief summary of the main features of the DWBA theory of stripping reactions is given below. Thorough development of this subject can be found in several articles (Sa 64, Bu 60, Bu 61, Au 63, Me 62). Therefore, the emphasis here will be on the basic assumptions and the application of the theory.

1.2 DWBA Theory of (d,n) and (d,p) Stripping Reactions

For generality let us represent (d,n) and (d,p) stripping reactions as A(d,x)B. Here A is the target nucleus bombarded by the deuteron. The outgoing particle, x, (either a neutron or a proton) leaves the residual nucleus B. B is formed by adding the captured particle, y, (a proton or a neutron respectively) to the target nucleus A. The two types of reaction can be treated identically, except that the Coulomb potential is dropped wherever the neutron is specifically involved.

The reaction represents a transition from the initial state described by the wave function |initial> to a final state |final>. |final> must describe the states of nucleus B and particle x, as well as the relative motion of B and x. Similarly, |initial> must define the states of A and the deuteron, as well as their relative motion.

Unfortunately, the A(d,x)B reaction is not the only possible transition.
In the incoming channel shape elastic scattering takes place, direct
reactions to other final states compete, and compound nucleus reactions
can produce sizeable transition amplitudes to the final channel of
interest as well as to other modes of decay. All of these reaction modes,
of course, have an effect on the wave functions describing the relative
motion of the bodies in the incoming and outgoing channels. An exact
calculation of the transition amplitude from the initial channel to the
final channel would have to take all these effects into account. The
solution would involve a detailed coupled channels calculation (Le 66).
The mathematical complexity of such an approach renders the technique
impractical in this case.

It is at this point that the Born approximation is invoked. If it
is found that in the incident channel the dominant interaction is
elastic scattering of the deuterons, then the other transitions can be
treated by a perturbation analysis. Similarly, if all other cross-sections
are small compared to' the elastic scattering cross-section when nucleus
B is bombarded by the particle x, then a perturbation treatment should
be a good approximation for the outgoing channel as well. In many
reactions studied to date it has been found that the elastic scattering
cross-section is large compared to competing modes of interaction. Thus
it is with some confidence that elastic scattering wave functions are
used to describe the relative two-body motions in the incident and exit
channels of stripping reactions. All other channels are ignored except

in so far as they can be represented by an absorption potential in the

elastic scattering. The validity of this Born approximation is, however,

not guaranteed in every case. Buck and Rook (Bu 65) have suggested that

ignoring the coupling to other reaction channels is a poor approximation

for reactions involving large momentum differences between the initial

and final states, or involving both strongly and weakly absorbed particles,

or involving large angular momentum transfer.

With this approach in mind the transition amplitude for the direct

reaction A(d,x)B is written as (Sa 64)

$$T = J \int d\vec{r}_d \int d\vec{r}_x \; \chi_x^{(-)*}(\vec{k}_x,\vec{r}_x) < B,x|V'|A,d > \chi_d^{(+)}(\vec{k}_d,\vec{r}_d) \tag{1.1}$$

where $\vec{r}_x$ is the displacement of x from B, and $\vec{r}_d$ is the displacement

of the deuteron from A. J is the Jacobian of the transformation to these

relative coordinates. The function $\chi_d^{(+)}(\vec{k}_d,\vec{r}_d)$ is the elastic scattering

wave function for the deuteron in the incoming channel with momentum

vector $\vec{k}_d$. Similarly $\chi_x^{(-)}$ is the elastic scattering wave function for

particle x in the outgoing channel. The superscripts (+) and (-) denote

outgoing- and ingoing-wave boundary conditions (Sa 64).

As indicated above, these distorted waves are obtained by optical

model fits to the appropriate elastic scattering data. Optical model

fits to elastic scattering differential cross-section and/or polarization

angular distributions yield an optical model potential, U(r), which

generates the appropriate elastic scattering distorted waves through the

solution of the Schrödinger equation

$$[\nabla^2 + k^2 - \left(\frac{2\mu}{\hbar}\right)^2 U(r)] \; \chi(\vec{k},\vec{r}) = 0 \tag{1.2}$$

The potential $U(r)$ is taken to be of the form (Ba 64, Le 64, Pe 66)

$$U(r) = U_c(r) - Vf(r,r_{OR}, a_R) + 4i \, a_I \, W \, \frac{d}{dr} \, [f(r,r_{OI},a_I)]$$

$$+ \left(\frac{\hbar}{m_\pi c}\right)^2 V_S \, \frac{\vec{L} \cdot \vec{\sigma}}{r} \, \frac{d}{dr} \, [f(r,r_{OS},a_S)] \qquad (1.3)$$

The Coulomb potential $U_c(r)$ is taken to have the form

$$U_c = \frac{Ze^2}{2R_c} \left[3 - \frac{r^2}{R_c^2} \right] \qquad\qquad \text{for } r \leq R_c$$

$$= \frac{Ze^2}{r} \qquad\qquad\qquad \text{for } r > R_c \qquad (1.4)$$

where

$$R_c = r_{oc} \, A^{\frac{1}{3}} \qquad (1.5)$$

is the Coulomb radius $(r_{oc} \approx 1.3 \text{ fm})$. The form factors for the remaining potentials in equation (1.3) are taken to have the Saxon-Woods shape

$$f(r,r_o,a) = \{1 + \exp[(r-r_o \, A^{\frac{1}{3}})/a]\}^{-1} \qquad (1.6)$$

V is the strength of the real potential representing shape elastic scattering and W is the strength of the imaginary potential representing absorption of particles from the elastic scattering channel. V_S is the strength of the spin-orbit potential describing the coupling between the spin of the incoming particle $\vec{\sigma}$ and its orbital angular momentum $\vec{L}$. The mass m_π is the pion mass.

In equation (1.1) $|A,d\rangle$ represents the internal states of the colliding particles A and d, while $|B,x\rangle$ describes the internal states of the final nucleus and the outgoing particle. The potential V' is the agent responsible for inducing the transition between the initial and final states. In stripping reactions it becomes (Le 64)

$$V' = V_{np} + (V_{xA} - U_{xB}) \tag{1.7}$$

where V_{np} is the neutron-proton potential, V_{xA} is the potential between particle x and the target nucleus A and U_{xB} is the optical potential for the outgoing channel defined in equation (1.3). Usually it is assumed that $V_{xA} \approx U_{xB}$ so that $V' \approx V_{np}$ is used for the stripping calculations. Although this approximation is used universally its validity is questionable (Le 64, Pe 66a).

Satchler (Sa 64) has chosen to factor the transition amplitude into (1) a spectroscopic coefficient $A_{\ell s j}$ which includes such quantities as fractional parentage coefficients for the initial or final nuclear states and the interaction strength, and (2) a form factor $\beta_{sj}^{\ell m m_x m d}(\vec{k}_x, \vec{k}_d)$ which accounts for the remaining parts of the transition amplitude. Thus equation (1.1) is expressed as (Sa 64)

$$T = \sum_{\ell s j} (2j+1)^{\frac{1}{2}} A_{\ell s j} \quad \langle J_A \, j M_A, \, M_B - M_A \mid J_B \, M_B \rangle$$
$$\beta_{sj}^{\ell m m_x m d}(\vec{k}_x, \vec{k}_d) \tag{1.8}$$

Here J_A is the spin of the target nucleus with magnetic quantum number M_A, J_B and M_B represent the same quantities for the residual nucleus, and j is the total angular momentum of the captured nucleon with orbital

angular momentum ℓ and spin s. Specifically,

$$\vec{j} = \vec{J}_B - \vec{J}_A \tag{1.9}$$

$$\vec{s} = \vec{s}_d - \vec{s}_x \tag{1.10}$$

$$\vec{\ell} = \vec{j} - \vec{s} \tag{1.11}$$

It is customary to express the wave function $\psi_{J_B M_B}$ for the residual nucleus B in terms of eigenstates of the target $\psi_{J_A M_B}$.

$$\psi_{J_B M_B} (\vec{r}_{yA} \, \xi_y \, \xi_A)$$

$$= \sum_{j\mu J'_A M'_A} \psi_{J'_A M'_A} (\xi_A) \, \Omega^{BA'}_{j\mu} (r_{yA}, \xi_y) < J'_A \, jM'_A \, \mu \, | J_B M_B > \tag{1.12}$$

Assuming V_{np} does not depend on the coordinates $\vec{r}_{yA}$ only one term of the sum contributes to the transition amplitude, that term due to $J'_A = J_A$ and $M'_A = M_A$. The coordinate $\vec{r}_{yA}$ is the vector between the captured particle and target nucleus A. The remaining coordinates ξ_y and ξ_A refer to the internal coordinates of the captured particle and the target nucleus respectively. In (d,n) and (d,p) stripping reactions where the captured particle is a single nucleon the function Ω can be identified as the wave function ψ for the nucleon orbital (ℓ,j) times a spectro-scopic amplitude.[†]

[†]It has been suggested (Le 64) that the proportionality expressed by $\alpha^{BA}_{\ell j}$ is of doubtful validity in some cases.

$$\Omega_{j\mu}^{BA} (\vec{r}_{yA}, \xi_y) = \alpha_{\ell j}^{BA} \, \psi_{\ell j, \mu} (\vec{r}_{yA}, \xi_y) \qquad (1.13)$$

This permits definition of the usual spectroscopic factor (Sa 64) as

$$S_{\ell j} = n(\alpha_{\ell j})^2 \qquad (1.14)$$

where the factor n arises from antisymmetry considerations if there are

n equivalent nucleons in the orbit of the captured particle. If the

final nucleus can be represented as an inert, closed-shell core formed

by the target A with only the captured nucleon in the orbit (ℓ, j) the

spectroscopic factor becomes $S_{\ell j} = 1$. With the identification of

equation (1.13) the spectroscopic factor measures the extent to which

the final nucleus can be represented by an extreme single-particle shell

model. That is, the extent to which the stripped nucleon is captured

into a pure single-particle state.

The remaining assumption of note lies in the zero-range/finite-range

option. If the d-state of the deuteron is ignored, the deuteron internal

wave function ψ_d can be factored into a radial part $\phi_d(r_{np})$ and a spin

function $\psi_{s_d m_d}$.

$$\psi_d = \phi_d(r_{np}) \, \psi_{s_d m_d} \qquad (1.15)$$

Subsequently the interaction potential is grouped with the radial function

to define

$$D(r_{np}) = V_{np}^{(sd)} \, \phi_d(r_{np}) \qquad (1.16)$$

Here $V_{np}^{(s_d)}$ is the interaction potential for the deuteron spin-state s_d.

In the zero-range approximation it is assumed that the interaction $D(r_{np})$

is appreciable over such a short range that it may be replaced by a

normalized delta function.

$$D_{ZR}(r_{np}) \approx D_o \, \delta(r_{np}) \tag{1.17}$$

Effective-range analysis is used to choose D_o to provide the proper

normalization of the deuteron wave function at $r_{np} \to \infty$ (Sa 64). The

resulting value is

$$D_o^2 \approx 1.5 \times 10^4 \text{ MeV}^2 \text{ fm}^3 \, . \tag{1.18}$$

In the past it has been assumed reasonable to neglect the d-state

of the deuteron since it represents a very small part of the total

deuteron wave function. However, it has been shown recently that the

d-state probably makes a large contribution to spin-dependent effects

in stripping differential cross-sections (Jo 67).

In the above discussion an attempt has been made to expose the

basic physical assumptions inherent in DWBA theory without involving

detailed mathematical derivations. These derivations are adequately

expounded elsewhere (Sa 64), and tend not to add much to physical insight

into the model. With the transition amplitude expressed above we can

now define the differential cross-section and the polarization.

The differential cross-section for unpolarized projectiles and

unpolarized target nuclei is given by (Sa 64)

$$\frac{d\sigma(\theta)}{d\Omega} = \frac{\mu_d\,\mu_x}{(2\pi\hbar^2)^2}\,\frac{k_x}{k_d}\,\frac{\sum|T|^2}{(2J_A+1)\,(2s_d+1)} \qquad (1.19)$$

where μ_d and μ_x are the reduced masses of the respective particles and the sum is over M_A, m_d, M_B, and m_x. This can also be written as

$$\frac{d\sigma(\theta)}{d\Omega} = \frac{\mu_d\mu_x}{(2\pi\hbar^2)^2}\,\frac{k_x}{k_d}\,\frac{(2J_B+1)}{(2J_A+1)\,(2s_d+1)}$$

$$\cdot \sum_{jmm_xm_d}\left|\sum_{\ell s}B_{sj}^{\ell mm_xm_d}\right|^2 \qquad (1.20)$$

where

$$B_{sj}^{\ell mm_xm_d} = A_{\ell sj}\,\beta_{sj}^{\ell mm_xm_d} \qquad (1.21)$$

The polarization of the outgoing particles is defined as

$$P_x(\theta) = \frac{\langle s_x\rangle}{|s_x|}\left[\frac{d\sigma(\theta)}{d\Omega}\right]^{-1} \qquad (1.22)$$

where $\langle s_x\rangle$ is the expectation value of the spin of the outgoing particles. The only non-vanishing component is that parallel to the vector $\vec{k}_d \times \vec{k}_x$ (Sa 64)

$$P_x(\theta) = \frac{\sum[(s_x-m_x)(s_x+m_x+1)]^{\frac{1}{2}}}{s_x\,\sum B_{sj}^{\ell mm_xm_d}\,(B_{s'j}^{\ell'mm_xm_d})^*} \qquad (1.23)$$

$$\cdot\ \mathrm{Im}\,[B_{sj}^{\ell mm_xm_d}\,(B_{s'j}^{\ell'\ m+1\ m_x+1\ m_d})^*]$$

where the sums are both over s, s', ℓ, ℓ', j, m_d, m_x, and m. It can

be seen from equations (1.20) and (1.23) that the polarization is

sensitive to different aspects of the transition amplitude than the

differential cross-section is. The inverse dependence of $P_x(\theta)$ on

the differential cross-section indicates that large polarizations are

likely to be observed at angles where the differential cross-section

is small. This point is generally borne out in experiments.

In general only one j value contributes in (d,n) and (d,p)

stripping reactions. This restricts the spins of the levels populated

in the final nucleus through the relation

$$\vec{J}_B = \vec{j}_y + \vec{J}_A \tag{1.24}$$

Although j-dependent effects have been observed in differential cross-

sections (La 67, Da 66, Le 64a, Bu 66) these angular distributions

generally permit reliable identification of only the ℓ-value of the

captured nucleon. Hence the j value is ambiguous to the extent that

$$j_y = \ell_y \pm \frac{1}{2} \tag{1.25}$$

is determined only to within one unit of angular momentum. If the target

nucleus has zero spin, then the spin of the final state is determined

to be $J_B = \ell_y \pm \frac{1}{2}$. The parity π_B of the state is also determined since

the parity change in the reaction is (Sa 64)

$$\pi_B = (-1)^\ell \pi_A \tag{1.26}$$

where π_A is the parity of the ground state in the target nucleus.

1.3 Experimental Determination of the Spectroscopic Factor

In most computer codes for the calculation of the differential cross-section in the distorted wave Born approximation the wave function for the captured particle, y, is generated from an optical potential of the type

$$U_y = U_c(r) - Vf(r, r_{OR}, a_R)$$

$$+ \left[\frac{\hbar}{m_\pi c}\right]^2 V_S \frac{\vec{L} \cdot \vec{\sigma}}{r} \frac{d}{dr} [f(r, r_{OS}, a_S)] \qquad (1.27)$$

where the terms on the right hand side are defined in equations (1.4) to (1.6). The wave function is an extreme single-particle wave function and is calculated by solving a Schrödinger equation for the motion of the captured nucleon in the potential U_y. The potential depth V is adjusted by the computer program to produce the binding energy required for the state chosen in the final nucleus. Since the calculation is for an extreme single-particle state the spectroscopic factor is calculated to be unity. In the experiment being performed the final state formed may not be a pure single-particle state. The spectroscopic factor for the experiment then should be less than unity. If reliable absolute cross-sections are measured in the experiment, then the spectroscopic factor relevent to the final state observed experimentally can be calculated from

$$S_{\ell j} = \left. \frac{d\sigma(\theta)}{d\Omega} \right|_{exp} \cdot \left[\left. \frac{d\sigma(\theta)}{d\Omega} \right|_{Th} \right]^{-1} \qquad (1.28)$$

where $\left. \dfrac{d\sigma(\theta)}{d\Omega} \right|_{exp}$ is the experimentally measured cross-section and

$\dfrac{d\sigma(\theta)}{d\Omega}\bigg|_{Th}$ is the theoretically predicted cross-section for a pure

single-particle state. Equation (1.28) follows from equations (1.12),

(1.13), (1.14), and (1.1). The spectroscopic factor consequently promises

to be a useful tool in determining the nature of the nuclear structure

of the final state formed in nucleus B. Unfortunately stripping theory

is still not sufficiently sophisticated to permit a high degree of con-

fidence in such spectroscopic factors. It is apparent that several of

the weaker approximations in DWBA theory need thorough study both experi-

mentally and theoretically before reliable spectroscopic information can

be obtained.

1.4   Experimental Approach to Stripping Reaction Studies

The formalism of section 1.2 indicates that in order to calculate

the stripping cross-section and polarization a knowledge of the elastic

scattering wave functions is required for the incoming and outgoing

channels. At the least this requires a measurement of elastic scattering

cross-sections for the incoming channel and for the scattering of the

outgoing particle from the residual nucleus B at the energies involved

in the stripping reaction. Several problems arise which make such simple

measurements inadequate. First of all the polarization in the stripping

reaction is very sensitive to the spin-orbit potentials in the incoming

and outgoing channels. It turns out (Pe 66, Pe 67, Ro 65, Ro 65a, Ro 66)

that differential cross-sections are relatively insensitive to the spin-

orbit potential. In order to define accurately the proper spin-orbit

potential the polarization effect in elastic scattering must be measured

(Ro 65, Ro 65a, Ro 66). Secondly the optical model is really an average

model. That is, it treats the mechanics of scattering by ignoring nuclear structure. The nucleus is represented essentially by a spherical semi-transparent ball. In many cases compound nucleus fluctuations affect the elastic scattering to yield slightly different potentials from experiments performed at different energies. Hence to get a truly average set of optical potentials the elastic scattering must be studied over a large number of nuclei and over a wide energy range. With such information the average behaviour can be traced over the whole range of nuclei and bombarding energies. This approach also eliminates many of the ambiguities found in analysing one isolated elastic scattering experiment. Such a comprehensive survey has been carried out for neutrons and protons (Ro 65, Ro 65a, Ro 66), and the optical parameters for elastic scattering of neutrons and protons are now regarded as quite well established.[†] There is still an urgent need for a similar study of deuteron elastic scattering (Pe 66). In fact the absence of well established average deuteron potentials is one of the largest stumbling blocks in the study of (d,n) and (d,p) stripping reactions at the present time.

Given a good set of average elastic scattering potentials one can then concentrate on the study of the stripping reaction itself. As has been mentioned previously ambiguities in the results of such a study still arise. It is for this reason that the following approach has been taken in this laboratory.

[†] Whether elastic scattering wave functions provide a reasonable description for the outgoing channel when the residual nucleus is left in an excited state is open to question. Experimentally there is little that can be done to resolve this problem.

First of all the target nucleus should be selected such that the spectroscopic factor can be reliably predicted for the experiment. This means that the target nucleus should provide a good closed-shell core for the residual nucleus. In the range of nuclei accessible with a 6 MeV bombarding energy there are two likely candidates: ^{40}Ca and ^{16}O. Of the two ^{40}Ca is the more desirable since it has a higher mass number. One anticipates some difficulty in ignoring nuclear structure and treating the nucleus as an average optical potential at low mass numbers where the nucleus is made up of very few nucleons. Choice of a doubly closed-shell nucleus such as ^{40}Ca has a further advantage. With the ^{40}Ca(d,p)^{41}Ca and ^{40}Ca(d,n)^{41}Sc reactions mirror nuclei are produced in the final state. On the basis of the single-particle shell model one would expect the ^{41}Ca ground state to consist of one proton in the $1f_{\frac{7}{2}}$ shell outside a closed shell of 20 protons and an inactive core of 20 neutrons. The ^{41}Sc ground state is expected to have the same configuration with the roles of the neutrons and protons reversed. Hence the spectroscopic factors for transitions to the ground states in these two reactions should be $S_{3,\frac{7}{2}} = 1$. The two reactions should be identical except for the effect of the Coulomb potential. The sharing of a common entrance channel means that the deuteron elastic scattering parameters must provide an accurate description for both reactions simultaneously. Similarly, the two reactions, including the entrance and exit channel elastic scattering experiments, share the same compound nucleus levels in ^{42}Sc (at about 16 MeV excitation energy). Clearly, the correlation

in these two stripping reactions is strong, and taken together they
should provide a stringent test of DWBA predictions.

Aside from the theoretical advantages there is a practical reason
for studying the reactions on ^{40}Ca. Considerable work has been carried
out on this nucleus at energies from 7 to 12 MeV (Ba 64, Le 64, Mi 66,
Hj 65) with the (d,p) and (d,d) reactions. Except for the spin-orbit
potential a good average set of deuteron potentials has been established
for the energy range from 7 to 12 MeV (Ba 64, Le 64). This information
provides a good starting point for extrapolating the average set to
lower energies where the deuteron elastic scattering has been measured
at 5, 6, and 6.5 MeV (Le 67, Le 68). The work on the (d,p) reaction at
higher energies provides information complementary to the lower energy
studies undertaken here.

There are, however, some disadvantages in choosing ^{40}Ca. The most
serious problem arises from the Coulomb potential. While the separation
energy for the $1f_{\frac{7}{2}}$ neutron in ^{41}Ca is 8.36 MeV, the binding energy of
the last proton in ^{41}Sc is 1.08 MeV. Hence, only the ground state is
bound in ^{41}Sc and the Q values for the two stripping reactions differ
by 7.29 MeV (^{40}Ca(d,p)^{41}Ca: Q = +6.14 MeV; ^{40}Ca(d,n)^{41}Sc: Q = -1.146 MeV).

The degree to which one can regard the ^{40}Ca ground state as a
closed shell is not as perfect as one would hope. Gerace and Green (Ge 67c)
have shown that there is a significant contribution of 2 particle-2 hole
states and some contribution from 4 particle-4 hole states to the ground
state of ^{40}Ca. This causes deformation of the ^{40}Ca nucleus to a non-
spherical shape. The effect on excited states in ^{41}Ca and ^{41}Sc is

Figure 1.1   The lower energy levels of ^{41}Ca and ^{41}Sc. Taken from references (Gr 67, Bo 65, En 62)

Ex (MeV)	J^π	l_n

Ex (MeV) J^π l_n

3.50 ——————
3.40 ——————
3.37 ——————   0
3.21 ——————
3.06 ——————
2.97 ——————   1
2.89 ——————

2.61 2.68 —————— $\frac{1^+}{2}$ 0
     2.58 ——————
2.469 —————— $3/2^-$ 1

2.014 —————— $3/2^+$ 3^- 2
1.947 —————— $\frac{3}{2}$ 1

gs. —————— $\frac{7^-}{2}$ 3

^{41}Ca

Ex (MeV) J^π l_p

3.776 ——————
3.721 ——————

3.463 —————— $(\frac{1^-}{2})$

3.20 ——————

2.719 ——————
2.593 ——————
2.415 —————— $\frac{3^-}{2}$ 1

2.096 —————— $\frac{3^+}{2}$ 2

1.718 —————— $\frac{3^-}{2}$ 1

g.s. —————— $\frac{7^-}{2}$ 3

^{41}Sc

noticeable in the (d,p) and (d,n) reactions. Figure 1.1 shows the energy levels of ^{41}Ca and ^{41}Sc. Gerace and Green have shown that the extra $2p_{\frac{3}{2}}$ states at 2.469 MeV in ^{41}Ca and 2.415 MeV in ^{41}Sc are due to mixing of a rotational state with the expected single-particle $2p_{\frac{3}{2}}$ states at 1.947 MeV and 1.718 MeV respectively. In both the (d,p) and (d,n) reactions the $2p_{\frac{3}{2}}$ single-particle strength is found to be shared between these two states. The dominant strength in both reactions, of course, feeds the lower $2p_{\frac{3}{2}}$ level. On the other hand, spectroscopic factors in both reactions appear to be close to unity for the ground states of ^{41}Ca and ^{41}Sc (Gr 67, Le 68, Gr 67a, Le 67, Le 64).

CHAPTER 2

THE NEUTRON POLARIMETER

A description of the neutron polarimeter has been given previously in connection with studies on the ^{28}Si(d,n)^{29}P reaction (La 67). A brief review of the helium cryostat construction will be presented. Particular attention has been given to an account of the electronic instrumentation since the author was closely associated with this aspect of the polarimeter.

2.1 The Helium Cryostat

Most neutron polarimeters are based on the scattering of neutrons by ^{4}He nuclei for several reasons.

1. n-α scattering has been studied to such an extent that the phase shifts are well known. Thus it is possible to calculate the analysing power of a ^{4}He scatterer with reasonable accuracy over a wide energy range (up to $\approx$ 20 MeV) (Ma 63 , Ho 66).

2. The cross-section for n-α scattering is of a useable magnitude (~100 mb/sr) (Ho 66).

3. The analysing power of ^{4}He is large (~0.9) at suitable scattering angles and shows a smooth variation with energy.

4. Helium can be used in the liquid state to obtain a scatterer with high density.

5. The recoiling α particles from n-α scattering cause scintilla-
   tions in liquid helium. These scintillations can be used to
   detect the scattering event.

The polarimeter used in this work employed a liquid helium cell as the

neutron polarization analyser. The construction of the cryostat con-

taining the liquid helium scatterer was based on a design described by

Simmons and Perkins (Si 61) and improved on by Kane et al (Ka 63). Except

for the coating of the inside of the scintillation chamber and the

vacuum sealed mounting of the photomultiplier the cryostat was provided

as a commercial product by Hofman Cryogenics.[†]

Figure 2.1 gives an outline of the major features of the cryostat.

A central container holds the liquid Helium in a reservoir of 1.0 litres

capacity. The liquid Helium container is surrounded by a liquid air

reservoir which serves as a heat sink for the heat shield surrounding the

entire helium volume. The space between and around the two reservoirs is

evacuated to a pressure of 2×10^{-7} mm of mercury by a mercury diffusion

pump. The active scintillator volume is defined by a 2" diameter x 4" long

stainless steel reflector. An RCA8575 photomultiplier views the scintillating

volume through a sapphire window. The distance between the window and the

phototube is about 1/8". In order to provide good light collection the

inside of the reflector has been coated with several materials (La 67).

The coatings are indicated in the inset of figure 2.1 as a layer of Al

followed by a thin layer of SiO, a thin coating of white Tygon paint

(La 67) and finally $\geq$ 100 μg/cm^2 p,p'-diphenylstilbene (wavelength shifter).

This recipe follows that of Kane et al (Ka 63). The wavelength shifter

---

[†]Hofman Cryogenics, 225 Parkhurst Street, Newark, New Jersey, U.S.A.

Figure 2.1   A sectional view of the helium
cryostat.   The inset indicates schematically
the coating on the reflector.

TO SYPHON

HELIUM RECOVERY LINE

INLET

OUTLET

TO VACUUM PUMP

LIQUID AIR

LIQUID HELIUM

SIPHON GUIDE

REFLECTOR

HEATSHIELD

SAPPHIRE WINDOW

PHOTOTUBE

"O-RING" SEAL

0

5

10 INCHES

WAVE SHIFTER

WHITE PAINT

SILICON MONOXIDE

ALUMINUM

STAINLESS STEEL

SAPPHIRE WINDOW

PHOTOTUBE
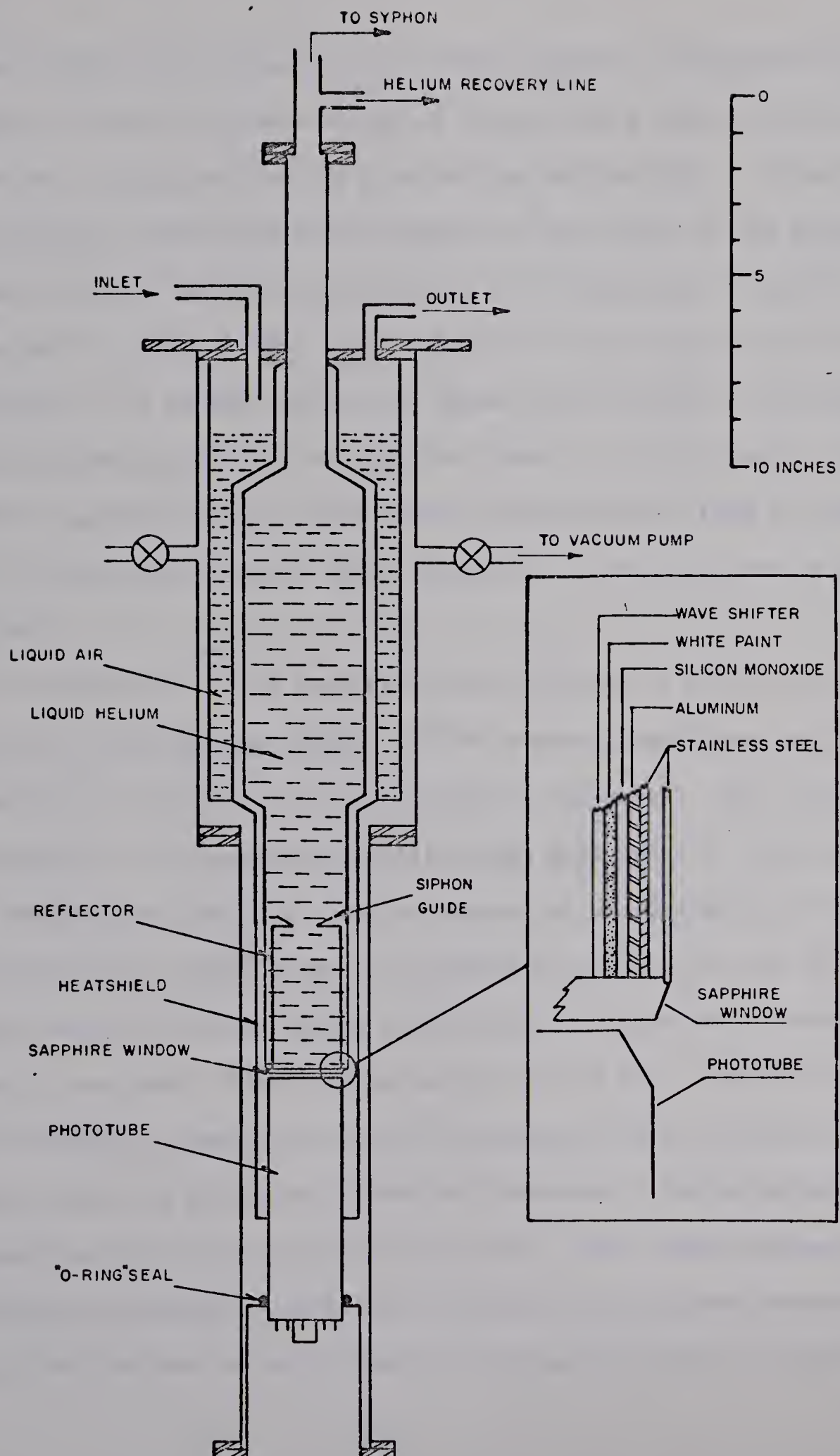
serves to shift the frequency of the light from the scintillation to
a region in which the photomultiplier cathode has a high sensitivity.
The other coatings are used to provide high reflectivity. A thin layer
of wavelength shifter was also deposited on the inside of the sapphire
window to ensure that direct light from the scintillator is shifted to
the proper frequency. This layer should be thick enough to function
efficiently ($\sim$50 μg/cm^2) but not so thick that it begins to attenuate
the light passing through the sapphire window. It is presently con-
sidered that the coating on the window is much thicker than 50 μg/cm^2
and is causing some loss of light intensity. A thinner layer is more
desirable.

An indication of the quality of the reflector is given by the
results of the following tests. A ^{239}Pu α-source was placed in the
scintillator on the axis of the cylindrical reflector. The output of
the·phototube was integrated, amplified and analysed for pulse height
in a multichannel analyser. As the source was moved from the bottom of
the scintillator volume (near the sapphire window) to the top the
energy resolution (pulse height resolution) was observed to increase
linearly from about 24% to approximately 38% (La 67). The decrease in
pulse height was compared to the $1/r^2$ intensity law on the basis of the
distance from the phototube cathode to the source. The pulse height was
observed to fall off less rapidly than $1/r^2$. This result indicates that,
although the dominant contribution of light came by direct transmission
from scintillations in the vicinity of the source, there was also some

contribution from light reflected from the walls of the scintillator volume. It is not surprising that with a tall cylinder the reflected light is not efficiently collected. Best light collection with a scintillator is usually obtained when the scintillator is thin and has a large area (perpendicular to the thin dimension) in contact with the photocathode of the phototube. It is anticipated that very little improvement can be made in the collection of reflected light without a drastic change in geometry. Some improvement in pulse height resolution should be possible with more careful control of the thickness of the wavelength shifter layer on the sapphire window. A factor of 2 increase in detected light intensity should decrease the pulse height resolution (and the time resolution) by a factor of $\sqrt{2}$.

2.2 Polarimeter Scattering Geometry

Figure 2.2 shows the general scattering geometry of the neutron polarimeter. The target nucleus A is bombarded by the accelerated beam of particles, a, from the University of Alberta 5.5 MeV Van de Graaff accelerator to produce reactions of the type

$$A(a,n)B$$
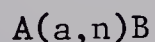
In order to analyse the polarization of the neutrons produced in the reaction the neutrons are scattered from the 2" diameter by 4" long active helium volume and detected in one of two neutron detectors located symmetrically on either side of the cryostat. If these detectors are labelled "left" and "right" as shown in the diagram, then the neutron

Figure 2.2   The polarimeter geometry used in
the ^{40}Ca(d,n)^{41}Sc measurements.   The neutron
detectors are 2" thick by 3-1/2" diameter NE213
scintillators mounted on XP1040 photomultipliers.
The cylindrical axes of the scintillators and
the phototubes lie along the lines from the
cryostat defining the 123°_{LAB} mean scattering
angles.
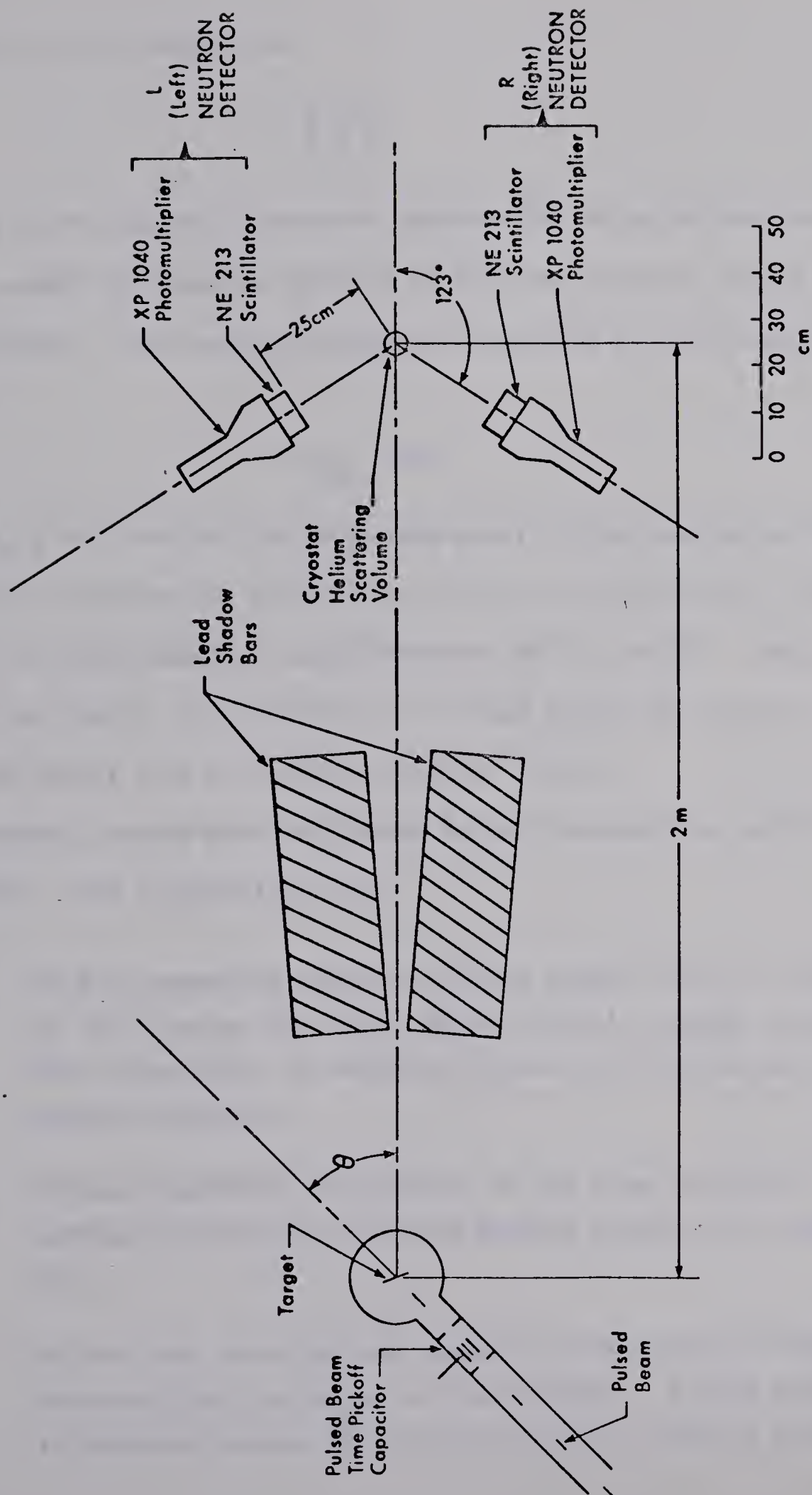
asymmetry can be defined as

$$\varepsilon = \frac{R - L}{R + L}$$

where R is the number of neutrons detected in the right detector, and L

is the number of neutrons detected in the left detector during the same

time interval. The neutron asymmetry is related to the neutron polariza-

tion by

$$\varepsilon = A_{eff} \ P(\theta)$$

where A_{eff} is the effective analysing power of the neutron polarimeter

and $P(\theta)$ is the neutron polarization at the reaction angle θ with

respect to the bombarding beam direction (Hu 61, Hu 66). Lead shadow

bars 60 cm long by 20 cm wide by 25 cm high shield the neutron detectors

from the direct flux of neutrons from the target.

Several systems were considered before choosing the method used in

this work. The alternatives were

1. DC beam operation using the linear signal from the photomultiplier
    in the cryostat for pulse height analysis (energy analysis). A
    fast coincidence is demanded between the cryostat and each
    neutron detector.

2. DC beam operation and analysis of the time of flight of neutrons
    between the cryostat and each neutron detector for energy separa-
    tion.

3. Pulsed beam operation and analysis of the time of flight of
    neutrons from the target to the cryostat. A fast coincidence
    is demanded between the cryostat and each neutron detector.

4. Pulsed beam operation with separate time of flight measurements
    between the target and each of the two neutron detectors. The
    flight path is composed of the distance from the target to the
    cryostat plus the distance from the cryostat to the respective
    neutron detector. A fast coincidence is demanded between the
    cryostat and each neutron detector.

Method (1) was ruled out because the energy resolution (~30%) was sub-
stantially worse than that provided by a time of flight system (~ 7%)
The remaining time of flight alternative must be compared on a basis of
energy resolution for the same detection efficiency. The energy resolu-
tion of a time of flight system can always be improved at the expense
of detection efficiency by increasing the length of the flight path
(providing target thickness is not a dominant factor).

Method (2) is not useable because the flight paths between the
cryostat and the neutron detectors must be made long for adequate energy
resolution. To recover the detection efficiency the distance from target
to cryostat must be made short. The resulting geometry severely restricts
the range of reaction angles which can be studied.

Superficially method (4) would seem to be an improvement on method (3)
due to the increased flight path length (Mi 67a). In actual fact this is
not the case. Nonrelativistically the neutron energy is related to the
flight path length, S, and the time of flight, t, by

$$E = \frac{1}{2} m_n \left(\frac{S}{t}\right)^2$$

where m_n is the neutron mass.

By partial differentiation the contribution to the energy resolution, $\Delta E/E$, due to detector thickness, ΔS, is

$$\left.\frac{\Delta E}{E}\right|_{\Delta S} = 2\,\frac{\Delta S}{S}$$

The contribution from the intrinsic time resolution of the detector, Δt, is

$$\left.\frac{\Delta E}{E}\right|_{\Delta t} = -2\,\frac{\Delta t}{t}$$

For the comparison let us use the following figures:

(a) Flight path from target to cryostat = 2 meters

(b) Flight path from cryostat to neutron detector = 25 cm

(c) Cryostat thickness = 5.08 cm diameter

(d) Neutron detector thickness = 5.08 cm

(e) Mean n-α laboratory scattering angle ≈ 120°

For method (3) the detector thickness contribution is approximately

$$\left.\frac{\Delta E}{E}\right|_{\Delta S} = \frac{2 \times 5.08 \times 10^{-2}}{2} = 5.08\%$$

For method (4) the cryostat thickness contributes both before and after scattering with an effective thickness of approximately $\sqrt{3}$ x 5.08 cm. The neutron detector contributes an additional thickness of 5.08 cm. If we assume that the two thicknesses combine as statistically independent quantities, the total effective thickness is 10.16 cm. Consequently the resolution contribution due to detector thickness for method (4) is

$$\frac{\Delta E}{E}\bigg|_{\Delta S} = \frac{2 \times 10.16 \times 10^{-2}}{2.25} = 9.0\%$$

This contribution is almost a factor of two larger than in method (3).

For a narrow range of pulse heights the intrinsic time resolution of a scintillation detector is roughly proportional to $E^{-\frac{1}{2}}$. For a neutron detector accepting all pulse heights from a 0.5 MeV threshold up to the maximum pulse height this dependence on energy is somewhat weaker. A crude estimate giving $\Delta t \propto E^{-0.3}$ can be considered typical. In either case the energy resolution contribution is

$$\frac{\Delta E}{E}\bigg|_{\Delta t} = \frac{2\Delta t}{t} = k\frac{E^{-x}}{E^{-\frac{1}{2}}} = kE^{(0.5-x)}$$

where $0.5 \geq x \geq 0.3$ and k is a proportionality constant. For the cryo-stat where a narrow pulse height range is selected by the recoil kinematics[†] $x \approx 0.5$ and

$$\frac{\Delta E}{E}\bigg|_{\Delta t} \approx k$$

so that the contribution to the energy resolution is approximately inde-pendent of energy. For the neutron detector $x \approx 0.3$ and

$$\frac{\Delta E}{E}\bigg|_{\Delta t} \approx k\,E^{0.2}$$

which is a slowly increasing function of energy.

A measurement of the time resolution as a function of pulse height with 20 MeV neutrons bombarding the cryostat indicates a contribution to

---

[†] With the geometry defined above the mean energy of the recoiling alpha-particles is $E_\alpha = 0.54\,E_n$, where E_n is the incident neutron energy. The range of alpha recoil energies is limited to approximately $\pm$ 6% of E_α by the solid angles defined by the neutron detectors. This range is small compared to the nominally 30% pulse height resolution inherent in the cryostat scintillator. However, the 30% resolution is still sufficiently small to allow choosing $x \approx 0.5$ for the cryostat.

the energy resolution of ≈ 4.5% for a 10 MeV alpha recoil energy and a flight path of 2 meters. Typical figures for the neutron detector give a time resolution of ≈ 1.2 nsec at 10 MeV and ~ 1.7 nsec at 2.25 MeV. These time resolutions give an energy resolution contribution of 6.2% at 20 MeV and 4.4% at 5 MeV when referred to the energy of the neutrons before scattering from the cryostat. (Approximately half the incident neutron energy is lost to the recoiling ^{4}He nucleus). Consequently, at 5 MeV neutron energy method (3) gives an energy resolution of ≈ 6.8% to be compared to ≈ 10% for method (4). At 20 MeV the figures differ slightly more, ≈ 6.8% compared to 11%.

Clearly method (4) offers no improvement in the energy resolution. Experimental confirmation of this fact recently has been offered by Miller (Mi 67b) in contradiction to his earlier suggestion (Mi 67a).

Method (3) was consequently the experimental arrangement chosen for this work. The flight path from target to cryostat was 2 meters. This length represented a compromise between energy resolution and counting rate. The neutron side detectors were set at a mean laboratory angle of 123° because the analysing power of n-α scattering is large and relatively independent of energy at this angle. The neutron detectors were 2" thick by 3-1/2" diameter "bubble-free" NE213 scintillators[†] mounted on XP1040 photomultipliers. The axes of the cylindrical scintillators and the phototubes were aligned with the 123° mean scattering direction in the reaction plane. The distance from cryostat center

[†]Provided by Nuclear Enterprises Ltd., 550 Berry Street, Winnipeg 21, Canada.

to the front face of the scintillators was 25 cm. With this geometry
the neutron detectors subtended an angle of 20° in the reaction plane
at the center of the cryostat. This angle covers a range of scattering
angles centered at 123°(LAB) where the analysing power of the helium is
large (Ho 66). The length of the flight path was chosen to keep the
size of the polarimeter reasonably small and to minimize the differences
in flight times from the cryostat to the neutron detectors for the range
of neutron energies accepted. The pulsed deuteron beam from the Univer-
sity of Alberta 5.5 MeV Van de Graaff and Mobley compression system was
used to bombard the target. This system provides beam pulses with
widths between 400 and 500 psec at a repetition rate of 10^6/sec (Da 66,
Mc 67). An average beam current between 1.0 and 3.5 μA is obtainable.

2.3 Electronic Instrumentation

The electronics for the polarimeter consists of a basic time-of-
flight system between a capacitive time pickoff just before the target
and the helium cryostat with fast coincidence circuits between the
cryostat and each neutron detector providing routing information.
Figure 2.3 shows the entire system. The main time-of-flight section
will be described first.

(a) Beam Pickoff: The stop channel of the main time-of-flight system
was driven by a time pickoff from the pulsed deuteron beam. A cylindri-
cal capacitor is mounted in the beam transport tube just ahead of the
target. As the beam pulse passes through the cylinder, a small signal is

Figure 2.3   A block diagram of the polarimeter
electronics as used in the measurement of neutron
polarizations.   For operation in the simple time
of flight mode the coincidence interrupt (COINC
INTPT) is operated by integral discriminator C
instead of by the output of the fan in.
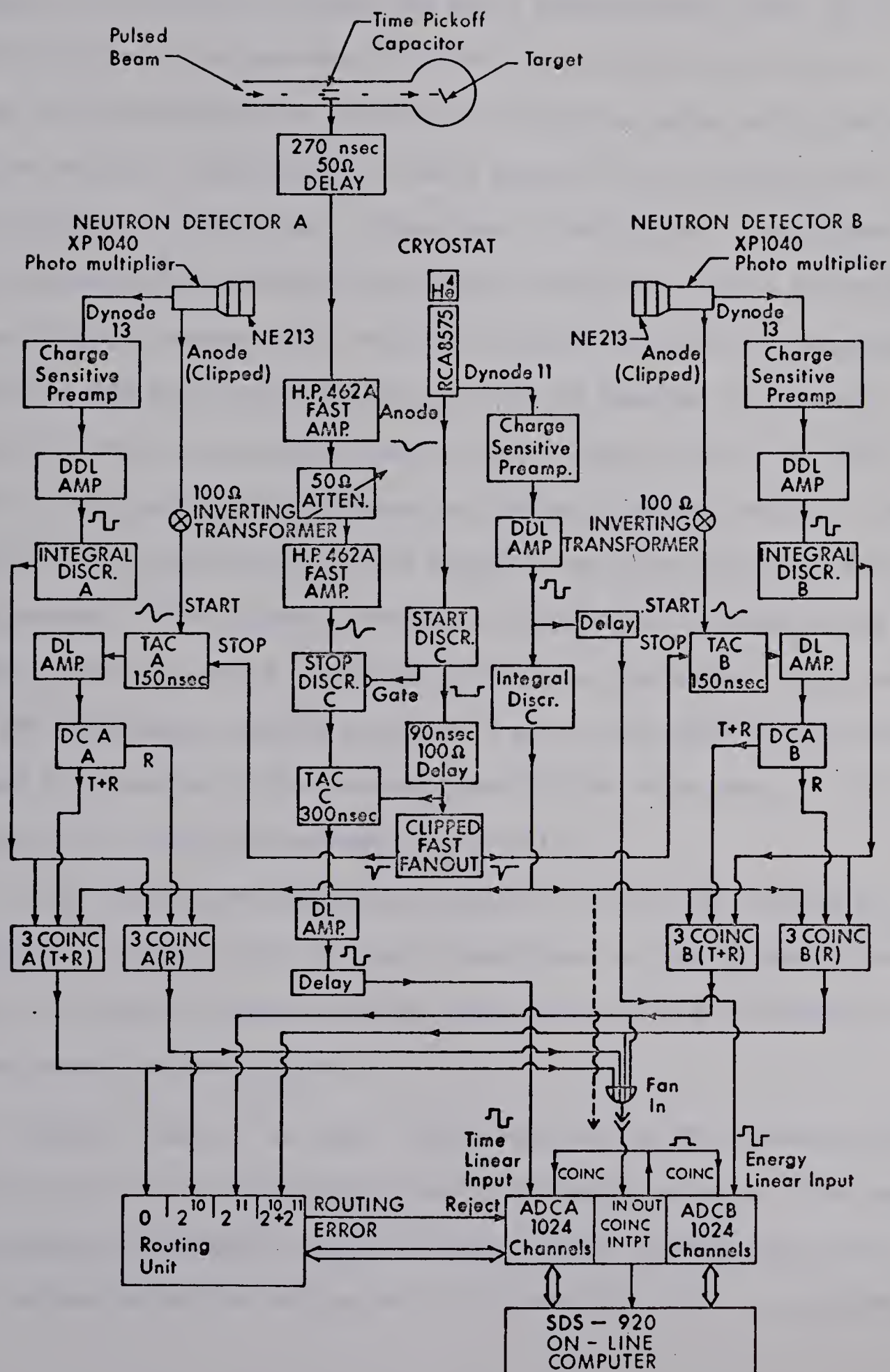
induced. The signal is bipolar and has a characteristic width of the order of 1 nsec (see appendix C). The zero-crossing point of this pulse is representative of the arrival of the beam pulse at the center of the capacitor, and hence provides a measure of the arrival time of the beam pulse at the target. This time pickoff signal is amplified by two fast amplifiers (Hewlett-Packard model 462A) with a 50 Ω attenuator providing gain control. The stop discriminator of the time-to-amplitude converter (TAC) was set to trigger as close as possible to the zero-crossing point on the negative phase of the bipolar pulse. The TAC's used in this experiment were based on a design by Wieber (Wi 63). Ideally a true zero-crossing discriminator should be used for the pulsed beam time pickoff. This approach prevents time shifts due to fluctuating pulse heights which are caused by changes in the beam conditions. Since performing the experiments reported here such a circuit has been designed and placed in operation in the neutron time-of-flight experiments. A full report on this device is provided in appendix C.

Since the stop discriminator is unable to run at 10^6 cps the discriminator was gated with the start discriminator. The 50 ohm 270 nsec delay was inserted to make the stop pulse arrive at the TAC after the start pulse from the cryostat.

(b) Cryostat Timing: The anode output from the RCA 8575 photomultiplier was used to time the scattering event in the helium cryostat. The start discriminator threshold was set to trigger on the leading edge of the fast current pulse from the anode. The threshold was set at approximately

1/5 of the maximum pulse height observed with the 662 keV gamma rays from a ^{137}Cs source. As with other fast neutron detectors, a wide range of pulse heights is produced for a monoenergetic neutron group due to the variety of allowed neutron scattering angles. This wide range of pulse heights produces "walk" in the electronic timing due to the finite discriminator threshold. The result is an undesirable broadening of the time resolution. A walk correction routine written for the SDS-920[†] on-line computer compensated for this effect (Mc 67b). This technique is described in more detail below.

The TAC output is a negative unipolar pulse and requires amplification as well as clipping in order to drive an amplitude-to-digital-converter (ADC). A single delay line clipped amplifier is used for this purpose. The delay line clip eliminates base line shifting with counting rate by producing a symmetrical bipolar pulse. The amplified pulse from TAC C was delayed and fed to a TMC model 217A 1024 channel ADC to record the time-of-flight information.

The current output from the last dynode of the RCA 8575 tube was integrated with a charge sensitive preamplifier, amplified by a double delay line clipped amplifier and fed to ADC B for the pulse height information. ADC B was identical to ADC A. The output of the double delay line clipped amplifier was inspected by an integral discriminator. When running in the simple time-of-flight mode the discriminator was connected directly to the coincidence interrupt input on the TMC 242 unit housing

[†]Scientific Data Systems, Santa Monica, California

the two ADC's. The discriminator is used to reject the smaller pulse

heights for which the time resolution is very poor (see figure 2.4).

The coincidence interrupt is used to signal the computer that the next

events from ADC A and ADC B are to be treated as a coincident pair. The

coincidence interrupt also provides a front panel output only when both

ADC's are not busy (Ge 66a). This output was used to operate the

coincidence gates on ADC A and ADC B.

The walk correction routine, data accumulation, and data storage

were all carried out with an SDS-920 on-line computer using the GPKS

system written by Dr. W. K. Dawson and J. F. Easton (Da 66a). The walk

correction technique has been thoroughly described elsewhere (Mc 67b,

La 67). Briefly, it functions as follows. First a two parameter

measurement of time versus pulse height is made using subroutine TWOD

(Da 66a) with ADC A and ADC B in coincidence. A reaction producing a

high energy neutron group, such as the $T(d,n)^4He$ reaction, is used as

the source of neutrons. The result is a walk curve with small pulse

height events showing later triggering times than higher pulses. From

this curve the number of channels on the time axis required to shift the

time peak for each pulse height to the same position as observed for the

largest pulse amplitudes is noted. This information is entered into

the TOFA (Da 66a) routine as a shift table for walk correction. For

subsequent time-of-flight operation ADC A and ADC B are operated in

coincidence in the TOFA routine. The pulse height information provided

by ADC B is used to identify the appropriate walk correction listed in

the shift table. This correction is applied to the time information from ADC A and the event is stored according to the resulting address. The result is a time-of-flight spectrum with the walk effects almost entirely eliminated.

With this system and a flight path of 2 meters a time resolution of 1.6 nsec was obtained with 19.6 MeV neutrons from the $T(d,n)^4He$ reaction. For 8 MeV neutrons from the $D(d,n)^3He$ reaction the resolution was 1.75 nsec (FWHM). For both of these measurements the cryostat was operated in the simple time-of-flight mode with all pulse heights above the lower threshold contributing to the time resolution. In polarization measurements restriction of the range of pulse heights in the cryostat by recoil kinematics reduces this time resolution because small pulse height events are rejected (see Figure 2.4). At low energies (≤ 5 MeV) this effect is not noticeable since the range of pulse heights accepted is already small. As the energy is increased above 6 MeV the reduction in resolution in the polarization mode becomes more significant. The lower threshold of the integral discriminator was set between 0.5 and 1 MeV equivalent neutron energy for most of the experimental runs.

(c) Neutron Detectors: A dynode output from each XP1040 photomultiplier was integrated and amplified in the same manner as for the RCA 8575 phototube. Integral discriminators were used to reject small pulse height events. The lower thresholds on both neutron detectors were set at approximately 500 keV effective neutron energy by calibrating with the 511 keV and 1.28 MeV gamma rays from a ^{22}Na source (Ba 61). It was

Figure 2.4   Time resolution of the cryostat as
a function of the helium recoil energy.   The
source of neutrons was the $T(d,n)^4He$ reaction
producing 19.6 MeV neutrons.   The start dis-
criminator threshold was set at an alpha particle
energy of approximately 250 keV.   Transit time of
the neutrons through the cryostat thickness in
addition to the beam pulse width contributes about
0.9 nsec.   The curve is taken from reference (La 67).

TIME RESOLUTION FROM T(d,n) ^{4}He
AT E_d = 3·0 MeV
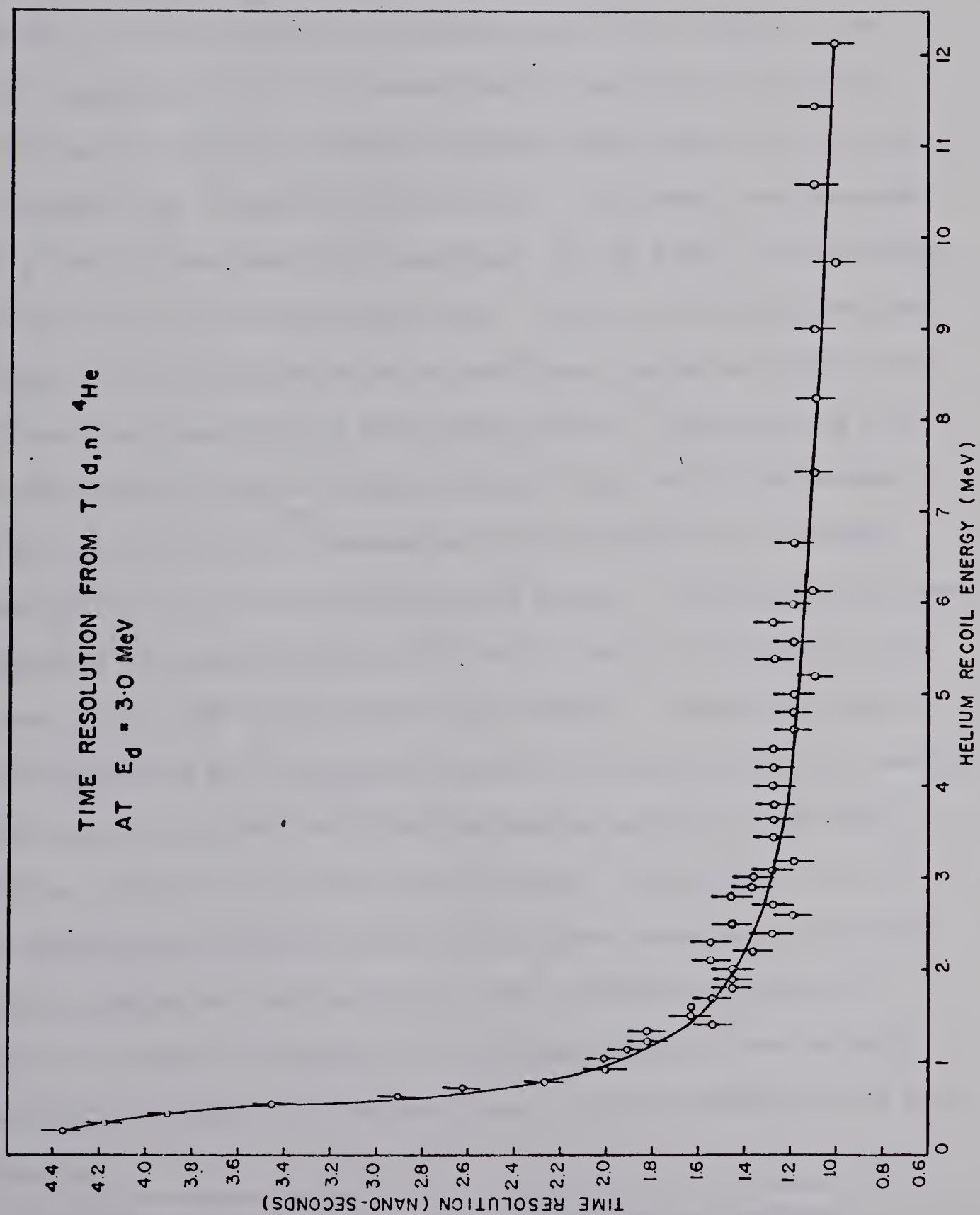
found essential to surround each XP 1040 phototube with an extra μ-metal magnetic shield. Without this precaution the phototube gains were sensitive to the orientation of photomultiplier with respect to the earth's magnetic field. The current output from the anode of each XP 1040 was RC clipped to produce a bipolar pulse with a leading edge to crossover time of approximately 10 nsec. The pulses were inverted with a fast 100 ohm inverting transformer (EH ZT 9-9X)[†] before driving the start input of the appropriate TAC. The start thresholds were set to trigger on the negative phase of the bipolar pulses as close to the zero-crossing phase point as noise would permit. This method of zero-crossing timing provides very poor intrinsic time resolution because the zero-crossing point is sensitive to the arrival time of charge generated very late in the scintillation process. The best defined time information is normally found on the leading edge of the current pulse at about 10% to 20% of the current pulse height. However, at the time these experiments were performed a method to eliminate walk with leading edge timing was not available for the neutron detectors. The above technique using a "near zero-crossing trigger" (as opposed to a true zero-crossing discriminator) was found to give better time resolution than the leading edge method without walk correction. Section 2.4 refers to a superior approach to fast timing which has been recently developed and tested on the neutron time of flight spectrometer in this laboratory.

[†]EH Research Laboratories, Inc., 163 Adeline St., Oakland, California, U.S.A.

Stop signals were obtained for TAC A and TAC B from the cryostat start discriminator C by a high input impedance clipped fast fanout designed for this purpose (Ge 66b). Negative 2 volt pulses of approximately 25 nsec duration were produced from the 1 μsec 6 volt rectangular pulse from start discriminator C. The TAC outputs were amplified by single delay line clipped amplifiers and presented to dual channel analysers (DCA). The time-of-flight spectra obtained from TAC's A and B in a typical reaction showed a broad peak due to gamma rays travelling from the cryostat to the neutron detectors. Adjacent to the gamma-ray peak was a very broad hump due to the variety of flight times for the different neutron groups from the cryostat to the neutron detectors. Due to the walk present in the stop channel and the poor intrinsic resolution in the start channel for TAC's A and B the gamma-ray peak and the neutron groups were not completely resolved with the 25 cm flight path. Consequently it was necessary to include both gamma rays and neutrons in the "true plus random" coincidence window set by the dual channel analyser.' The DCA consisted of two single channel analysers sharing the adjacent threshold. The lower window was set 50 nsec wide to include the gamma-ray peak near the upper threshold, and to cover flight times sufficiently long to accept 1 MeV neutrons above the lower threshold. This window includes both the desired true coincidences and the unwanted background occurring randomly in time. This window is labelled T+R (true plus random) in the diagram. In order to have an accurate subtraction of the random background the upper window of the

DCA was set 50 nsec wide in the purely random background region adjacent to the gamma-ray peak. This window is labelled R for random. Since the TAC's exhibited extreme nonlinearity it was necessary to calibrate the window widths by using a single 50 nsec delay cable inserted alternately in the start and stop channels. Gamma-ray eliminators were not employed with the neutron detectors because available circuits typically offer poor long term stability and make it difficult to match the neutron efficiencies between the two detectors.

In the polarization measurement four triple coincidence units were used. One input common to all units was obtained from the lower threshold set on the cryostat by the integral discriminator. For each neutron detector two coincidence units were driven with the integral discriminator setting the lower threshold for that detector. The outputs from the DCA's completed the inputs on each pair of triple coincidence units. Consequently the outputs from the coincidence units provided logic pulses signalling four classes of events.

1. A(T+R) = detector A, true plus random
2. A(R)   = detector A, random
3. B(T+R) = detector B, true plus random
4. B(R)   = detector B, random.

To make use of this information a routing unit was designed and built for use with the T.M.C. ADC's (Ge 65, Ge 66c). For the polarization measurements the routing is performed on ADC A by setting the appropriate combinations of the 2^{10} and 2^{11} bits. Since ADC A was run in the 1024 channel mode this resulted in the following time-of-flight spectra in the computer.

Channel	Spectrum
0 to 1023	A (T+R)
1024 to 2047	A (R)
2048 to 3071	B (T+R)
3072 to 4095	B (R)

A routing error pulse is generated by the routing unit whenever it is requested to route into two or more different regions at the same time. A special reject circuit was added to ADC A to cause the event to be tagged as an overflow and ignored in such a situation.

In the polarization mode the outputs of the four triple coincidence units were fanned in to operate the coincidence interrupt circuit. The output of the coincidence interrupt circuit operated the coincidence gates on ADC A and ADC B. The four triple coincidence units and the fan in were specifically designed for this application (Ge 66d).

The technique of routing the cryostat time-of-flight spectrum has proved useful in that it facilitates treating all four spectra in an identical fashion during data analysis. This helps to avoid introducing false asymmetries during data analysis. Simultaneous recording of the random-background reduces the required running time and guarantees that the experimental conditions are the same for the measurements of both the true plus random and the random spectra.

2.4 Improvements in Fast Timing Techniques

Since the completion of the polarization work a significant advance has been achieved in the development of fast timing techniques for scintillation detectors (Ge 67a, Ge 67b). It has been known for some

time that the optimum time resolution for a fast scintillator-photomultiplier combination is obtained by triggering on the leading edge of the anode current pulse at 10% to 20% of the pulse height (Mc 67a). A constant fraction of pulse height trigger was designed to trigger at this phase point independent of pulse amplitude. Tests have proven that this circuit provides the optimum time resolution for a scintillation detector and virtually eliminates the walk effect. The circuit has been found to operate well over a 100 : 1 dynamic range with a walk within $\pm$ 120 psec. Appendices A and B give a detailed account of this circuit in the form of preprints of papers which have been submitted for publication.

It is suggested that the use of the constant fraction of pulse height trigger could make a significant improvement in the operation of the neutron polarimeter. Sufficient improvement in the time resolution should be possible to permit the exclusion of the gamma-ray peak from the true plus random window. The "walkless" feature of the trigger of course means that the computer walk correction routine is unnecessary. In the runs with the neutron time-of-flight spectrometer to date the constant fraction of pulse height trigger has been demonstrated to improve the symmetry of peak shapes (Mc 67b). New time-to-pulse-height converters are now available (ORTEC model 437) which offer better operation than those used in this experiment. In particular the differential linearity shows a drastic improvement.

In order to incorporate the constant fraction of pulse height trigger, time resolution studies of the type reported in reference (Mc 67a) should

be carried out to determine the fractional triggering level which provides

the optimum time resolution. While the timing characteristics of the

cryostat have not been established it is possible to make a good

estimate of the proper fraction for the neutron detectors on the basis

of reference (Mc 67a).

2.5 Polarimeter Analysing Power

Figure 2.5 shows the simplified geometry necessary to define the

analysing power of the polarimeter. The beam from the accelerator

defines the incident direction $\vec{k}_i$. A neutron produced in the reaction

at the target travels in a direction $\vec{k}_f$ at the selected reaction angle

θ with respect to the bombarding beam. The reaction plane formed by

unit vectors $\vec{k}_i$ and $\vec{k}_f$ is defined by the normal vector

$$\vec{n} = \vec{k}_i \times \vec{k}_f$$

The neutron strikes the ^{4}He scatterer and recoils along the direction

defined by unit vector $\vec{k}'$ at an angle θ' with its original direction.

The scattering plane is defined by the normal vector

$$\vec{n}' = \vec{k}_f \times \vec{k}'$$

The line labelled by $\phi = 0$ to $\phi = \pi$ lies in the reaction plane and is

perpendicular to $\vec{k}_f$. The angle ϕ is defined by the angle between the

reaction plane and the scattering plane.

$$\vec{n} \cdot \vec{n}' = \cos \phi$$

The differential cross-section for elastic scattering of neutrons

Figure 2.5   Simple geometry for the definition of analysing power.

Neutron
Producing
Target

He⁴ Scatterer

$\phi = \pi$

θ

n

k_f

θ'

n'

k'

ϕ

$\phi = 0$
Point Neutron
Detector

k_i

Bombarding
Beam from
Accelerator
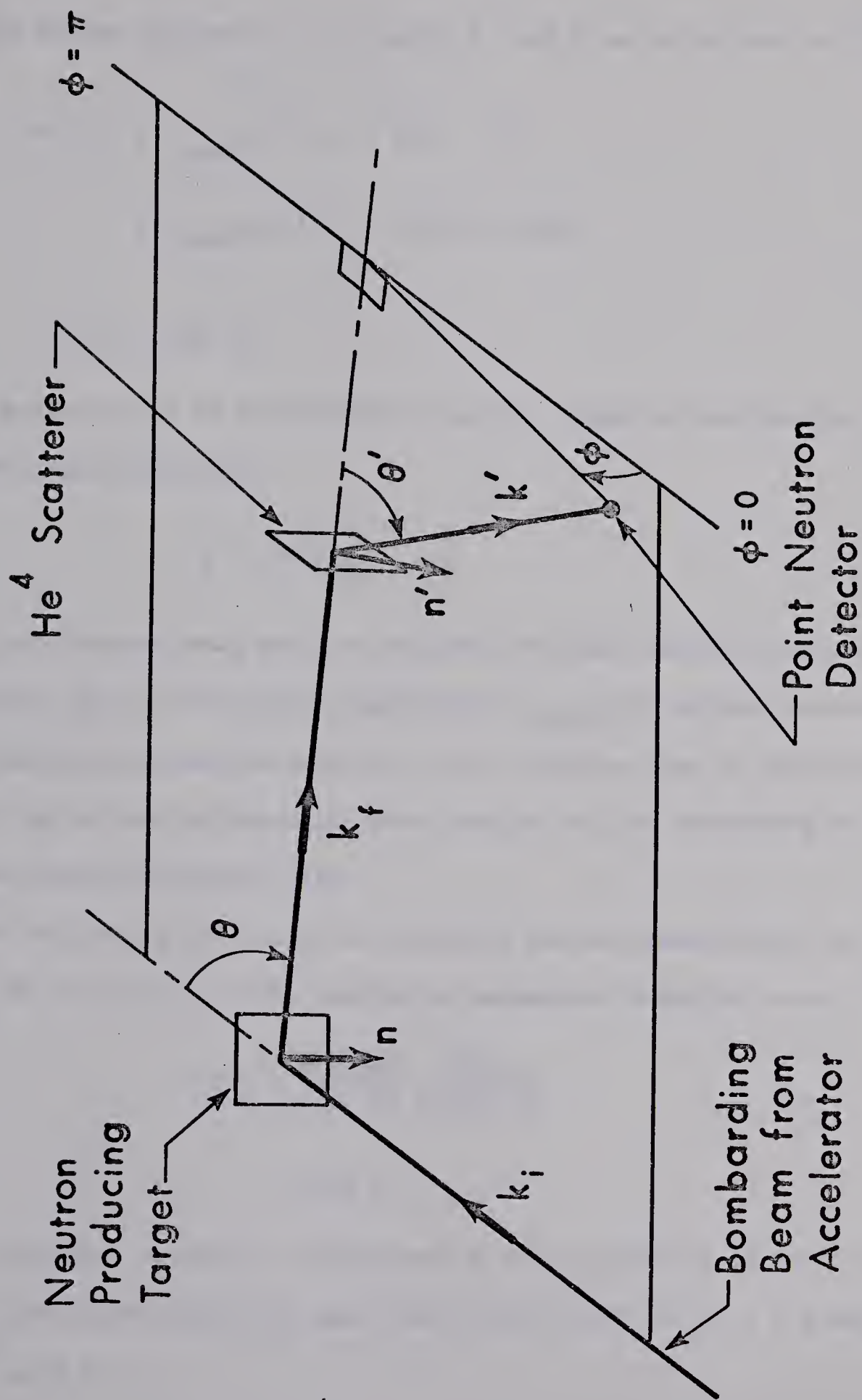
from the helium analyser at the angles θ' and ϕ can be written as (Ha 63)

$$\sigma(\theta',\phi) = \sigma_{unpol}(\theta') \; [1 + \vec{P}(\theta) \cdot \vec{P}']$$

$$= \sigma_{unpol}(\theta') \; [1 + P(\theta) \; P' \; \cos\phi] \qquad (2.1)$$

where
$$\vec{P}(\theta) = P(\theta) \; \vec{n}$$

is the polarization of the neutrons from the target at the reaction angle θ (Basel sign convention),

$$\vec{P}' = P'\vec{n}'$$

is the polarization that would be observed for the scattered neutrons if the initial neutron beam were unpolarized, $\sigma_{unpol}(\theta')$ is the scattering differential cross-section when the initial neutron beam is unpolarized, and $\sigma(\theta',\phi)$ is the differential cross-section for the scattering of neutrons with polarization $\vec{P}(\theta)$.

For fictitious point neutron detectors placed symmetrically at the angles $(\theta',0)$ and (θ',π) the scattering asymmetry is defined to be

$$\varepsilon(\theta) = \frac{\sigma(\theta',0) - \sigma(\theta',\pi)}{\sigma(\theta',0) + \sigma(\theta',\pi)} \qquad (2.2)$$

$$= P(\theta) \; P'$$

This is directly related to the number of events detected in the two neutron detectors during the same time interval $N(\theta',0)$ at $\phi = 0$ and $N(\theta',\pi)$ at $\phi = \pi$.

$$\varepsilon(\theta) \quad = \quad \frac{N(\theta',0) - N(\theta',\pi)}{N(\theta',0) + N(\theta',\pi)} \tag{2.3}$$

For convenience the detector at $(\theta',0)$ will be labelled "right" and the detector at (θ',π) labelled "left," with the number of detected events identified as $R = N(\theta',0)$ and $L = N(\theta',\pi)$. For reaction angles on the opposite side of the accelerator beam $(-\theta)$ a simple rotation of the geometry of figure 2.5 by $180°$ about $\vec{k_i}$ is sufficient to define the labels and sign conventions for the new geometry.

P' is often called the analysing power A of the polarimeter. It can be calculated directly from the known phase shifts derived from differential scattering cross-sections. Hence a measurement of the scattering asymmetry $\varepsilon(\theta)$ is sufficient to determine the polarization of the neutrons produced in the initial reaction.

In a practical case the helium scatterer and the two neutron detectors have finite size. Consequently equation (2.1) must be integrated over the finite geometry to arrive at the proper expression for the detected scattering asymmetry. Double scattering of neutrons in the volume of the helium analyser is also an important factor. A complete calculation in such a case results in replacing the point geometry analysing power A with an effective analysing power A_{eff} to give

$$\varepsilon(\theta) \quad = \quad \frac{R - L}{R + L}$$

$$= \quad A_{eff} \; P(\theta) \tag{2.4}$$

Figure 2.6 The effective (average) analysing power calculated for the polarimeter with a neutron detector threshold of 0.5 MeV. The lower curve includes the effects of finite geometry and double scattering.

VARIATION OF ANALYZING POWER
WITH ENERGY OF INCIDENT NEUTRON
(θ_{DET} = 123° LAB)

POINT SCATTERER
POINT DETECTOR

FINITE GEOMETRY
SINGLE PLUS DOUBLE SCATTER

5% STATISTICAL ERROR
ON PHASE SHIFTS

NEUTRON ENERGY (MeV)

AVERAGE ANALYZING POWER
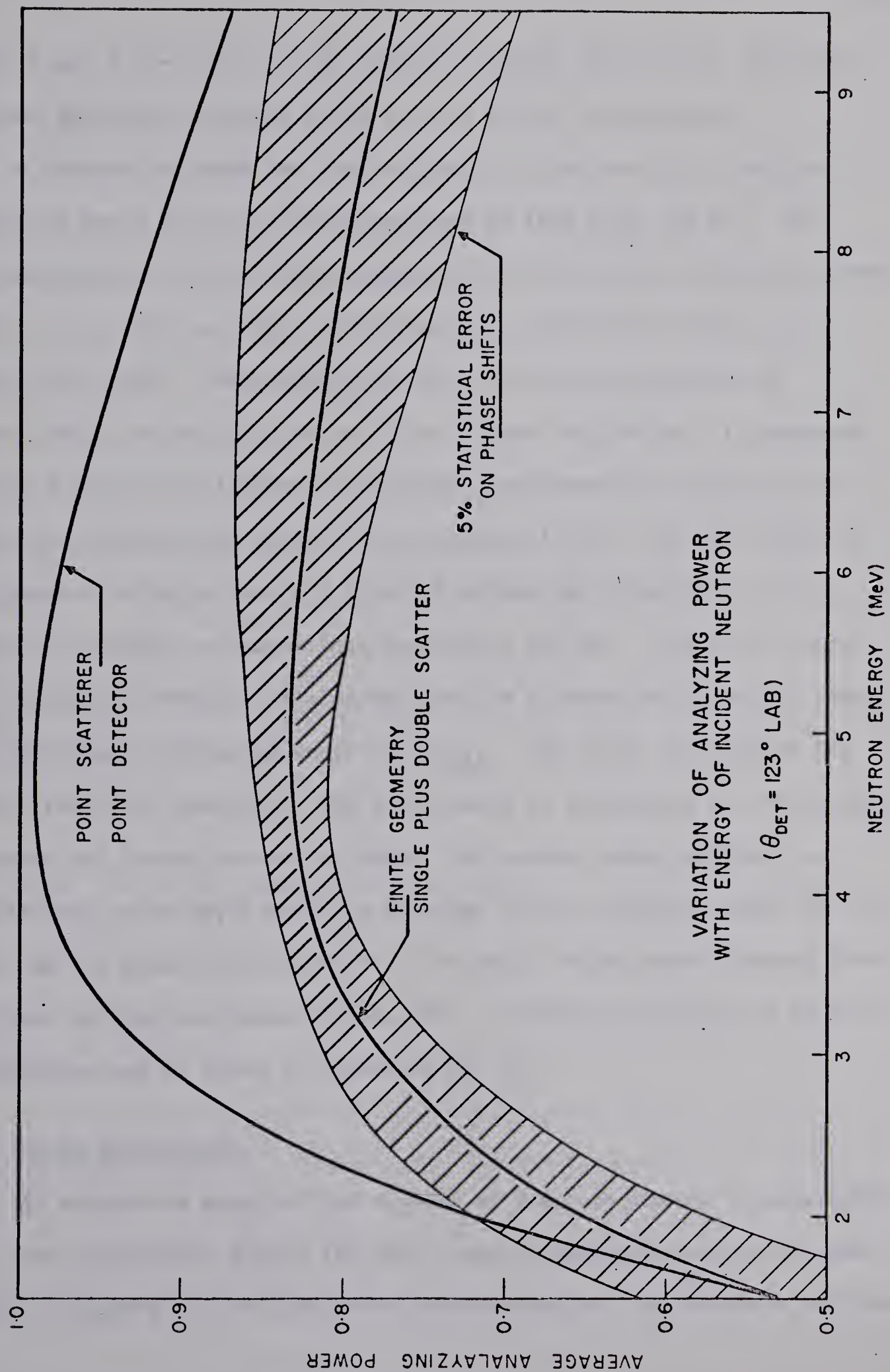
where R and L now refer to the number of counts detected in the finite neutron detectors centered at $(\theta',0)$ and (θ',π) respectively.

A computer program has been written to calculate the effective analysing power for the polarimeter used in this work (St 67). The program accounts for the finite geometry of the cryostat and the neutron detectors as well as double scattering and attenuation within the scattering volume. Depolarization after the first scattering is incorporated in the calculation of the second scattering. In contrast to Monté Carlo calculations the program uses numerical integration of analytical expressions derived from equation (2.1). The efficiency of the neutron detectors for a 0.5 MeV threshold was calculated on the basis of a simple semi-empirical expression (Ob 66). Figure 2.6 shows the calculated effective analysing power as a function of neutron energy for an average scattering angle of 123°_{LAB}. The upper curve shows the result for point geometry. The lower curve is calculated for the finite geometry and double scattering case. The shaded region defines the statistical error which would be obtained in the analysing power if the error in the phase shifts were 5%. The phase shifts were obtained from the work of Hoop and Barschall (Ho 66). A detailed description of this calculation can be found in reference (St 67).

2.6 False Asymmetries

An exhaustive study of the sources of false asymmetry in polarimeters has been reported by Libert (Li 66). These asymmetries can occur from a lack of symmetry in the electronic instrumentation, the detector efficiencies,

or in the physical geometry of the polarimeter. A check for residual asymmetries can be made by analysing the neutrons emitted from a reaction at a 0° reaction angle. Deviations from zero in the detected polarization are due to some source of asymmetry in the polarimeter.

In the polarimeter used in this work the major source of false asymmetry was found to be due to the electronics. Due to the large distances involved in the polarimeter layout a high degree of geometrical symmetry could be achieved. Electronic asymmetries were cancelled by interchanging the roles of the neutron detectors for the second half of each polarization measurement. The principle is as follows. Suppose the detection efficiency of neutron detector A is k times larger than that of detector B. Assuming that for matched detectors the measured ratio of counts in the right detector to the counts recorded in the left neutron detector should be

$$r = \frac{R}{L} \qquad (2.5)$$

then with detector A counting on the right side and with B on the left the expected measured ratio is

$$r_1 = \frac{R_A}{L_B} = \frac{kR}{L} = kr \qquad (2.6)$$

If the roles of the detectors are now interchanged to make B the right detector and A the left detector, then the expected measured ratio will be

$$r_2 = \frac{R_B}{L_A} = \frac{R}{kL} = \frac{r}{k} \qquad (2.7)$$

The geometric mean of equations (2.6) and (2.7) gives

$$\left[\frac{R_A}{L_B} \cdot \frac{R_B}{L_A} \right]^{\frac{1}{2}} = r \qquad (2.8)$$

with the asymmetry caused by k removed. The scattering asymmetry is then calculated as

$$\epsilon(\theta) = \frac{r-1}{r+1} = P(\theta) \, A_{eff} \qquad (2.9)$$

At the forward angles ($\theta < 30^{\circ}_{LAB}$) it was possible to move the polari-meter from one side of the accelerator beam to the other (+θ to -θ) to interchange the roles of the detectors. This method also eliminates false asymmetries due to geometrical differences in the paths between the cryo-stat and each neutron detector. At large reaction angles where space was not available and, of course, at zero degrees the interchange was achieved by exchanging neutron detectors with their electronics on their polariza-tion table mountings. This second method does not eliminate the geometri-cal asymmetries cancelled by the first method.

A possible source of geometrical asymmetry lay in the determination of the zero degree reaction angle. Both positive and negative reaction angles were scanned with the cryostat in measuring the differential cross-section for the $D(d,n)^3He$ reaction. The position of the $\ell_p = 0$ peak in this distribution calibrated the zero degree reaction angle to an estimated error of $\pm 1^{\circ}$.

For each set of runs on the $^{40}Ca(d,n)^{41}Sc$ reaction the polarization at $\theta = 0^{\circ}$ was measured to determine the residual false asymmetry of the

polarimeter. In the two cases the weighted average of the residual

asymmetry over all the observable states amounted to (+0.06 ± 0.14)%

and (+0.06 ± 0.19)%. The observed residual false asymmetry was clearly

negligible.

CHAPTER 3

POLARIZATION MEASUREMENTS AND ANALYSIS

3.1 Target Preparation

Chemical grade calcium metal (97.01% ^{40}Ca natural abundance) was

used to prepare targets. The vacuum evaporation was controlled to yield

targets of approximately 700 $\mu g/cm^2$ thickness on a 0.005 inch thick gold

backing. The targets were handled in a helium atmosphere wherever

possible to minimize carbon and oxygen contamination from the carbon

dioxide and oxygen present in the room atmosphere. Two targets were

prepared in each vacuum evaporation. One was used for the experiment,

while the other target was weighed to determine the target thickness.

Two sets of runs were carried out with two different calcium targets.

With target (1) the reaction angles 0°, 20°, 40°, 60°, 80°, and 100°

(lab) were studied. Target (2) was used to measure the polarization

for 0°, 10°, 30°, 50°, 70°, 90°, 110°, and 120° (lab). The target

thicknesses were (1) 745 $\mu g/cm^2$, and (2) 675 $\mu g/cm^2$, respectively. For

a 6 MeV deuteron bombarding energy the energy loss in target (1) was

55 keV while in target (2) the value was 49.8 keV. These energy losses

were calculated from references Ma 60 and Ri 54. Including an estimated

$\pm$ 5 keV uncertainty in the beam energy calibration and a $\pm$ 5 keV energy

spread due to the Mobley compression system, the above energy losses

yielded an average deuteron bombarding energy of 5.974 $\pm$ 0.039 MeV.

This beam energy was used in all the subsequent data analysis. Since this energy is only 26 keV less than 6 MeV the energy is nominally called 6 MeV in what follows. In the DWBA calculations 6 MeV was the energy used since this figure is well within the experimental error.

3.2 Experimental Conditions

The $^{40}Ca(d,d)^{40}Ca$ and $^{40}Ca(d,n)^{41}Sc$ differential cross-sections have been measured at 5.0, 6.0, and 6.5 MeV (Gr 67, Gr 67a, Le 67, Le 68). The 6.5 MeV energy was ruled out for this experiment because of the difficulty in running the accelerator for long periods of time at such a high energy. The 5.0 MeV deuteron energy would not permit observation of the $^{41}Sc_{2.415}$ state with the polarimeter, since the neutron energy from this state would be below 1.5 MeV. The threshold for reliable operation of the polarimeter is about 2 MeV. At $E_d = 6.0$ MeV the $^{41}Sc_{2.415}$ state yielded neutrons just above 2 MeV. Consequently 6 MeV was chosen for the neutron polarization measurements in the $^{40}Ca(d,n)^{41}Sc$ reaction.

Differential cross-section yield curves for the $^{40}Ca(d,d)^{40}Ca$, $^{40}Ca(d,p)^{41}Ca$, and $^{40}Ca(d,n)^{41}Sc$ reactions were measured by other groups (Gr 67, Gr 67a, Le 67, Le 68) over the energy range from 4.8 MeV to 6.6 MeV (6.2 MeV for the (d,p) reaction). Fluctuations in the cross-sections as a function of energy were less than 10% in the (d,d) and (d,n) reactions, and less than 20% in the (d,p) reaction. This suggests that compound-direct interference is negligible in these reactions (Go 63). This result is not surprising since the 16 MeV excitation energy in the ^{42}Sc

compound nucleus is likely to lie in a continuum region where the level density is high. Such a situation should permit incoherent separation of compound and direct processes.

Average beam currents between 1.8 and 2.5 μA were used. With this range of current a counting rate of about 3×10^3 counts/sec was obtained in the cryostat. Higher counting rates were not used because the peaks in the "random" spectra amounted to about 10% of the height of the corresponding peaks in the "true plus random" spectra.

Figure 3.1 shows a typical time of flight spectrum obtained with the $^{40}Ca(d,n)^{41}Sc$ reaction. The ground, 1.718 and 2.415 MeV states in ^{41}Sc are clearly seen. The 2.096 MeV state of ^{41}Sc is barely visible while the $^{41}Sc_{2.719}$ state is definately not observable. Peaks from the $^{16}O(d,n)^{17}F$ reaction due to oxygen contamination are clearly identified. The $^{13}N_{gnd}$ and $^{13}N_{2.367}$ states from the $^{12}C(d,n)^{13}N$ reaction due to carbon contamination are small enough to be neglected.

At each reaction angle a 5 to 10 minute run was made in the "simple time-of-flight" mode to obtain a spectrum with clear definition of peak shapes and positions. This run was followed by two polarization measure- ments of about 3 hours' duration each. For the second polarization run neutron detectors A and B were interchanged, or the polarimeter was moved to the same angle on the opposite side of the 0° (deuteron beam) position. All three spectra were stored on magnetic tape for data analysis with an off-line computer. The full range of angles was covered in two separate sets of runs as indicated in section 3.1. At the start of each of these two sets the polarization was measured at a reaction

Figure 3.1 A ^{40}Ca(d,n)^{41}Sc time-of-flight spectrum between the target and the cryostat at an angle of 40° (lab). The system was operating in the "simple time-of-flight" mode.

NEUTRON FLIGHT TIME (n sec)

$^{40}Ca (d,n)^{41}Sc$
$E_d = 6.0$ MeV $\theta_{LAB} = 40°$
Flight Path = 2 meters

$^{41}Sc_{gnd}$
$^{13}N_{gnd}$
$^{17}F_{gnd}$
$^{17}F_{0.5}$
$^{41}Sc_{1.718}$
$^{13}N_{2.367}$
$^{41}Sc_{2.096}$
$^{41}Sc_{2.415}$
$^{41}Sc_{2.719}$

CHANNEL NUMBER

COUNTS
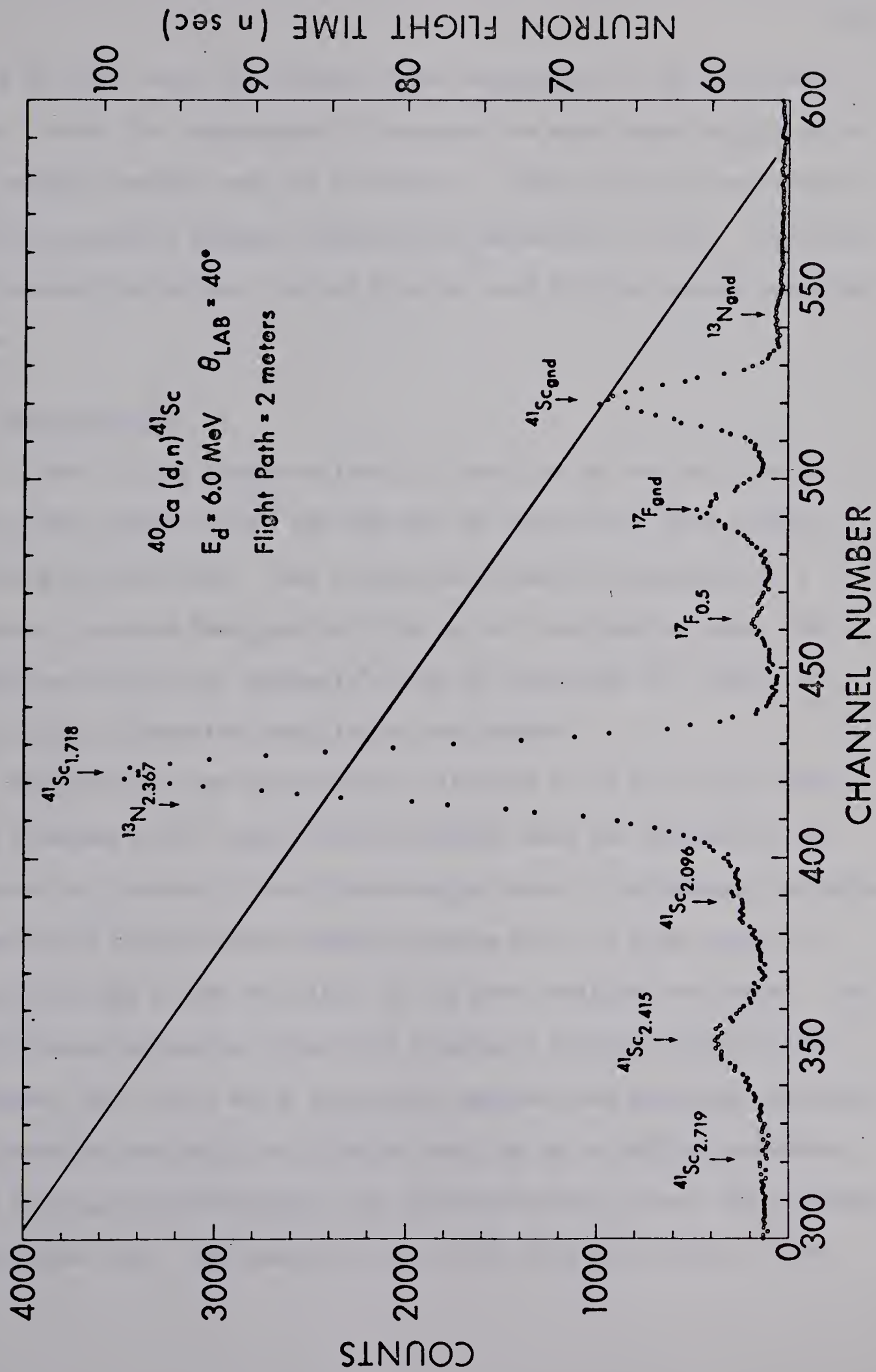
angle of 0° to check for residual false asymmetries in the polarimeter. Table I shows the asymmetries (ε) observed for each state together with the weighted average over all the states. Clearly there is no evidence for any measurable residual asymmetry in either set of runs. The errors are standard deviations obtained from the peak fitting program described below.

3.3 Data Analysis

A peak fitting program written by Tepel (Te 66) and modified for use in this laboratory (Gr 66) was used to analyse the three spectra obtained at each angle. This program estimates the background in a spectrum, searches for peaks and fits up to 5 overlapping peaks. The operation can be fully automatic or can be overridden in a number of ways to use information specified by the operator.

Since the neutron energies were all below 5 MeV the energy resolution observed in the "simple time-of-flight" mode was essentially the same as that observed in the "polarization" mode of polarimeter operation. Hence the 10 minute time-of-flight spectrum with its large number of counts provided a good definition of the peak positions and shapes. The peak fitting program was given full freedom to fit this time-of-flight spectrum. The result was a set of well defined peak positions and widths. The positions and widths so obtained were fed in as initial parameters when fitting the polarization time-of-flight spectra, where the statistics were rather poor. For these fits the widths were held fixed at their

Table I

Residual False Asymmetries at 0°

State	Target(1) $\varepsilon \pm \Delta\varepsilon$	Target(2) $\varepsilon \pm \Delta\varepsilon$
$^{41}Sc_{2.415}$	-0.024 ± 0.028	$+0.0081 \pm 0.026$
$^{41}Sc_{2.096}$ +(other unresolved groups)	-0.023 ± 0.21	$+0.073 \pm 0.039$
$^{41}Sc_{1.718}$	-0.039 ± 0.026	$+0.005 \pm 0.11$
$^{17}F_{0.5}$	$+0.007 \pm 0.013$	-0.022 ± 0.019
$^{17}F_{gnd}$	-0.050 ± 0.066	$+0.305 \pm 0.133$
$^{41}Sc_{gnd}$	$+0.034 \pm 0.023$	$+0.044 \pm 0.038$
$^{13}N_{gnd}$	$+0.009 \pm 0.087$	-0.29 ± 0.33
Weighted Mean	$+0.0006 \pm 0.0014$	$+0.0006 \pm 0.0019$

initial values.[†] All the polarization spectra for a given reaction angle

were treated in an identical fashion by the peak fitting program to as

large a degree as possible. This approach was taken to reduce the

possibility of introducing false asymmetries during data analysis, which

could occur with an unbalanced treatment of left and right spectra. It

would be helpful if the peak fitting program could be modified to include

a fixed peak position option. This feature would be useful in the above

method particularly where the statistics were poor. In the case of the

"random" spectra at reaction angles past about 30° there was essentially

no time uncorrelated background under the peaks, and the program was

instructed to assume zero background. The output of the program gave

peak areas, with standard deviations as errors adjusted for the quality

of the fit. Experience with this program has demonstrated that it gives

an objective and accurate analysis of time-of-flight spectra. One of

the advantages of the program for neutron time-of-flight work is that

it uses a peak shape derived from experiment rather than an analytical

mathematical function for fitting the peaks in a spectrum.

Counts in the "random" spectra were subtracted from the correspond-

ing peaks in the "true plus random" spectra in order to arrive at the

---

[†] This technique cannot be used for neutron energies above about 6
MeV since the cryostat time resolution is significantly better in the
"polarization" mode where the pulse height range is restricted by
kinematics (see section 2.3). Hence peak widths obtained from the
"simple time-of-flight" mode are too large to be used in the polariza-
tion fits at neutron energies above 6 MeV.

"true" counts. These results were then combined to get the right-left ratios for each of the two polarization geometries at the same reaction angle. The two right-left ratios were combined as described in Chapter 2 to arrive at the neutron scattering asymmetry. A conventional statistical error analysis was used to calculate the standard error in the observed asymmetry. These calculations were carried out on a computer by a simple program (CRUTCH) to reduce the time devoted to analysis and the chance of error. The average (effective) analysing power was taken from figure 2.6 to calculate the polarizations.

Tables II to VI list the asymmetries and calculated polarizations for the $^{41}Sc_{gnd}$, $^{41}Sc_{1.718}$, $^{41}Sc_{2.415}$, $^{17}F_{gnd}$, and $^{17}F_{0.5}$ states obtained from the experimental measurements. This data together with differential cross-sections from reference Gr 67 are plotted in figures 3.2 to 3.9. Indicated errors are standard deviations arising from the statistical accuracy of the original data only. Center of mass angles and neutron energies were calculated from a relativistic kinematics program written by T. B. Grandy and J. W. D. Sinclair (Gr 67b).

The large error on the polarization data at 122° in figure 3.2 is due to the presence of the $^{13}N_{gnd}$ peak on the low energy side of the $^{41}Sc_{gnd}$ peak. At angles larger than 80° the $^{17}F_{0.5}$ peak began to move into the high energy side of the $^{41}Sc_{1.718}$ peak to cause the large errors in the polarization data indicated for these angles in figures 3.3 and 3.6. At angles larger than 50° the peak to background ratio for the $^{41}Sc_{2.415}$ state became so small that measurement of the polarization for this state became impractical. Data plotted in this angular range illustrate the inaccuracy

Table II

$^{40}Ca(d,n)^{41}Sc_{gnd}$ Polarization

Center of Mass Angle θ (degrees)	Neutron Energy (MeV)	Analysing Power A_{eff}	Asymmetry $\varepsilon \pm \Delta\varepsilon$	Polarization $P \pm \Delta P$
10.4	4.783	0.832	-0.076±0.033	-0.091±0.040
20.8	4.766	0.832	-0.011±0.026	-0.013±0.031
31.1	4.738	0.832	-0.002±0.034	-0.002±0.041
41.5	4.701	0.832	-0.073±0.022	-0.088±0.026
51.7	4.655	0.832	-0.045±0.033	-0.054±0.040
62.0	4.603	0.831	-0.007±0.018	-0.008±0.022
72.1	4.546	0.831	-0.087±0.034	-0.105±0.041
82.2	4.485	0.830	-0.072±0.027	-0.087±0.033
92.3	4.424	0.829	-0.101±0.037	-0.122±0.045
102.2	4.364	0.828	-0.094±0.021	-0.114±0.025
112.1	4.306	0.828	-0.101±0.044	-0.122±0.053
122.0	4.253	0.827	-0.192±0.15	-0.232±0.181

Table III

$^{40}Ca(d,n)^{41}Sc_{1.718}$ Polarization

Center of Mass Angle θ (degrees)	Neutron Energy (MeV)	Analysing Power A_{eff}	Asymmetry $\varepsilon \pm \Delta\varepsilon$	Polarization $P \pm \Delta P$
10.5	3.032	0.776	+0.026±0.011	+0.034±0.014
21.0	3.019	0.775	+0.014±0.012	+0.018±0.015
31.4	2.997	0.773	+0.003±0.014	+0.004±0.019
41.9	2.967	0.771	-0.068±0.017	-0.088±0.022
52.2	2.930	0.768	-0.034±0.019	-0.044±0.025
62.5	2.889	0.765	-0.096±0.019	-0.125±0.026
72.7	2.844	0.761	-0.032±0.017	-0.042±0.022
82.8	2.795	0.757	-0.021±0.016	-0.028±0.021
92.9	2.747	0.752	-0.022±0.022	-0.029±0.029
102.8	2.700	0.747	-0.052±0.025	-0.070±0.034
112.7	2.655	0.743	+0.277±0.518	+0.373±0.697
122.5	2.613	0.737	-0.055±0.112	-0.075±0.152

Table IV

$^{40}Ca(d,n)^{41}Sc_{2.415}$ Polarization

Center of Mass Angle θ (degrees)	Neutron Energy (MeV)	Analysing Power A_{eff}	Asymmetry $\varepsilon \pm \Delta\varepsilon$	Polarization $P \pm \Delta P$
10.6	2.316	0.703	-0.074 ± 0.025	-0.105 ± 0.036
21.1	2.304	0.701	-0.007 ± 0.027	-0.010 ± 0.039
31.7	2.285	0.698	-0.158 ± 0.050	-0.226 ± 0.074
42.1	2.259	0.696	-0.179 ± 0.062	-0.257 ± 0.091
52.5	2.227	0.692	$+0.029\pm0.159$	$+0.042\pm0.230$
62.9	2.190	0.687	-0.038 ± 0.094	-0.055 ± 0.136
73.1	2.150	0.678	-0.268 ± 0.519	-0.395 ± 0.766
83.3	2.109	0.672	$+0.111\pm0.969$	$+0.165\pm1.44$
93.3	2.067	0.665	-0.298 ± 0.510	-0.448 ± 0.768
103.3	2.026	0.659	-0.039 ± 0.256	-0.059 ± 0.387
113.1	1.987	0.652	$+0.327\pm0.558$	$+0.502\pm0.856$
122.9	1.951	0.644	$+0.703\pm2.711$	$+1.09 \pm4.2$

Table V

$^{16}O(d,n)^{17}F_{gnd}$ Polarization

Center of Mass Angle θ (degrees)	Neutron Energy (MeV)	Analysing Power A_{eff}	Asymmetry $\epsilon \pm \Delta\epsilon$	Polarization $P \pm \Delta P$
11.0	4.243	0.827	-0.190 ± 0.095	-0.230 ± 0.115
22.0	4.204	0.827	-0.076 ± 0.032	-0.092 ± 0.039
33.0	4.140	0.826	-0.073 ± 0.022	-0.088 ± 0.027
43.8	4.055	0.824	-0.086 ± 0.037	-0.104 ± 0.045
54.6	3.952	0.822	$+0.044\pm0.039$	$+0.054\pm0.048$
65.2	3.836	0.819	$+0.112\pm0.077$	$+0.137\pm0.094$
75.6	3.711	0.814	$+0.151\pm0.062$	$+0.186\pm0.077$
85.9	3.583	0.810	-0.057 ± 0.177	-0.070 ± 0.217
96.0	3.456	0.804	-0.029 ± 0.096	-0.036 ± 0.119
105.9	3.333	0.797	-0.004 ± 0.064	-0.005 ± 0.080
115.6	3.217	0.790	$+0.095\pm0.096$	$+0.120\pm0.122$
125.2	3.113	0.782	$+0.039\pm0.038$	$+0.050\pm0.049$

Table VI

$^{16}O(d,n)^{17}F_{0.5}$ Polarization

Center of Mass Angle θ (degrees)	Neutron Energy (MeV)	Analysing Power A_{eff}	Asymmetry $\varepsilon \pm \Delta\varepsilon$	Polarization $P \pm \Delta P$
11.1	3.727	0.815	$+0.018\pm0.024$	$+0.022\pm0.029$
22.2	3.689	0.814	$+0.053\pm0.029$	$+0.065\pm0.036$
33.2	3.629	0.812	-0.195 ± 0.036	-0.240 ± 0.045
44.1	3.549	0.808	-0.609 ± 0.116	-0.754 ± 0.146
54.9	3.452	0.804	-0.311 ± 0.061	$-0.387+0.077$
65.6	3.343	0.798	-0.202 ± 0.108	-0.253 ± 0.136
76.0	3.227	0.791	-0.199 ± 0.072	-0.252 ± 0.153
86.3	3.107	0.782	-0.666 ± 0.660	-0.852 ± 0.845
96.4	2.988	0.773	-0.475 ± 0.175	-0.614 ± 0.228
106.3	2.874	0.762	-0.379 ± 0.207	-0.497 ± 0.273

of the measurement. Since the oxygen was regarded as an undesirable

contaminant an attempt was made to minimize its presence in the target.

Consequently the polarization data presented for the $^{17}F_{gnd}$ and $^{17}F_{0.5}$

states show poor statistical accuracy. More will be said about this

reaction in a later section.

3.4 DWBA Calculations

A DWBA computer code written by L. Hutton (Hu 67, Al 67) was used

to give theoretical predictions for the $^{40}Ca(d,n)^{41}Sc$ differential

cross-sections and neutron polarizations. This program is capable of

performing approximate non-local (Pe 62, Fi 66, Pe 63) and finite-range

calculations. The local and finite-range options were adopted for the

following calculations. One of the advantages of Hutton's program is

that it permits calculations at low binding energies. For the two unbound

states in ^{41}Sc the binding energy of the captured proton could be set as

low as 200 keV without causing computational difficulties. The program

employed potentials for the incoming and outgoing channels as described

in equation 1.2. The potentials described in equation 1.27 were used for

the captured particle.

Neutron parameters for the outgoing channel were obtained from a

survey of the field listed in reference Ro 66. The two different sets

obtained by Perey and Rosen (Ro 66) were tried. The deuteron parameters

obtained by Leighton et al (Le 67, Le 68) were used for the entrance

channel. These parameters provided a smooth extension of the average

deuteron parameters obtained by Basel et al at higher bombarding

energies (Ba 64, Le 64). It is well known that the deuteron elastic

scattering differential cross-sections are extremely insensitive to the

spin-orbit potential (Pe 67, Pe 66). There seems to be little point in

attempting to determine this parameter from deuteron elastic scattering

cross-sections. For this reason the deuteron parameters of Leighton et al

were derived with the omission of the spin-orbit potential (Pe 67). It

was hoped that the polarization data from the (d,n) and (d,p) reactions

would give a clearer indication of the proper value for this spin-orbit

potential. With the rest of the deuteron parameters, and all of the

neutron and proton parameters fixed, the only parameterization left in the

stripping prediction is the spin-orbit potential. The radius and diffuse-

ness of the deuteron spin-orbit potential were fixed at the same values

as for the real potential.
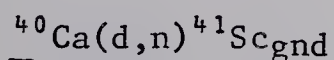
$^{40}Ca(d,n)^{41}Sc_{gnd}$

Figure 3.2 shows the DWBA predictions for the differential cross-

section and neutron polarization in the $^{40}Ca(d,n)^{41}Sc_{gnd}$ reaction.

Differential cross-section data were taken from reference Gr 67. The

four curves represent the results when the deuteron spin-orbit potential

was set at V_S = 0, 6.5, 13, and 19.5 MeV. Values of the other parameters

are listed in table VII. Perey's neutron parameters were used in figure

3.2. Agreement with the polarization data is fair only for the 13 MeV

and 19.5 MeV spin-orbit potentials, with some preference for the higher

value. The predicted cross-sections are in complete disagreement with

the experimental data. It is not reasonable to assume that the major

cause of discrepancy is the spectroscopic factor, since a value greater

than unity would be required. The absolute cross-section calibration

Figure 3.2   DWBA predictions for the differential cross-section and neutron polarization for the $^{40}Ca(d,n)^{41}Sc_{gnd}$ reaction.   The deuteron bombarding energy is nominally $E_d = 6.0$ MeV.   The four curves represent predictions with the deuteron spin-orbit potential ($V_{so} = V_s$) set at 0, 6.5, 13, and 19.5 MeV. $\ell_p = 3$, $j = \ell_p + \frac{1}{2} = J^\pi = \frac{7^-}{2}$.

DIFFERENTIAL CROSS-SECTION

$^{40}Ca(d,n)^{41}Sc_{gnd}$

$\frac{d\sigma}{d\Omega}$ mb/sr

$V_{SO} = 0$
$V_{SO} = 6.5$ MeV
$V_{SO} = 13$ MeV
$V_{SO} = 19.5$ MeV

θ_{CM}

POLARIZATION

$P(\theta)$

θ_{CM} (degrees)
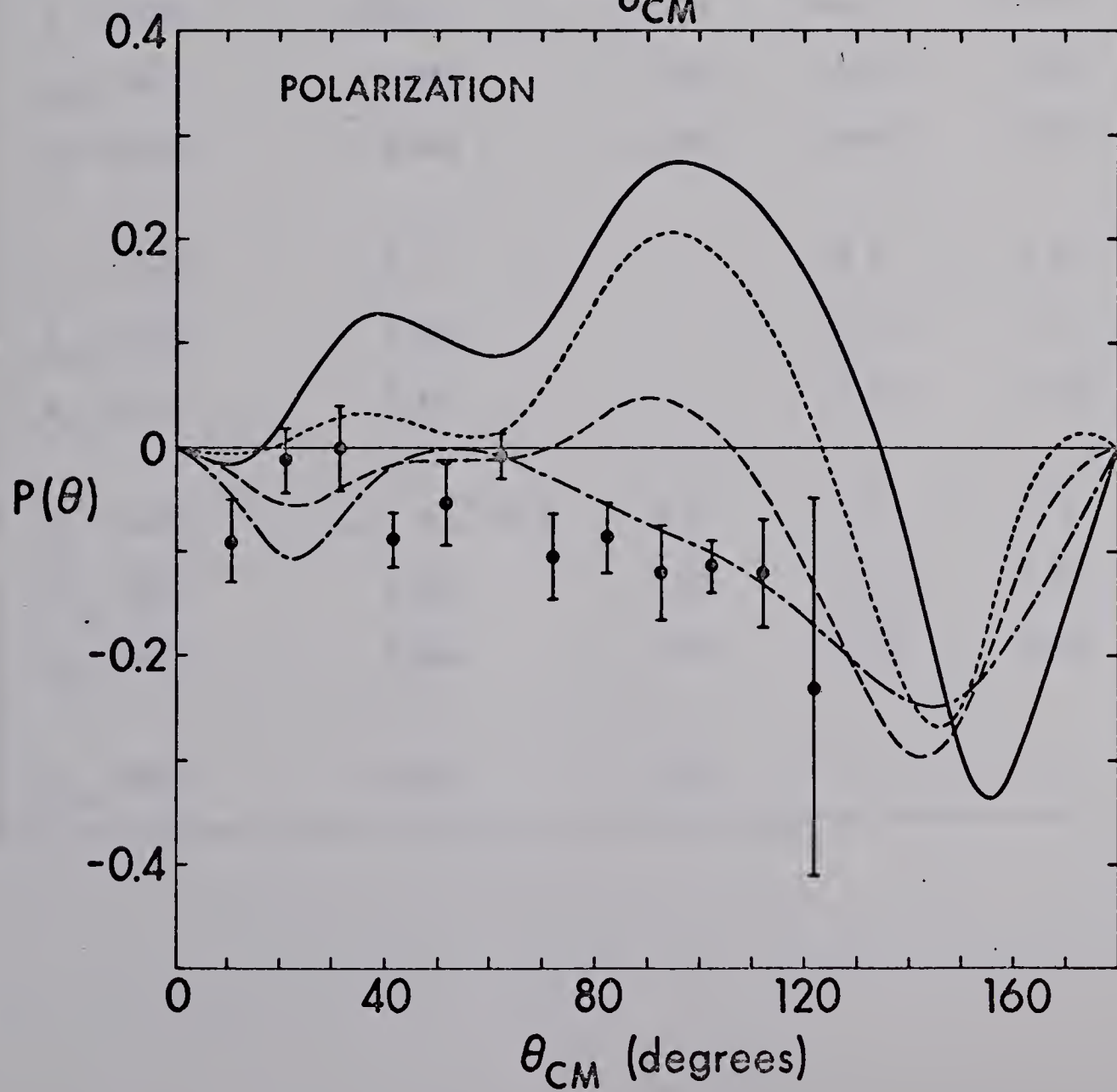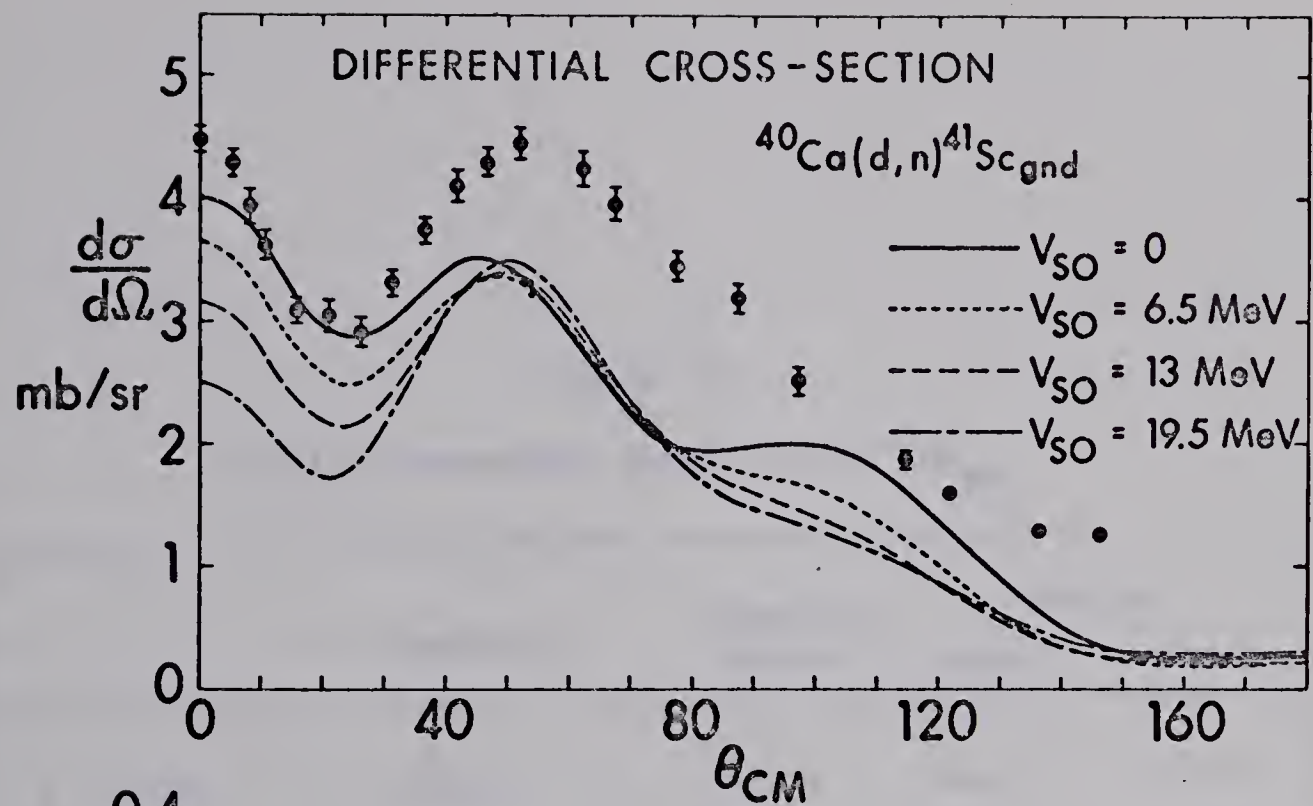
Table VII

Optical Potentials for $^{40}Ca(d,n)^{41}Sc_{gnd}$

		Deuteron	Captured Proton	Neutron Perey	Neutron Rosen
V	(MeV)	110.0	53.34	46.6	47.7
r_{OR}	(fm)	1.065	1.25	1.27	1.25
a_R	(fm)	0.806	0.65	0.66	0.65
W	(MeV)	9.9		9.6	5.75
r_{OI}	(fm)	1.568		1.27	1.25
a_I	(fm)	0.55		0.47	0.70
V_S	(MeV)	0, 6.5, 13, 19.5	6.5	7.2	5.5
r_{OS}	(fm)	1.065	1.25	1.25	1.25
a_S	(fm)	0.806	0.65	0.66	0.65
r_{oc}	(fm)	1.25	1.25		

could be in error by as much as 20% (Gr 67) but a renormalization of the

experimental data would not improve the agreement substantially at the

larger angles. One interesting feature of the curve for the 13 MeV

spin-orbit potential is that it is offset from the experimental data by

an almost constant amount throughout the entire range of angles. In

light of the large observed cross-section at back angles one is tempted

to attribute this to compound nucleus reaction contributions. One might

assume that the compound nucleus reaction differential cross-section is

a very weak function of angle. If, on this basis, a flat 1 mb/sr is

subtracted from the experimental data, the fit shown in figure 3.3 is

obtained. The solid curve is the prediction from figure 3.2 with the

13 MeV spin-orbit potential . This result tends to suggest that a spin-

orbit potential in the neighbourhood of 13 MeV is appropriate for the

deuteron. It is, of course, unsafe to assume that the disagreement at

large angles in figure 3.2 is due to compound nucleus formation. DWBA

predictions frequently disagree with experiment for angles larger than

60°. It is interesting to note that the ^{40}Ca(d,p)^{41}Ca cross-section

is also underestimated at E_d = 6.0 MeV (by $\approx$ 0.5 mb/sr) at large angles

using similar potentials (V_s = 0) (Le 67). At higher energies (Le 64)

the agreement has been found to be fairly good at large angles.[†] This

observation tends to support the suspicion of compound nucleus effects.

Clearly, Hauser-Feshbach calculations are required to resolve the

question of compound nucleus contributions (Go 63). At the time this

---

[†]Lee et al calculated a compound nucleus cross-section of $\leq$ 0.14
mb/sr at energies above 7 MeV (Le 64).

Figure 3.3   Polarization and differential
cross-section data from figure 3.2 with
1 mb/sr subtracted from the experimental
cross-section. The solid curve is the
prediction from figure 3.2 with a 13 MeV
deuteron spin-orbit potential and Perey's
neutron parameters. The dashed curve is
the same prediction using Rosen's neutron
parameters.

DIFFERENTIAL CROSS-SECTION

$^{40}Ca(d,n)^{41}Sc_{gnd}$

——— Perey
- - - - Rosen
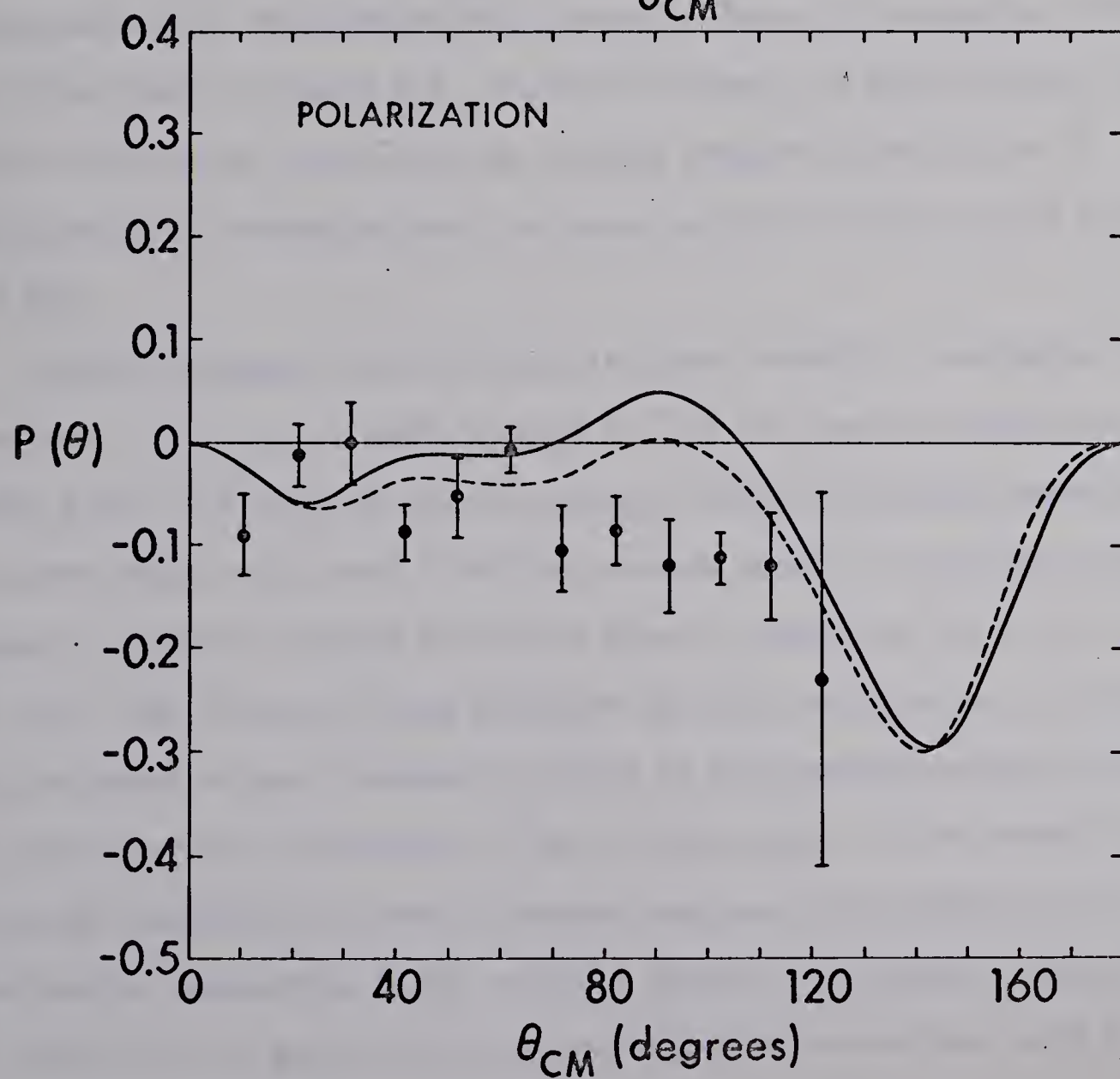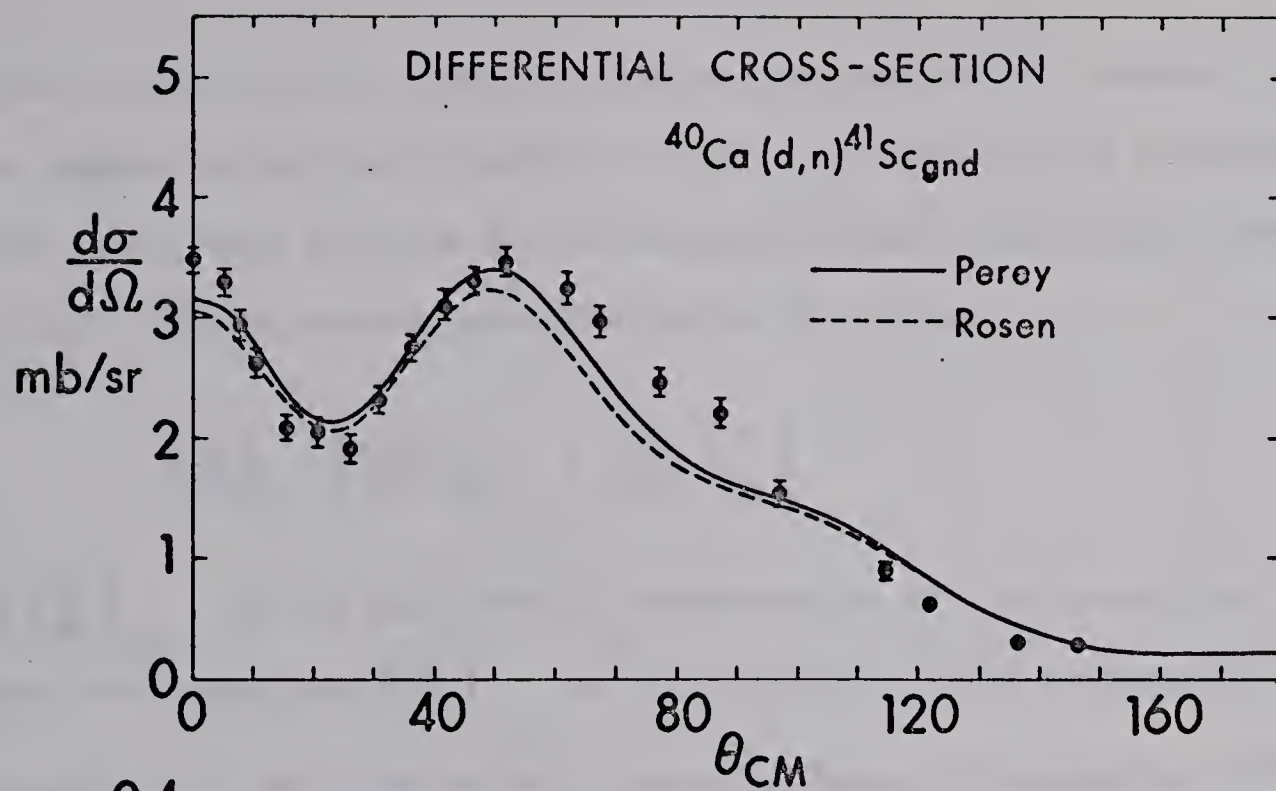
POLARIZATION

work was performed such a computer code was not available. However, work

is now proceeding in this direction. If the compound nucleus contributions

produce unpolarized neutrons in the outgoing channel, then there is an

attenuation in the observed polarization by the factor

$$\left(\frac{d\sigma}{d\Omega}\right)_{DI} \cdot \left[\left(\frac{d\sigma}{d\Omega}\right)_{DI} + \left(\frac{d\sigma}{d\Omega}\right)_{CN}\right]^{-1}$$

where $\left(\frac{d\sigma}{d\Omega}\right)_{DI}$ is the differential cross-section for the direct interaction

process (stripping) and $\left(\frac{d\sigma}{d\Omega}\right)_{CN}$ is the compound nucleus differential

cross-section to the same outgoing channel. There is no apparent evidence

for this effect in figure 3.2. On the other hand, it seems unlikely that

nature would be so cooperative as to yield complete cancellation of

polarization in averaging over the levels excited in the compound nucleus

(Go 63).

Another compound nucleus effect may cause trouble in analysing this

reaction. For all the levels excited in ^{41}Sc the neutron energies are

below 5 MeV. It has been found in neutron elastic scattering experiments

on other nuclei that below 6 MeV the compound elastic scattering process

begins to compete strongly with shape elastic scattering (Ro 65, Ro 65a,

Ro 66). This effect has been explained (Ro 65a) as being due to a decrease

in the number of open channels for decay of the compound nucleus formed

by the target plus the neutron (^{42}Sc in this case). If the probability

of decay through other channels becomes very small, the probability of

the neutron reappearing in the entrance channel is increased. Hence it

is likely that an appreciable compound elastic cross-section would be

observed if a neutron elastic scattering experiment on ^{41}Sc were performed.

However, the nucleus is radioactive and the experiment is not feasible.

The precise significance of such a compound nucleus effect is not obvious.

One conclusion which could be drawn is the following. In the (d,n) and

(d,p) reactions at high energies the compound nucleus (^{42}Sc), if formed,

has a large number of channels open for decay. Hence the cross-section

for decay to any one of these channels is small. Consequently, at these

energies very little compound nucleus contribution should be observed in

the (d,p) and (d,n) reactions. At low energies, where neutron scattering

indicates very few channels are open for compound nucleus decay, the

decay probability of the compound nucleus back into the entrance channel

and into the (d,n) and (d,p) exit channels should be much higher. Hence

one might expect to see significant compound nucleus contributions in

the (d,d), (d,n), and (d,p) reactions in question here. It is probably

not safe to extrapolate from neighbouring nuclei since the compound

nucleus effects will depend on level density, Q values, and spins. Again

this question requires more detailed study with a Hauser-Feshbach calcula-

tion. The above argument does indicate, however, the expected result of

the calculation.

The effect of the compound elastic scattering in the neutron channel

which is not clear is the extent to which the elastic scattering wave

functions as used in the DWBA calculation are perturbed. In the calcula-

tions reported here the wave function pertaining to shape elastic scatter-

ing alone has been used. One might expect the decay mode in the compound

elastic scattering to have little effect on the shape elastic wave function (unless compound-direct interference is strong). Except for the energy dependence of the neutron channel transmission coefficient (Go 63) the probability of formation of the compound nucleus in neutron elastic scattering is not strongly different at low and high energies. Thus the imaginary neutron potential should not show a strong dependence on the compound elastic scattering cross-section. The above argument suggests that the shape elastic wave function extrapolated from higher energies should be used in the DWBA calculations . The compound nucleus effects should simply provide an incoherent contribution to the cross-section between entrance and exit channels. If, on the other hand, compound-direct interference effects are important in the neutron channel, then the Born approximation is not valid and the DWBA calculation is inadequate.

It should be kept in mind that the above compound nucleus arguments are necessarily intuitive (Go 63), and serve only to point out possibilities that should be investigated when the appropriate means become available. Some of the concepts argued are fairly well established (Ro 65, Ro 65a, Ro 66, Go 63).

In table VII the differences between Perey's and Rosen's potentials are noticeable primarily in the depth and diffuseness of the imaginary potential and the strength of the spin-orbit potential. In figure 3.3 the DWBA predictions with the two sets of neutron potentials are compared for a 13 MeV deuteron spin-orbit potential. The differences in the predicted cross-section and polarization are small. One advantage in the

potentials supplied by Rosen is the fact that they were derived from fits

to elastic scattering prolarization data. Hence the spin-orbit potential

should be determined fairly accurately.

There are other reasons why the theory may be unable to predict the

observed cross-section and polarization. First of all, the proton is

captured with $\ell_p = 3$. As Buck and Rook point out (Bu 65), the DWBA

approach should encounter difficulty at such a high ℓ-value. Another

weak point may be the omission of the d-state in the deuteron wave function.

It has been shown recently (Jo 67) that the d-state can contribute to

strong j-dependent effects in the differential cross-section, producing

different shapes for $j = \ell + \frac{1}{2}$ and $j = \ell - \frac{1}{2}$ transitions. In the past

such effects have been pointed out at angles near 100° and close to 0°

(La 67, Da 66, Le 64a, Bu 66). The deuteron spin-orbit potential in

figure 3.2 also seems to affect the cross-section most in these two

regions.

It would appear from the fits to the $^{41}Sc_{gnd}$ state that a deuteron

spin-orbit potential in the vicinity of 13 MeV is required. Even with

this choice the agreement with experiment is not good. It is hoped

that fits to the $^{40}Ca(d,p)^{41}Ca$ differential cross-section and proton

polarization data will help to make the assignment more conclusive.

Preliminary results of the proton polarization work (Le 67a) indicate

close agreement with the magnitude and features of the neutron polari-

zation reported here. It is expected that more definite conclusions will

be possible when the measurements for both the (d,p) and (d,n) reactions

are available and Hauser-Feshbach calculations can be carried out. At

present the program for a thorough study of the reactions on ^{40}Ca is only partly completed.

^{40}Ca(d,n)^{41}Sc$_{1.718}$ and ^{40}Ca(d,n)^{41}Sc$_{2.415}$

Figures 3.4 and 3.5 show the DWBA predictions for the ^{41}Sc$_{1.718}$ and ^{41}Sc$_{2.415}$ states. Both these states are unbound. A proper solution for the captured proton should, therefore, yield an unbound state wave-function. To date, computer programs to treat the unbound state stripping calculation are not available. The best one can do is to assume the state is bound and set the binding energy at as low a value as the computer code is able to handle in the calculation. Clearly, the wave-function computed by the program is not the correct one. The effect of using a binding energy larger than the true value is a reduction in the predicted cross-section (Le 64). The reduction is largest at forward angles and decreases slowly with increasing angle, until in the backward direction the cross-section is unchanged.

Since the absolute cross-sections for these unbound states have little significance, the predictions were multiplied by 1.82 for the ^{41}Sc$_{1.718}$ cross-sections and by 0.257 for the ^{41}Sc$_{2.415}$ state. The four curves shown in figures 3.4 and 3.5 are for the four values of the deuteron spin-orbit potential V_S = 0, 6.5, 13, and 19.5 MeV. The bind-ing energy was arbitrarily fixed at 200 keV for both states. Potentials used in the DWBA calculations are listed in tables VIII and IX.

Very little can be concluded from the DWBA predictions since such a drastic approximation has been made for the proton wave function. The

Figure 3.4   Differential cross-section and polarization for ^{40}Ca$(d,n)^{41}$Sc$_{1.718}$.   The DWBA calculations are for the deuteron spin-orbit potential values 0, 6.5, 13, and 19.5 MeV.   The theoretical cross-sections have been multiplied by 1.82.   A binding energy of 200 keV was used in the calculation. $E_d = 6$ MeV, $\ell_p = 1$, $j = \ell_p + \frac{1}{2} = J^{\pi} = \frac{3^-}{2}$.

DIFFERENTIAL CROSS-SECTION
$^{40}Ca(d,n)^{41}Sc_{1.718}$

$\dfrac{d\sigma}{d\Omega}$ mb/sr

$V_{SO} = 0$
$V_{SO} = 6.5$ MeV
$V_{SO} = 13$ MeV
$V_{SO} = 19.5$ MeV

θ_{CM}

POLARIZATION

$P(\theta)$

θ_{CM} (degrees)

Table VIII

Optical Potentials for $^{40}Ca(d,n)^{41}Sc_{1.718}$

		Deuteron	Captured Proton	Neutron Perey	Rosen
V	(MeV)	110.0	56.83	47.1	48.3
r_{OR}	(fm)	1.065	1.25	1.27	1.25
a_R	(fm)	0.806	0.65	0.66	0.65
W	(MeV)	9.9		9.6	5.75
r_{OI}	(fm)	1.568		1.27	1.25
a_I	(fm)	0.55		0.47	0.70
V_S	(MeV)	0, 6.5, 13, 19.5	6.5	7.2	5.5
r_{OS}	(fm)	1.065	1.25	1.25	1.25
a_S	(fm)	0.806	0.65	0.66	0.65
r_{oc}	(fm)	1.25	1.25		

Figure 3.5   Differential cross-section and polarization for ^{40}Ca(d,n)^{41}Sc$_{2.415}$.   The DWBA calculations are for a deuteron spin-orbit potential $V_{so} = V_S = 0$, 6.5, 13, and 19.5 MeV.   The theoretical cross-sections have been multiplied by 0.257.   A binding energy of 200 keV was used for the calculation. $E_d = 6$ MeV, $\ell_p = 1$, $j = \ell_p + \frac{1}{2} = J^{\pi} = \frac{3^-}{2}$.
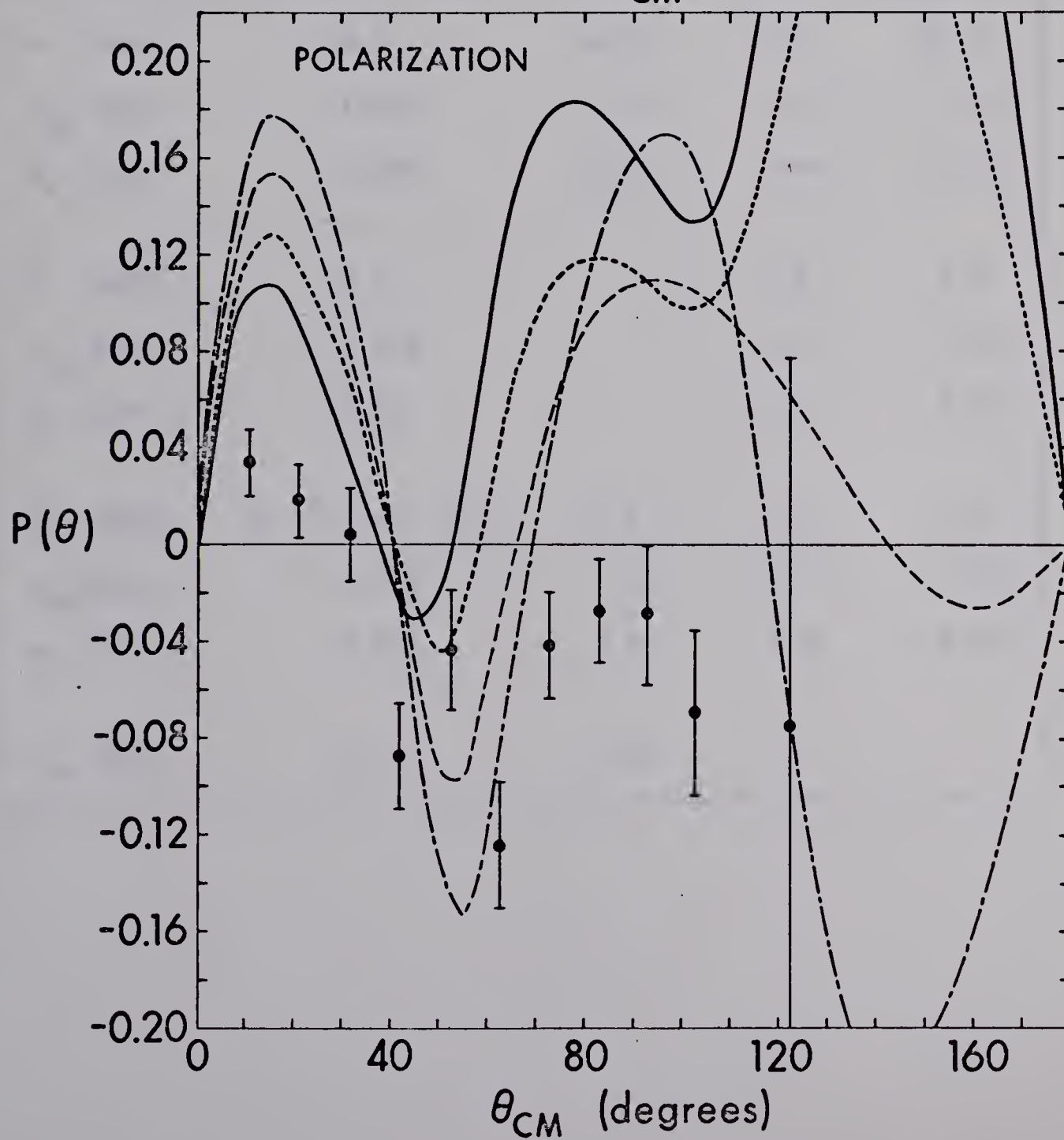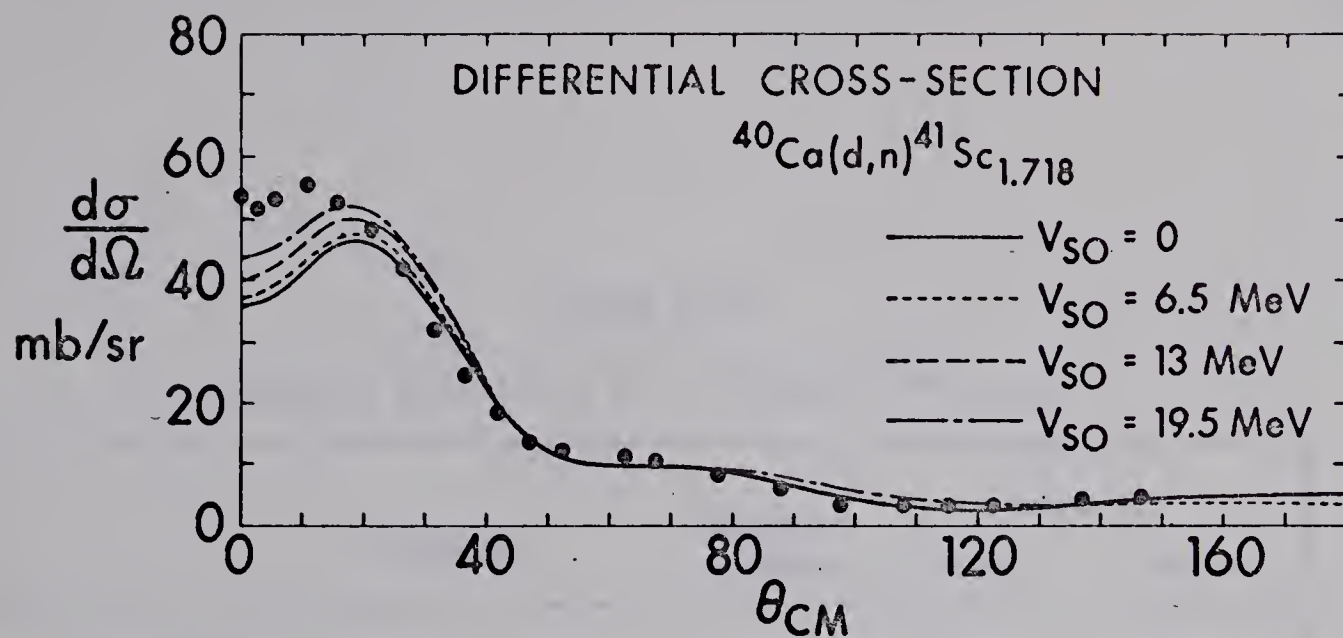
DIFFERENTIAL CROSS-SECTION
^{40}Ca(d,n)^{41}Sc$_{2.415}$

$\frac{d\sigma}{d\Omega}$
mb/sr

V_{SO} = 0
V_{SO} = 6.5 MeV
V_{SO} = 13 MeV
V_{SO} = 19.5 MeV

POLARIZATION

$P(\theta)$

θ_{CM} (degrees)
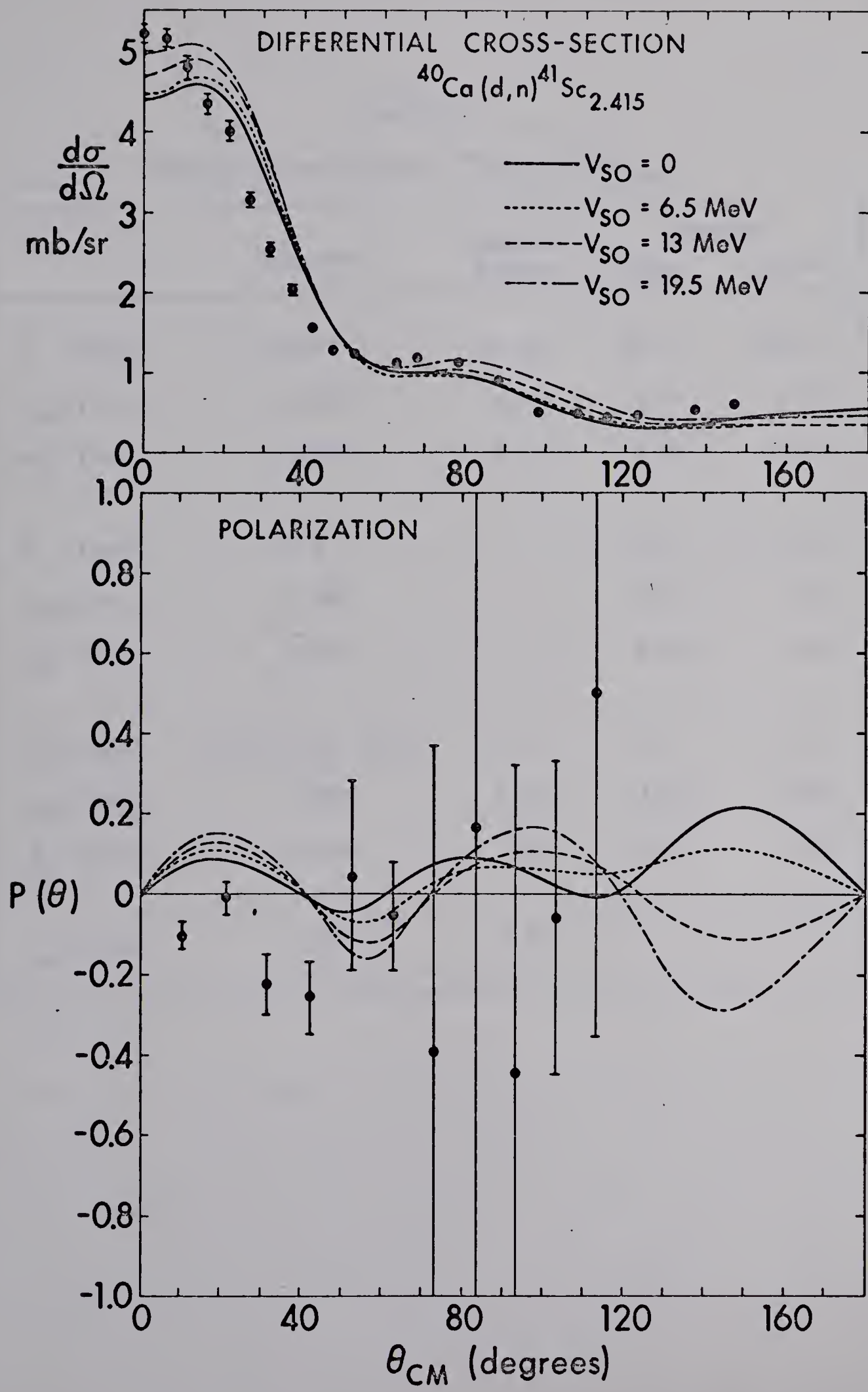
Table IX

Optical Potentials for $^{40}Ca(d,n)^{41}Sc_{2.415}$

		Deuteron	Captured Proton	Neutron Perey	Neutron Rosen
V	(MeV)	110.0	56.83	47.3	48.5
r_{OR}	(fm)	1.065	1.25	1.27	1.25
a_R	(fm)	0.806	0.65	0.66	0.65
W	(MeV)	9.9		9.6	5.75
r_{OI}	(fm)	1.568		1.27	1.25
a_I	(fm)	0.55		0.47	0.70
V_S	(MeV)	0, 6.5, 13, 19.5	6.5	7.2	5.5
r_{OS}	(fm)	1.065	1.25	1.25	1.25
a_S	(fm)	0.806	0.65	0.66	0.65
r_{oc}	(fm)	1.25	1.25		

polarization data for the $^{41}Sc_{1.718}$ state does show a tendency to follow the oscillation pattern in the predicted polarization. However, the magnitude and the sign do not exhibit satisfactory agreement.

Both these states are formed by $\ell_p = 1$ transitions and have a spin of $\frac{3}{2}$. As mentioned earlier, Gerace and Green (Ge 67c) have shown that the 2.415 MeV level arises from mixing of a rotational state with the $2p_{\frac{3}{2}}$ single-particle level at 1.718 MeV. Hence the $2p_{\frac{3}{2}}$ single-particle strength is shared by these two states in the $^{40}Ca(d,n)^{41}Sc$ reaction. The presence of deformation in ^{41}Sc also raises doubt as to the validity of using a single-particle wave function in the DWBA calculation for the ground state (Le 64).

Figures 3.6 and 3.7 show the data from figures 3.4 and 3.5 with a comparison between the use of Rosen's and Perey's neutron parameters. The deuteron spin-orbit potential was 13 MeV. Again the differences are not large, except perhaps at the forward angles in the differential cross-section.

The data for the $^{41}Sc_{2.415}$ and $^{41}Sc_{1.718}$ states offer no conclusive evidence regarding the deuteron spin-orbit strength.

$^{16}O(d,n)^{17}F$

Figures 3.8 and 3.9 show the differential cross-sections and neutron polarizations for $^{16}O(d,n)^{17}F_{gnd}$ and $^{16}O(d,n)^{17}F_{0.5}$. The cross-sections are taken from reference Gr 67. In figure 3.8 a DWBA prediction using parameters taken from Alty et al (Al 67a) at higher energies is shown. The parameters used in the calculation are listed in table X. Since the

Figure 3.6   Fits to the data of figure 3.4
comparing Perey's and Rosen's neutron para-
meters.   The deuteron spin-orbit potential
is 13 MeV.   The DWBA cross-sections have been
multiplied by 1.82.

DIFFERENTIAL CROSS-SECTION

$^{40}Ca(d,n)^{41}Sc_{1.718}$

—— Perey

- - - Rosen

POLARIZATION
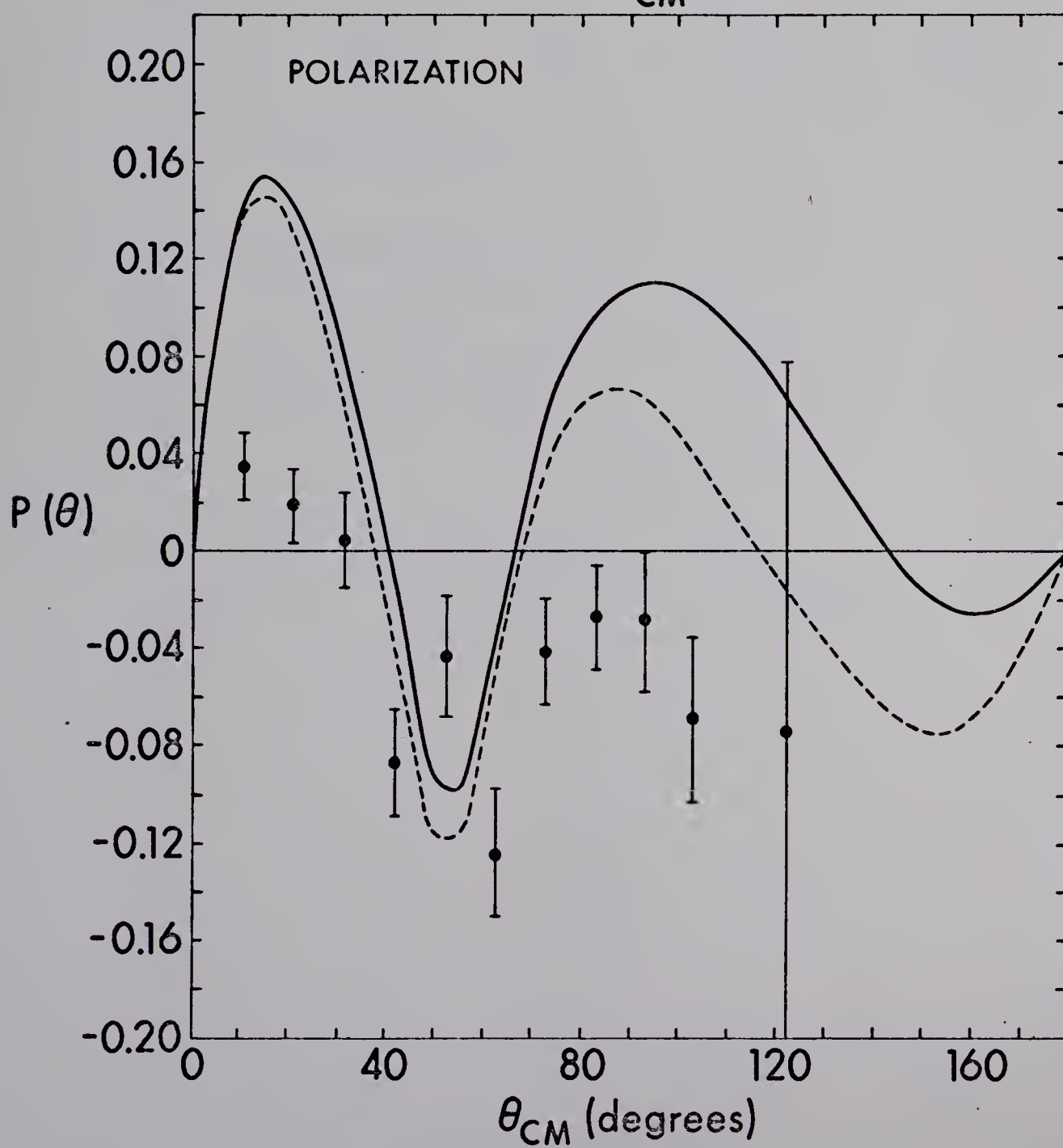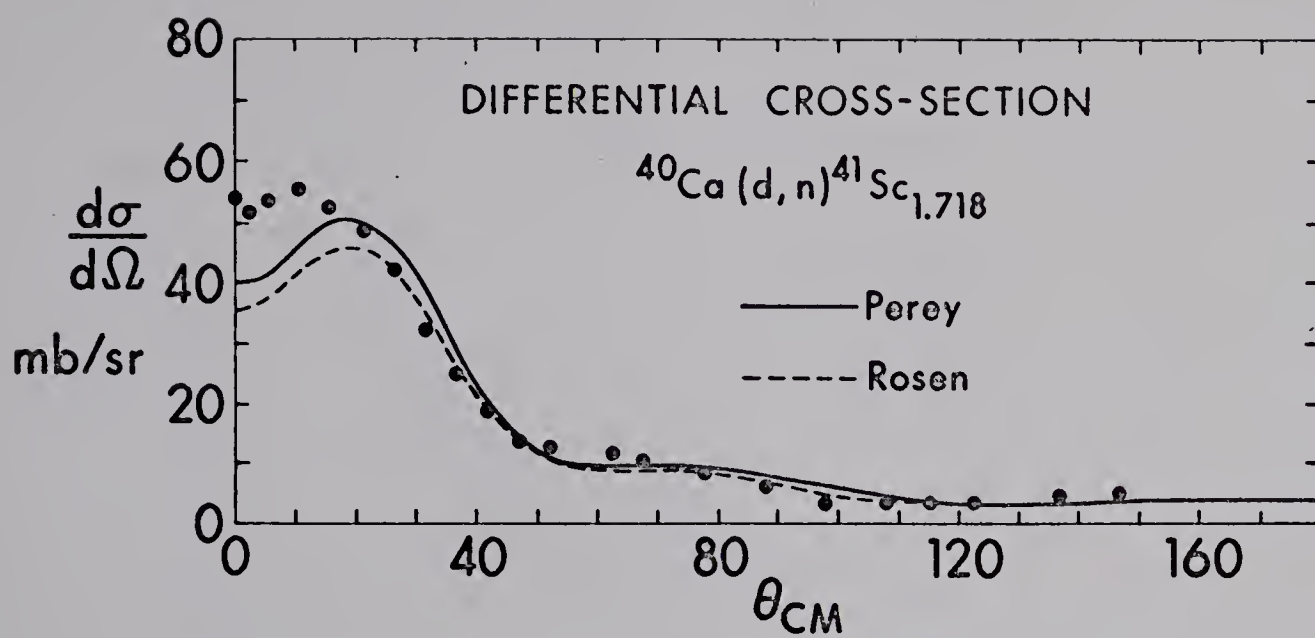
Figure 3.7   Fits to the data of figure 3.5
comparing Perey's and Rosen's neutron para-
meters.   The deuteron spin-orbit potential
is 13 MeV.   The DWBA cross-sections have been
multiplied by 0.257.

DIFFERENTIAL CROSS-SECTION

$^{40}Ca(d,n)^{41}Sc_{2.415}$

—— Perey

- - - Rosen

POLARIZATION

$P(\theta)$

θ_{CM} (degrees)
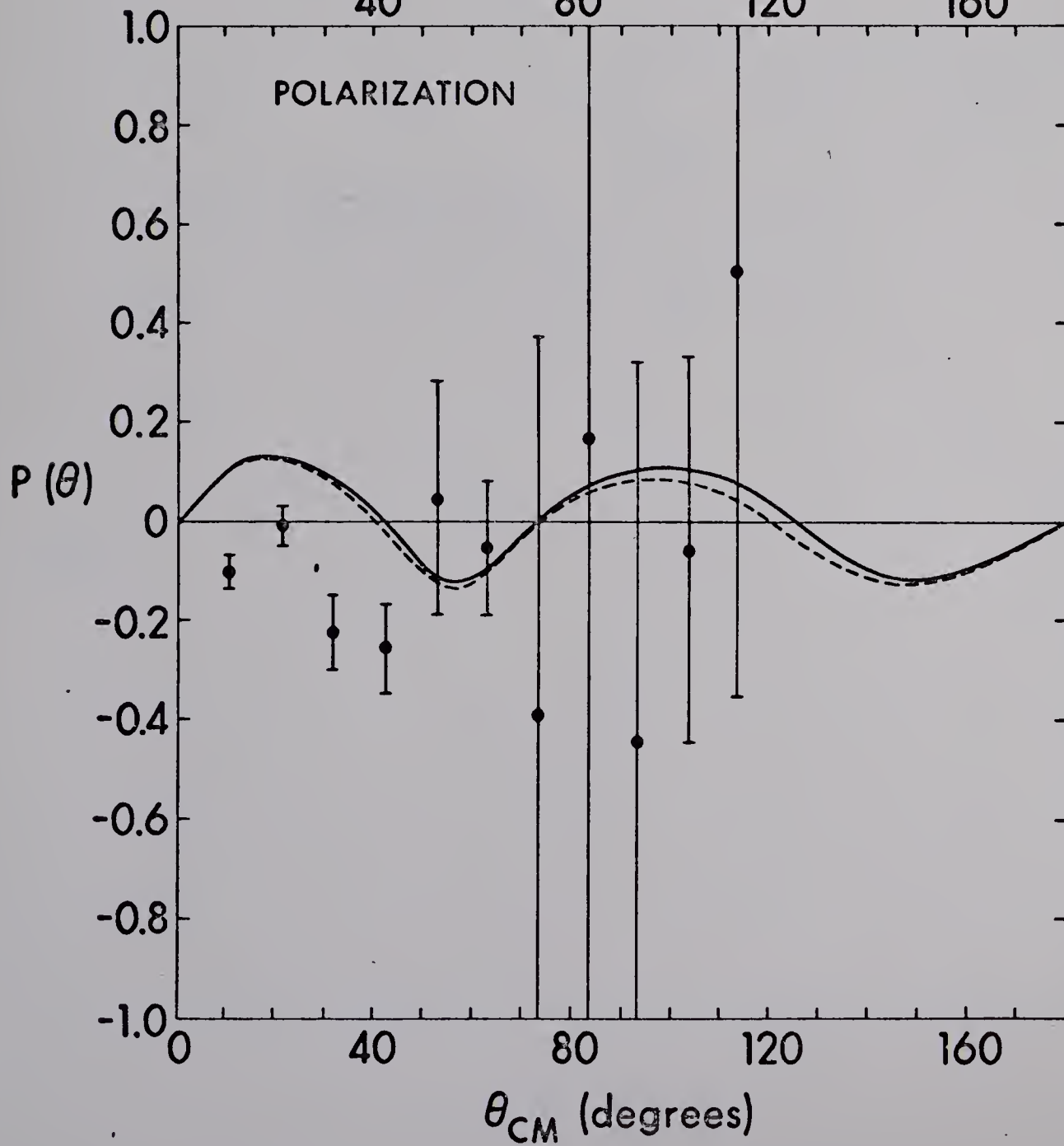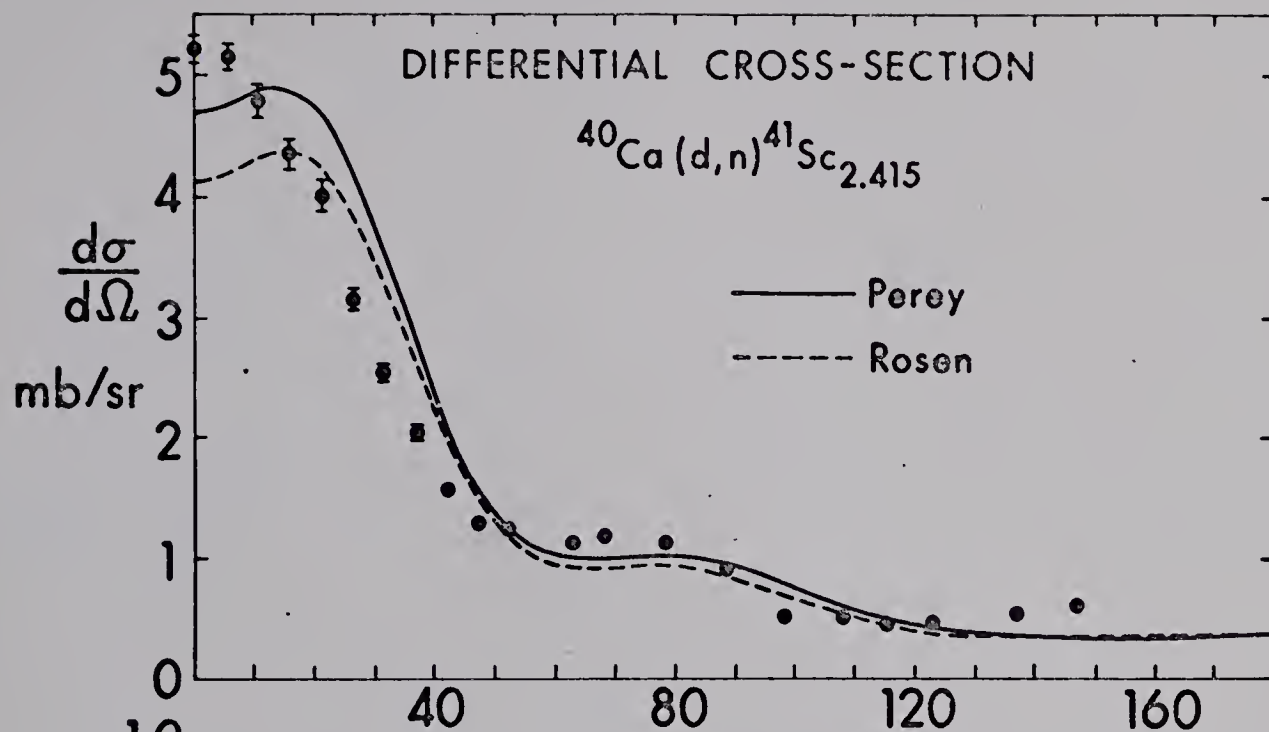
Figure 3.8　The differential cross-section
and neutron polarization for $^{16}O(d,n)^{17}F_{gnd}$
at E_d = 6 MeV. ℓ_p = 2, j = $\ell_p + \frac{1}{2}$ = $J^{\pi} = \frac{5^+}{2}$.

DIFFERENTIAL CROSS-SECTION

$^{16}O(d,n)^{17}F_{gnd}$

POLARIZATION
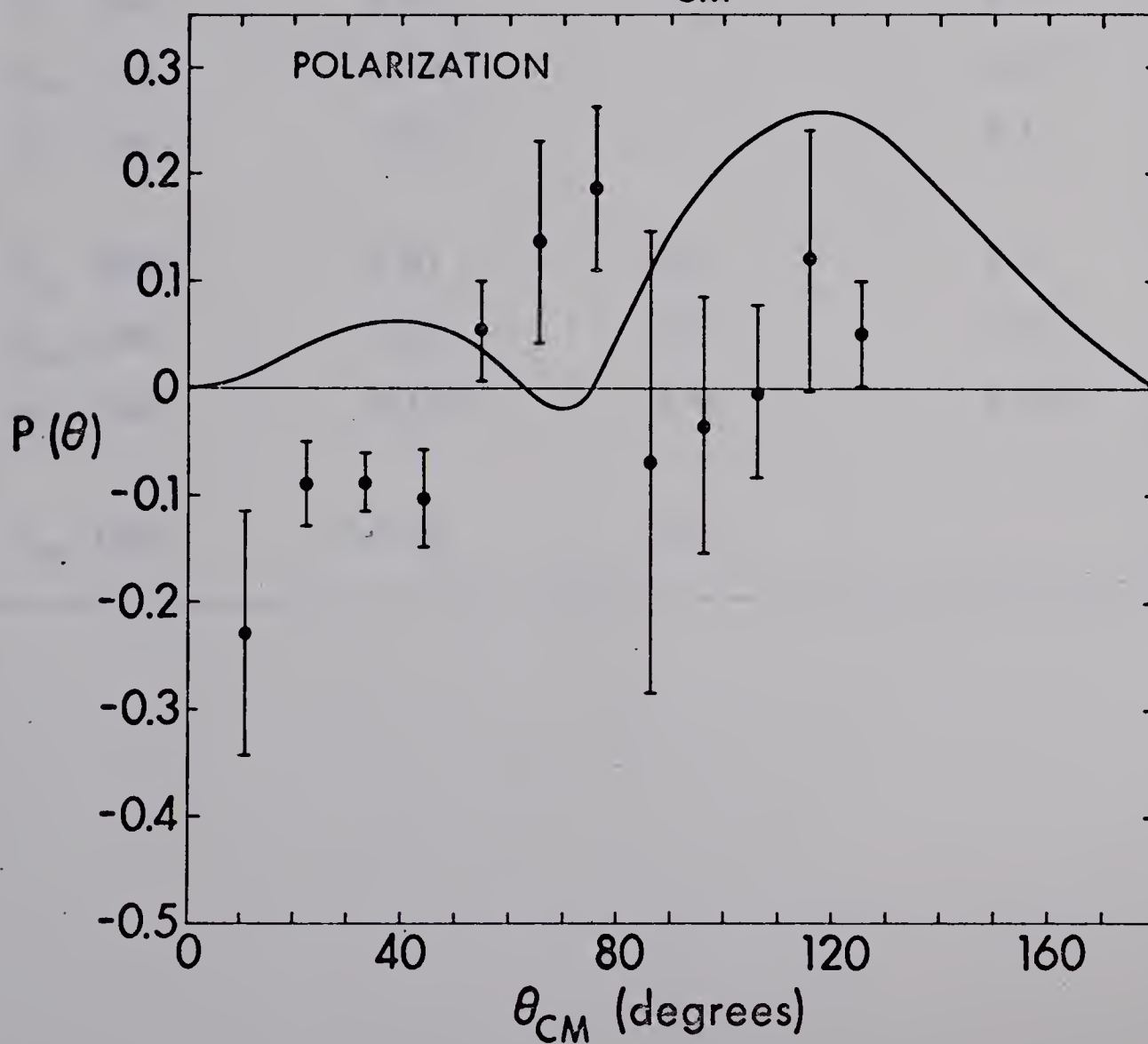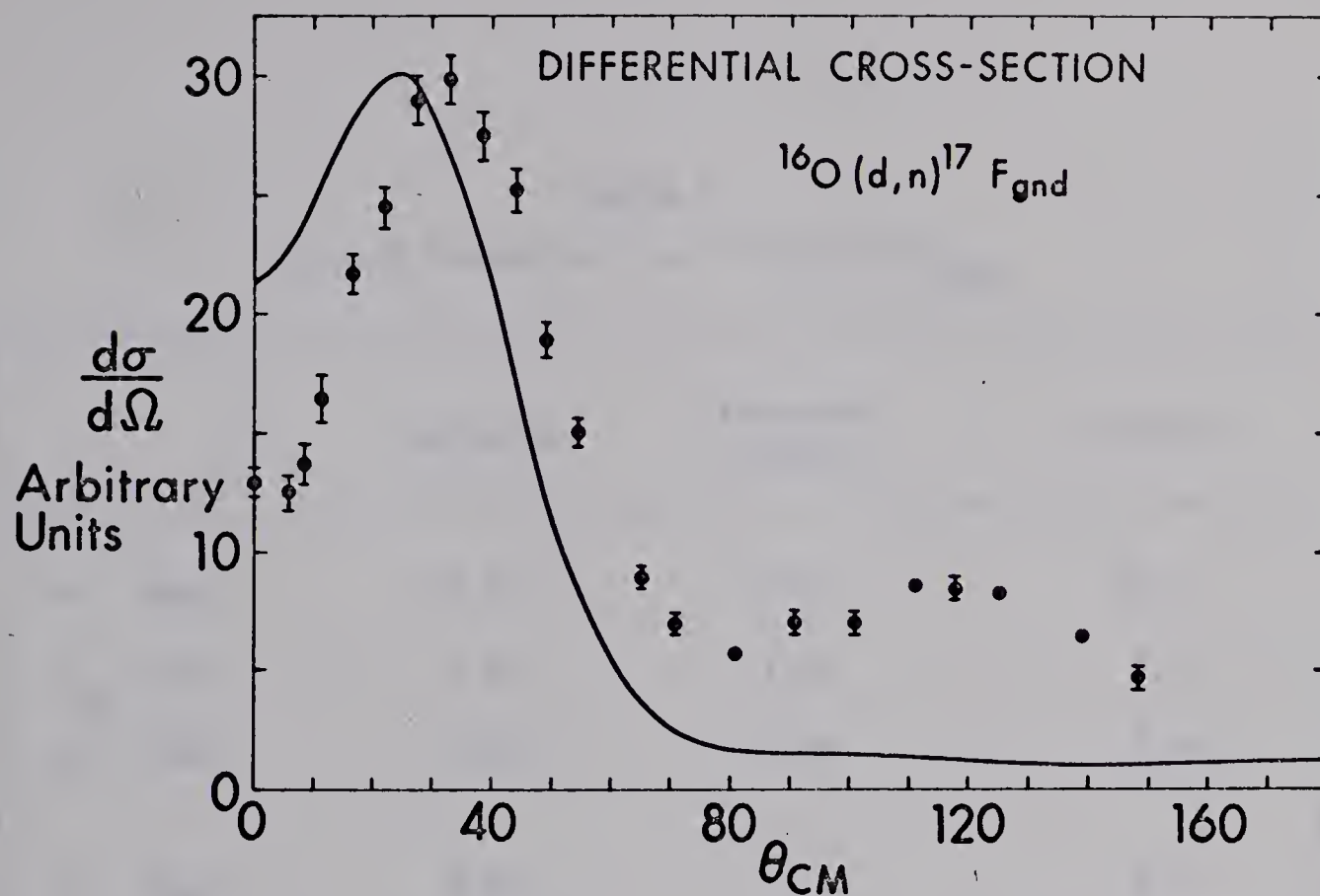
Table X

Optical Potentials for $^{16}O(d,n)^{17}F_{gnd}$

		Deuteron	Captured Proton	Neutron
V	(MeV)	81.76	52.61	46.8
r_{OR}	(fm)	1.25	1.25	1.27
a_R	(fm)	0.617	0.65	0.66
W	(MeV)	8.03		9.6
r_{OI}	(fm)	1.483		1.27
a_I	(fm)	1.435		0.47
V_S	(MeV)	7.67	6.5	7.2
r_{OS}	(fm)	1.25	1.25	1.25
a_S	(fm)	0.617	0.65	0.66
r_{oc}	(fm)	1.25	1.25	

Figure 3.9   The differential cross-section

and neutron polarization for $^{16}O(d,n)^{17}F_{0.5}$

at $E_d = 6$ MeV. $\ell_p = 0$, $j = \ell_p + \frac{1}{2} = J^{\pi} = \frac{1}{2}^+$.

DIFFERENTIAL CROSS-SECTION

$^{16}O(d,n)^{17}F_{0.5}$
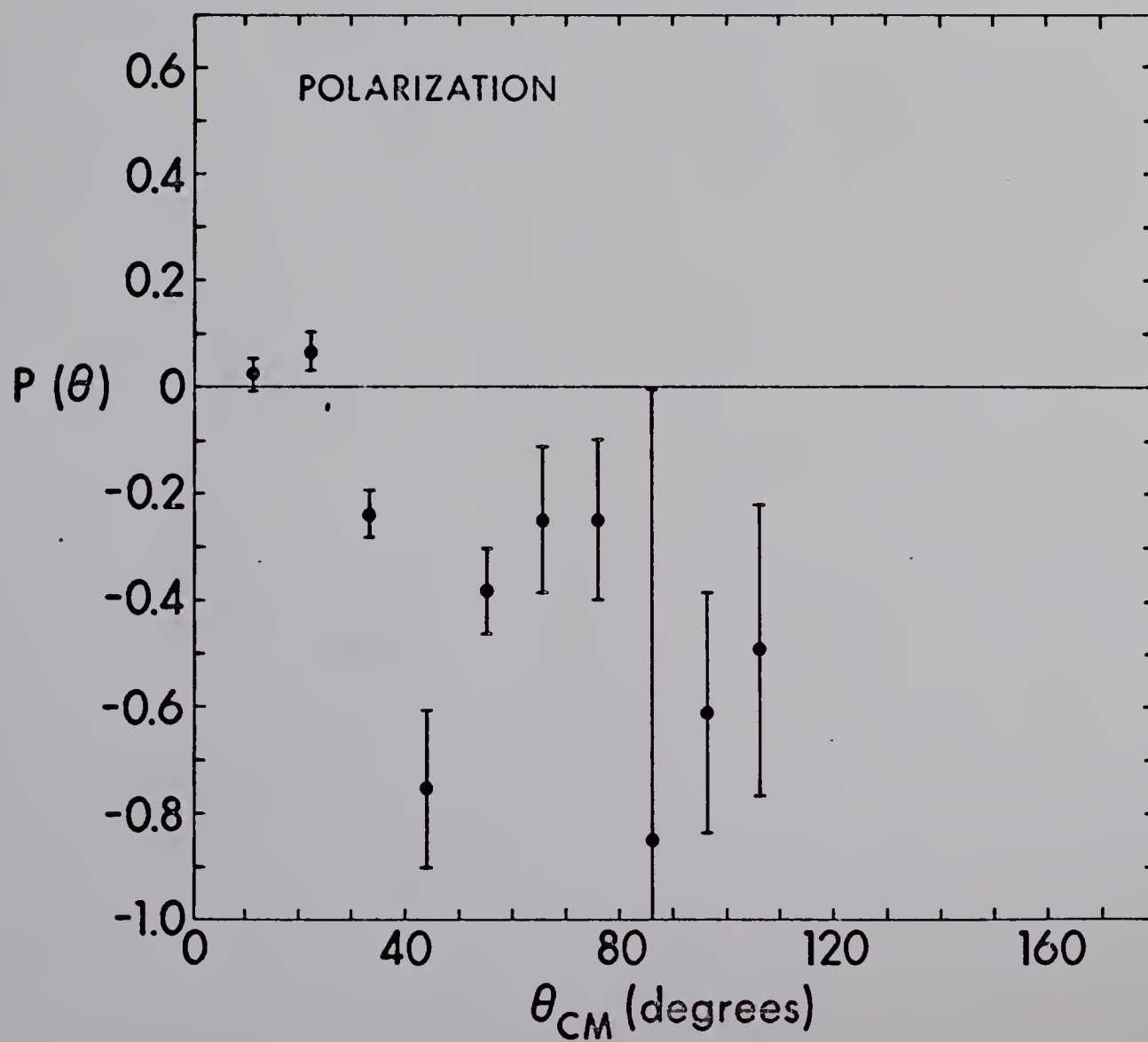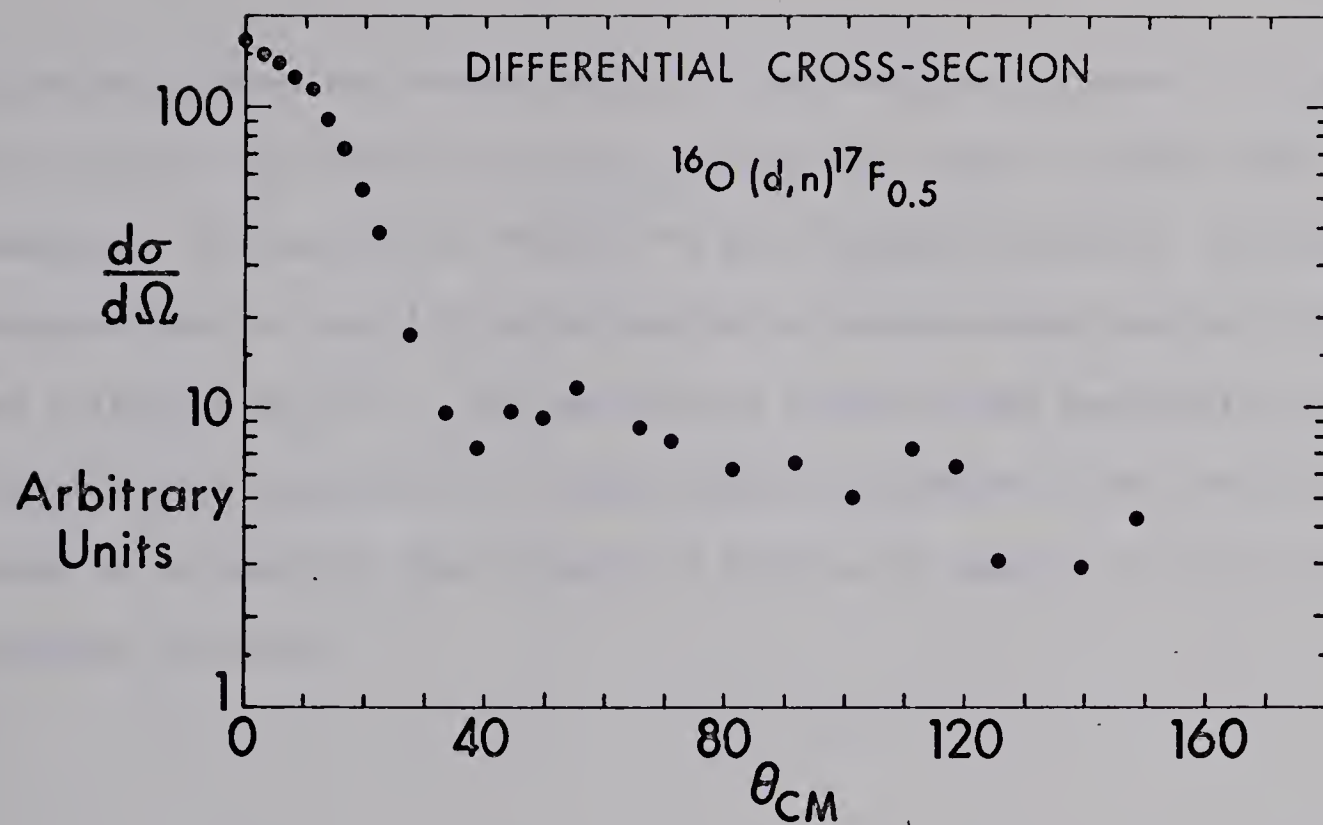
POLARIZATION

polarization data are rather inaccurate and absolute differential cross-sections were not given, no serious attempt was made to analyse this reaction. The results of $^{16}O(d,d)^{16}O$ and $^{16}O(d,p)^{17}O$ work at the higher energies tend to make ^{16}O attractive for a reaction study similar to the one initiated for ^{40}Ca. The determining factor in the desirability of studying the reactions on ^{16}O would likely be whether or not the yield curve is as smooth in the vicinity of 6 MeV as it appears to be at higher energies (Al 67a).

CHAPTER 4

CONCLUSIONS

To some extent, conclusions reached from the analysis of the $^{40}Ca(d,n)^{41}Sc$ are preliminary. When the other aspects of the study of the ^{40}Ca reactions are completed some of the ambiguities arising in the analysis should be removed. Agreement between theory and experiment to date is far from adequate. A few things, however, are already apparent.

In order to clarify the role of the compound nucleus ^{42}Sc in these reactions Hauser-Feshbach calculations are required. Information on the compound nucleus reaction contributions should test the postulate that these effects are responsible for the lack of agreement with DWBA calculations for the ground state of ^{41}Sc.

It is unlikely that the data on the 1.718 and 2.415 MeV states in ^{41}Sc will be helpful in the reaction studies unless an unbound state DWBA code becomes available. The ground state transition, however, favours a deuteron spin-orbit potential of about 13 MeV or slightly higher. While this potential seems high, Perey and Perey have indicated potentials up to 15 MeV are required in some of their studies (Pe 66). However, the potentials they list were derived from differential cross-section fits and may be inaccurate. The fact that they found potentials scattered over the range of 0 to 15 MeV may be indicative of the insensitivity

of the differential cross-section to the spin-orbit potential.

Fits to the (d,p) cross-sections and proton polarization data may make the choice of the deuteron spin-orbit potential more definite. When measurements of vector and tensor polarization in deuteron elastic scattering are made, a more conclusive choice of the spin-orbit potential should be possible. This approach would remove ambiguities introduced by stripping theory and perhaps indicate whether a potential of the $\vec{L} \cdot \vec{\sigma}$ form is adequate.

It appears that extensive systematic studies of deuteron elastic scattering are urgently needed. Until elastic scattering parameters for the entrance channel are well established it will be difficult to make conclusive tests on the stripping reaction itself.

Hopefully, we are now at the stage where some of the simplifying approximations mentioned in Chapter 1 can be relaxed. There is certainly convincing evidence that the d-state must be included in the description of the deuteron (Jo 67). It would also be interesting to study the effect of using more realistic wave functions for the captured particle.

Little work has been done on the $^{40}Ca(d,n)^{41}Sc$ reaction at higher energies. It would be helpful to measure the differential cross-sections and polarizations in the 7 to 12 MeV bombarding energy range in order to compare this reaction with the (d,p) mirror reaction studied by Lee et al (Le 64). Polarization measurements at 5 and 6.5 MeV might also be helpful in the study of the $^{40}Ca(d,n)^{41}Sc$ and $^{40}Ca(d,p)^{41}Ca$ reactions in the lower energy range.

$^{16}O(d,n)^{17}F$ and $^{16}O(d,p)^{17}O$ show some promise as alternative reactions to study with the approach taken in the ^{40}Ca studies.

REFERENCES

Al 67   J. L. Alty, L. L. Green, G. D. Jones, and J. F. Sharpey-Shafer,
         Nucl. Phys. A100 (1967) 191.

Al 67a   J. L. Alty, L. L. Green, R. Huby, G. D. Jones, J. R. Mines, and
         J. F. Sharpey-Shafer, Nucl. Phys. A97 (1967) 541.

Au 63   N. Austern, Fast Neutron Physics II, Editors: J. B. Marion and
         J. L. Fowler, Interscience Publishers (1963) 1113.

Ba 61   R. Batchelor, W. B. Gilboy, J. B. Parker, and J. H. Towle, Nucl.
         Instr. and Meth. 13 (1961) 70.

Ba 64   R. H. Bassel, R. M. Drisko, G. R. Satchler, L. L. Lee, Jr.,
         J. P. Schiffer, and B. Zeidman, Phys. Rev. 136 (1964) B960.

Bo 65   R. Bock, H. H. Duhm, and R. Stock, Phys. Lett. 18 (1965) 61.

Bu 60   B. Buck, R. N. Maddison, and P. E. Hodgson, Phil. Mag. 5 (1960)
         1181.

Bu 61   B. Buck and P. E. Hodgson, Phil. Mag. 6 (1961) 1371.

Bu 65   B. Buck and J. R. Rook, Nucl. Phys. 67 (1965) 504.

Bu 66   S. G. Buccino, D. S. Gemmel, L. L. Lee, Jr., J. P. Schiffer, and
         A. B. Smith, Nucl. Phys. 86 (1966) 353.

Da 66   W. G. Davies, A Study of the Structure of the Nuclei ^{29}P and
         ^{31}P, Ph.D. Thesis, University of Alberta (1966).

Da 66a   W. K. Dawson and J. F. Easton, The University of Alberta General
         Purpose Kicksorter Program (GPKS) for Data Collection with the
         SDS-920 Computer (1966) (unpublished).

En 62   P. M. Endt and C. Van der Leun, Nucl. Phys. 34 (1962) 266.

Fi 66   A. A. Fife, The Excited States of Boron-10, M.Sc. Thesis,
         University of Alberta (1966) 7.

Ge 65   D. A. Gedcke, TMC Kicksorter Memory Routing Unit, Nuclear Research
         Center instruction manual, University of Alberta (1965).

Ge 66a   D. A. Gedcke, <u>Modifications to TMC Two Parameter Unit No. 242:</u>
          <u>On Line Use of the 242 Unit Coincidence Interrupt Input/Output</u>
          <u>with the SDS-920 Computer</u>, Nuclear Research Center instruction
          manual, University of Alberta (1966).

Ge 66b   D. A. Gedcke, <u>Clipped Fast Fanout Instruction Manual</u>, Nuclear
          Research Center, University of Alberta (1966).

Ge 66c   D. A. Gedcke, <u>Use of the TMC Kicksorter Memory Routing Unit</u>
          <u>On-line with the TMC 242 Unit/SDS-920 Interface</u>, Nuclear
          Research Center instruction manual, University of Alberta
          (1966).

Ge 66d   D. A. Gedcke, <u>Instruction Manual for the Triple Coincidence</u>
          <u>Unit</u>, Nuclear Research Center, University of Alberta (1966).

Ge 67a   D. A. Gedcke and W. J. McDonald, <u>A Constant Fraction of Pulse</u>
          <u>Height Trigger for Optimum Time Resolution,</u> Nuclear Research
          Center, University of Alberta (1967) (submitted for publication
          in Nucl. Instr. and Meth.).

Ge 67b   D. A. Gedcke and W. J. McDonald, <u>Design of the Constant Fraction</u>
          <u>of Pulse Height Trigger for Optimum Time Resolution</u>, Nuclear
          Research Center, University of Alberta (1967) (submitted for
          publication in Nucl. Instr. and Meth.).

Ge 67c   W. J. Gerace and A. M. Green, Nucl. Phys. <u>93</u> (1967) 110.

Go 63   H. Goldstein, page 1525 of reference Au 63.

Gr 66   T. B. Grandy and D. A. Gedcke, <u>Tepel's Peak Fitting Program</u>
          <u>Anneliese</u>, Nuclear Research Center internal report, University
          of Alberta (1966).

Gr 67   T. B. Grandy, Ph.D. Thesis, Physics Department, University of
          Alberta (1967)

Gr 67a   T. B. Grandy, W. K. Dawson, W. J. McDonald, and G. C. Neilson,
          Bull. Amer. Phys. Soc., DE6, <u>12</u> (1967) 682.

Gr 67b   T. B. Grandy and J. W. D. Sinclair, <u>Relativistic Kinematics</u>,
          Nuclear Research Center internal report, University of Alberta
          (1967).

Ha 63   W. Haeberli, <u>Fast Neutron Physics II</u>, Chapter V.G., Editors:
          J. B. Marion and J. L. Fowler, Interscience Publishers, New
          York (1963) 1379.

Hj 65   S. A. Hjorth, J. X. Saladin, and G. R. Satchler, Phys. Rev.
          <u>138</u> (1965) B1425.

Ho 66   B. Hoop, Jr. and H. H. Barschall, Nucl. Phys. <u>83</u> (1966) 65.

Hu 61   P. Huber and K. P. Meyer (editors), Proceedings of the International Symposium on Polarization Phenomena of Nucleons (Basel Convention, July 1960). Helvetica Physica Acta, Supplementum VI (1961).

Hu 66   P. Huber and H. Schopper (editors), Proceedings of the 2nd International Symposium on Polarization Phenomena of Nucleons (Karlsruhe, September 1965), Helvetica Physica Acta, Experientia Supplementum 12 (1966).

Hu 67   L. Hutton and G. D. Jones, U.L.D.P. preprint (1967) (see reference Al 67).

Jo 67   R. C. Johnson and F. D. Santos, Phys. Rev. Lett. 19 (1967) 364.

Ka 63   J. R. Kane, R. T. Segel, and A. Suzuki, Rev. Sci. Instr. 34 (1963) 817.

La 67   S. T. Lam, A Liquid Helium Neutron Polarimeter and its Application to the Reaction ^{28}Si(d,n)^{29}P, Ph.D. Thesis, Physics Department, University of Alberta (1967).

Le 64   L. L. Lee, Jr., J. P. Schiffer, B. Zeidman, G. R. Satchler, R. M. Drisko, and R. H. Bassel, Phys. Rev. 136 (1964) B971.

Le 64a L. Lee, Jr., and J. P. Schiffer, Phys. Rev. Letters 12 (1964) 108.

Le 66   F. S. Levin, Phys. Rev. 141 (1966) 858.

Le 67   H. G. Leighton, G. Roy, D. P. Gurd, and T. B. Grandy, Bull. Amer. Phys. Soc. DE5, 12 (1967) 682.

Le 67a H. G. Leighton, private communication (1967).

Le 68   H. G. Leighton, Ph.D. Thesis (to be submitted).

Li 66   J. Libert, Nucl. Instr. and Meth. 41 (1966) 348, 44 (1966) 188, 44 (1966) 199, 46 (1967) 238.

Ma 60   J. B. Marion, 1960 Nuclear Data Tables, Part 3, National Academy of Sciences--National Research Council, U.S. Government Printing Office, Washington 25, D.C. (August 1960) pp 4-5.

Ma 63   T. H. May, R. L. Walter, and H. H. Barschall, Nucl. Phys. 45 (1963) 17.

Mc 67a W. J. McDonald and D. A. Gedcke, Time Resolution Studies on Large Photomultipliers, Nuclear Research Center, University of Alberta (1967) (submitted for publication in Nucl. Instr. and Meth.)

        D. A. Gedcke and W. J. McDonald, Bull. Amer. Phys. Soc., AF10, 12 (1967) 636.

Mc 67b   W. J. McDonald, D. A. Gedcke, G. C. Neilson, and W. K. Dawson,
          <u>Detection System for a Fast Neutron Time-of-Flight Spectrometer</u>
          (1967) (to be submitted to Nucl. Instr. and Meth.)

Me 62   A. Messiah, <u>Quantum Mechanics Vol. II</u>, North Holland Publishing
          Company, Amsterdam (1962) 801.

Mi 66   D. W. Miller, page 410 of reference Hu 66.

Mi 67a   T. G. Miller, Nucl. Instr. and Meth. <u>48</u> (1967) 154.

Mi 67b   T. G. Miller, private communication (1967).

Ob 66   A. Obst, <u>The $^{12}C(d,n)^{13}N$ Reaction at 6 MeV</u>, M.Sc. Thesis, Physics
          Department, University of Alberta (1966) 14.

Pe 62   F. Perey and B. Buck, Nucl. Phys. <u>32</u> (1962) 353.

Pe 63   F. G. Perey, <u>Direct Interactions and Nuclear Reaction Mechanisms</u>,
          (Editors: E. Clementel and G. Villi) Gordon and Breach, New York
          (1963) 125.

Pe 66   C. M. Perey and F. G. Perey, Oak Ridge National Laboratory
          report ORNL-TM-1529 (June 6, 1966) (submitted for publication
          in Physical Review).

Pe 66a   C. A. Pearson and M. Coz, Nucl. Phys., <u>82</u> (1966) 533 and 545.

Pe 67   F. G. Perey, private communication (1967).

Ri 54   Marvin Rich and Richard Madey, <u>Range-Energy Tables</u>, United States
          Atomic Energy Commission, U.C.R.L. - 2301, Radiation Laboratory,
          University of California, Berkeley, California (March 1954).

Ro 65   L. Rosen, Jerome G. Beery, Alfred S. Goldhaber, and Elliot H.
          Auerbach, Annals of Physics, <u>34</u> (1965) 96.

Ro 65a   L. Rosen, <u>Experiments with Polarized Protons and the Neutron-
          Nucleus Potential Derived Therefrom</u>, University of California
          preprint for the Antwerp Conference (1965).

Ro 66   L. Rosen, page 253 of reference Hu 66.

Sa 64   G. R. Satchler, Nucl. Phys. <u>55</u> (1964) 1.

Si 61   J. E. Simmons and R. B. Perkins, Rev. Sci. Instr. <u>32</u> (1961)
          1173.

St 67   G. M. Stinson, S. M. Tang, and J. T. Sample (to be published).

Te 66   J. W. Tepel, Nucl. Instr. and Meth. <u>40</u> (1966) 100.

Wi 63   D. L. Wieber, Nucl. Instr. and Meth. <u>24</u> (1963) 269.

Appendix A

A CONSTANT FRACTION OF PULSE HEIGHT TRIGGER FOR
OPTIMUM TIME RESOLUTION

This appendix is a complete preprint of a paper accepted for publi-
cation as a letter to the editor in Nuclear Instruments and Methods.
The paper was written in co-authorship with Dr. W. J. McDonald, May
1967.

Abstract

A fast discriminator has been designed which triggers at a constant fraction of the input signal amplitude. When operated by the anode current pulse from a photomultiplier tube the discriminator makes it possible to obtain optimum timing over a 100:1 dynamic range. In addition, the walk is within $\pm$ 120 ps for this range.

Abundant data are available on time resolutions for fast scintillator-photomultiplier combinations as a function of the fractional triggering level[1,2,3,4]. The results of these measurements indicate a minimum time resolution is obtained for a fractional triggering level of about 10% of the peak pulse height. It has been suggested that optimum time resolution should be obtainable with a circuit which triggers at a constant fraction of the anode pulse height independent of pulse amplitude[4,5]. A further advantage of such a circuit, is almost complete cancellation of the amplitude effect (walk).

Considerable progress has been made in the development of fast zero-crossing discriminators to eliminate walk. With the clipping stub technique which has generally been used[6,7], it is difficult to achieve reliable triggering over a reasonable dynamic range with a fractional triggering level much less than 50%. The difficulty is due to sensitivity to statistical pulse shape fluctuations and ringing. This is particularly true for scintillators with decay times longer than 2 nsec. In practice the resolution obtained has been worse by a factor $\geq$ 1.6 than the optimum provided by the scintillator-phototube combination[7,8].

A constant fraction of pulse height trigger has been developed using an attenuation-subtraction technique[5]. A block diagram of the prototype circuit is shown in figure 1. The current pulse from the phototube anode is fed to one input of a zero-crossing discriminator

Figure 1. A block diagram of the circuit designed
for testing the constant fraction of pulse height
attenuation-subtraction method. The block elements
are of conventional design[7,8,9].

CONSTANT FRACTION OF PULSE HEIGHT TRIGGER
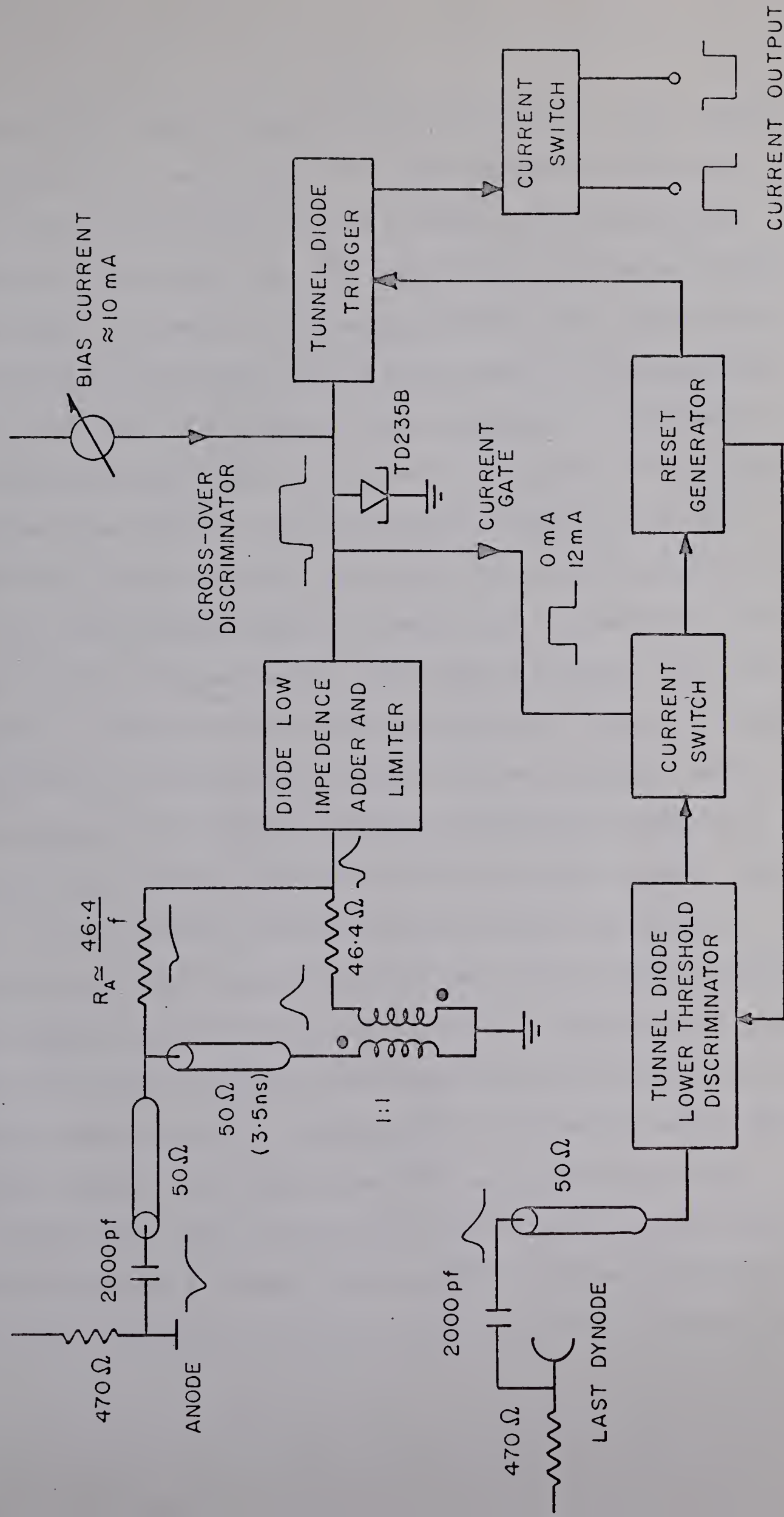
(resistor R_A). This same signal is delayed by about 3.5 nsec, inverted, and presented to a second input. The input impedance of the second input (46.4Ω) in series with the low impedance of the adding point terminates the 50Ω delay line. The resistor R_A is selected so that the peak current it presents to the summing point is equal to the desired fraction of the delayed and inverted current pulse at the appropriate phase point on the leading edge of the inverted pulse. Consequently the resulting current passes through zero at the desired fraction of the anode pulse height. A zero-crossing discriminator similar to conventional designs is used to detect the cross-over phase point.

The zero-crossing element is a tunnel diode supplied with a bias current equal to its peak current. The diode is prevented from triggering by a 12 mA gate current offsetting the bias. The lower threshold discriminator is driven by the last dynode of the phototube. Delays are arranged so that the lower threshold discriminator removes the 12 mA gating current just after the arrival of the attenuated negative anode pulse. As the current at the summing point crosses zero the zero-crossing tunnel diode passes through the peak current biasing condition and triggers rapidly to the high voltage state. Further circuits convert this signal into complementary 20 mA output currents for driving a time to pulse height converter. A reset generator returns all tunnel diodes to their original low voltage states after an appropriate interval.

Tunnel diode charge sensitivity has been reduced by using a diode with low capacitance and high peak current[9]. Overdrive effects[6] are minimized by limiting the switching current applied to the tunnel diode

with a network of fast diodes, as well as following the zero-crossing
element with a high sensitivity, fast tunnel diode trigger[9].

Figure 2 shows resolution curves measured with a constant threshold
discriminator for an RCA 8575 phototube excited by a fast light pulser[4].
The charging line of the pulser was adjusted to produce a pulse at the
photomultiplier anode with a rise time of 2 nsec and a decay constant of
6 nsec to duplicate approximately the response of fast scintillators such
as Naton. The ordinate, f, gives the fraction of the peak anode current
at which the discriminator threshold was set (leading edge timing).
Windows 10% wide were used to restrict the range of the integrated pulse
height. A correction for residual walk[4] across the window width was
also applied. Clearly the optimum time resolution is obtained for a
fraction $f \leq 10\%$. Equivalent electron energies have been indicated on
this and other figures. The 340 keV Compton edge from ^{22}Na 511 keV
annihilation radiation in a Naton plastic scintillator was used for
calibration.

A fraction of 10% was chosen for the constant fraction of pulse
height trigger ($R_A = 215\Omega$). Figure 3 shows a comparison between the
time resolutions obtained with the constant threshold discriminator
and with the constant fraction of pulse height trigger, for f = 10%.
Ten per cent windows were applied to the integrated pulse in both cases.
The resolutions obtained with both techniques are the same within
experimental errors. The solid curve in figure 3 represents the
theoretically expected dependence[10] on equivalent electron energy E,

Figure 2. Time resolution curves for the RCA 8575
photomultiplier excited by a light pulser as taken
with a constant threshold discriminator. The equiv-
alent electron energies have been obtained by cali-
bration with the 340 keV Compton edge for 511 keV
γ rays in a Naton scintillator. f is the fractional
triggering level referred to the peak anode current
specified in the diagram.

RCA 8575 TIME RESOLUTION
LIGHT PULSER
2000 Volts

Figure 3. A comparison between time resolutions
obtained with a fixed threshold discriminator and
the constant fraction of pulse height trigger for
$f = 10\%$. The arrows indicate Compton edge energies
for the γ rays from ^{22}Na source.

TIME RESOLUTION COMPARISON
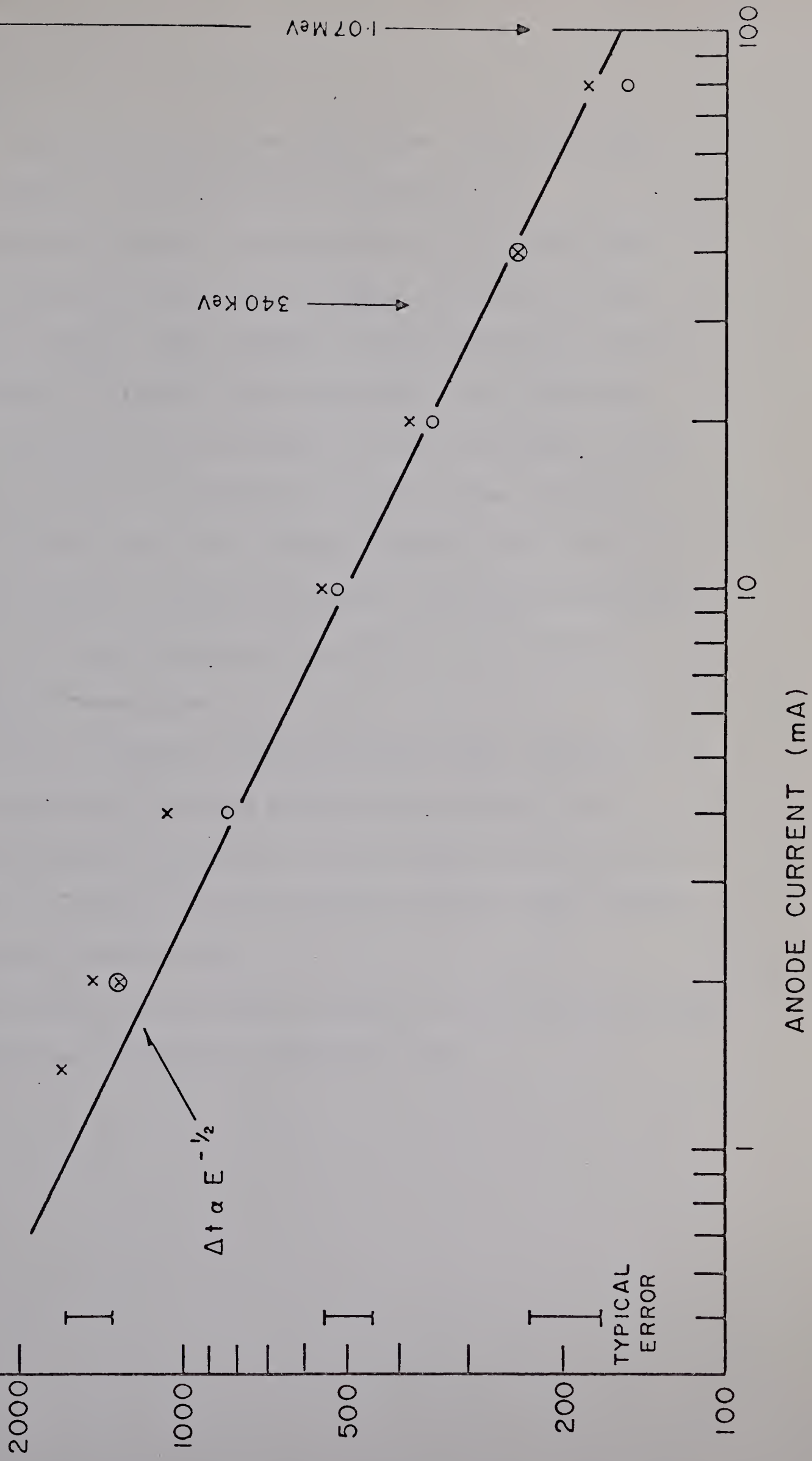RCA 8575, 2000V

LIGHT PULSER

f = 10%

x CONSTANT FRACTION OF PULSE HEIGHT TRIGGER
O CONSTANT THRESHOLD DISCRIMINATOR (LEADING
EDGE)

$\Delta t \, \alpha \, E^{-1/2}$

340 keV →

1·07 MeV →

ANODE CURRENT (mA)

Δt (FWHM)
(ps)

TYPICAL
ERROR

i.e. $\Delta t \propto E^{-\frac{1}{2}}$. Note that the measured resolutions diverge from this curve where the number of photoelectrons is extremely low.

Figure 4 shows the residual walk measured over the useful range of the constant fraction of pulse height trigger. The walk is within ± 120 psec. over a dynamic range of 100:1 (1.2 mA to 120 mA peak anode current). Operation is limited at the high current end by phototube space charge saturation, and at low current by the discriminator itself. In the saturation region the equivalent unsaturated anode current was deduced by monitoring a dynode lower down the bleeder chain. Over the useful operating range the residual walk makes a very small contribution to broadening of the time resolution in comparison to the intrinsic FWHM at the same pulse amplitude.

In conclusion, the constant fraction of pulse height trigger has proved to be successful for deriving optimum time resolution from a fast scintillator-phototube combination for fractional triggering levels from 5% to 30%. The dynamic range and walk cancellation appear adequate for most experimental requirements.

A version of this circuit suitable for general use is being developed and will be described in detail in a subsequent paper.
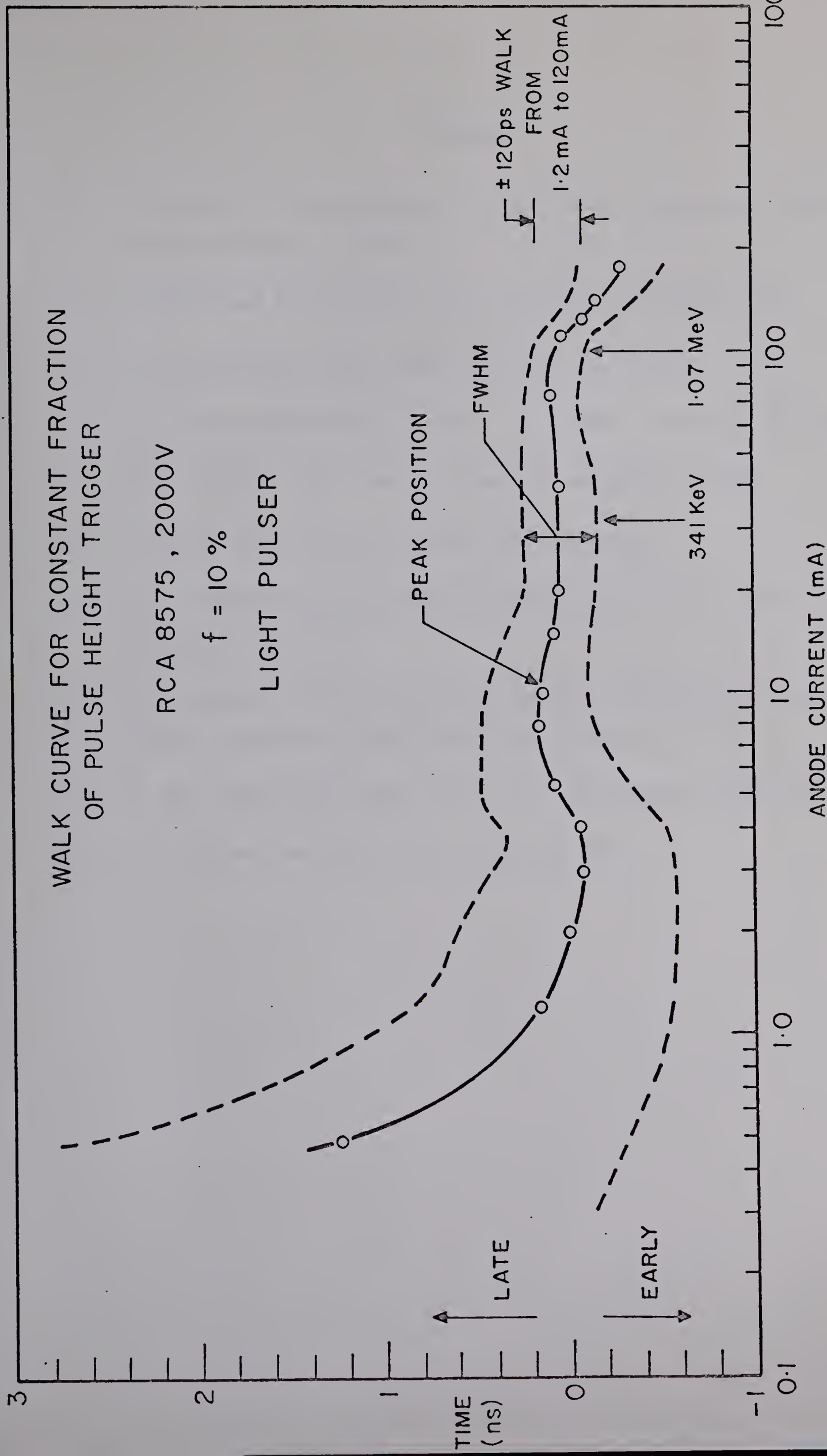
Figure 4. The walk curve measured for the
constant fraction of pulse height trigger
for f = 10%. The arrows indicate Compton
edge energies for the γ rays from a ^{22}Na
source.

WALK CURVE FOR CONSTANT FRACTION
OF PULSE HEIGHT TRIGGER

RCA 8575 , 2000V

f = 10 %

LIGHT PULSER

REFERENCES

1) G. Present, A. Schwarzchild, I. Spirn, and N. Wotherspoon, Nucl. Instr. and Meth. 31 (1964) 71.

2) W. Bartl and P. Weinzierl, Rev. Sci. Instr. 34 (1963) 252.

3) A. Schwarzchild, Nucl. Instr. and Meth. 21 (1963) 1.

4) W. J. McDonald and D. A. Gedcke, Nucl. Instr. and Meth. (in press).

5) D. A. Gedcke, M.Sc. Thesis, University of Ottawa (1964).

6) P. Orman, Nucl. Instr. and Meth. 21 (1963) 121.

7) D. L. Wieber and H. W. Lefevre, IEEE Trans. Nucl. Sci. NS-13, No. 1 (February 1966) 406.

8) C. W. Williams, ORTEC Instruction Manual, 264 Photomultiplier Timing Discriminator and Preamplifier (1967).

9) R. Nutt, IEEE Trans. Nucl. Sci. NS-14, 1 (February 1967) 110.

10) L. G. Hyman, Rev. Sci. Instr. 36 (1965) 193.

Appendix B

DESIGN OF THE CONSTANT FRACTION OF PULSE HEIGHT TRIGGER
FOR OPTIMUM TIME RESOLUTION

This appendix is a complete preprint of a paper submitted for publication in Nuclear Instruments and Methods, August 1967.

DESIGN OF THE CONSTANT FRACTION OF PULSE HEIGHT TRIGGER

FOR OPTIMUM TIME RESOLUTION*

D. A. Gedcke and W. J. McDonald

Abstract   The constant fraction of pulse height trigger has been shown
previously[1,2] to provide the optimum time resolution with a scintillator-
photomultiplier system. The principle is discussed in detail in this
paper and a circuit suitable for general use is presented. Over a
100 : 1 dynamic range the walk is within ± 120 psec. The lower thres-
hold is variable from 0.8 mA to 10 mA on the anode pulse height. A
comparison is made with other commonly used timing methods.

1. Introduction

In previous papers[1,2] results of tests on a constant fraction of pulse
height trigger were presented. It was shown that this technique produces
the optimum time resolution obtainable from a fast scintillator-phototube
combination over a 100 : 1 dynamic range. The residual walk over the same
pulse height range was within ± 120 psec. A circuit design for this trigger
which is suitable for general use is described in this paper.

A brief review of the other commonly used processing methods will be given in order to show how they can limit the obtainable time resolution.

2.   A Comparison of Pulse Processing Methods

Information has been available for some time which indicates that the time resolution of a scintillator-photomultiplier combination exhibits a minimum at a fractional triggering level of about 15% independent of pulse height[1,2,3,4,5,6]. Figure 1 is an example of such data taken from ref. 3. The detector was a 1" diameter x 1" long NE213 scintillator mounted on an XP1040 photomultiplier. The time resolution, Δt, is the full width at half maximum (nsec) of the time peak observed in a time-of-flight experiment with 17 MeV neutrons. The abscissa, f, is the fractional triggering level defined in the following way. The current pulse from the last dynode of the photomultiplier was used to drive a low input imped-ance tunnel diode discriminator. The discriminator was set to trigger at a fixed threshold on the leading edge of the current pulse (straight response[7]. The fractional triggering level is defined as the discriminator threshold divided by the amplitude of the current pulse.

As can be seen from Fig. 1, the time resolution is a minimum for a fractional triggering level of about 10%. The energies indicated in the diagram are equivalent electron energies deposited in the scintillator. The R values are the estimated numbers of photoelectrons emitted from the photo-cathode for each selected pulse height.

Figure 1.   Time resolution, Δt, (FWHM) as a function
of fractional triggering level, f, for a 1" diameter
by 1" long NE213 scintillator on an XP1040 photo-
multiplier.   Taken from reference 3.

XP 1040
1" Dia. X 1" NE 213

Δt (ns)

BIN 9, 352 KEV, R = 36

TYPICAL ERROR

RELATIVE   ABSOLUTE

BIN 18, 686 KEV, R = 72

BIN 28, 1·06 MEV, R = 109

BIN 44, 2·12 MEV, R = 218

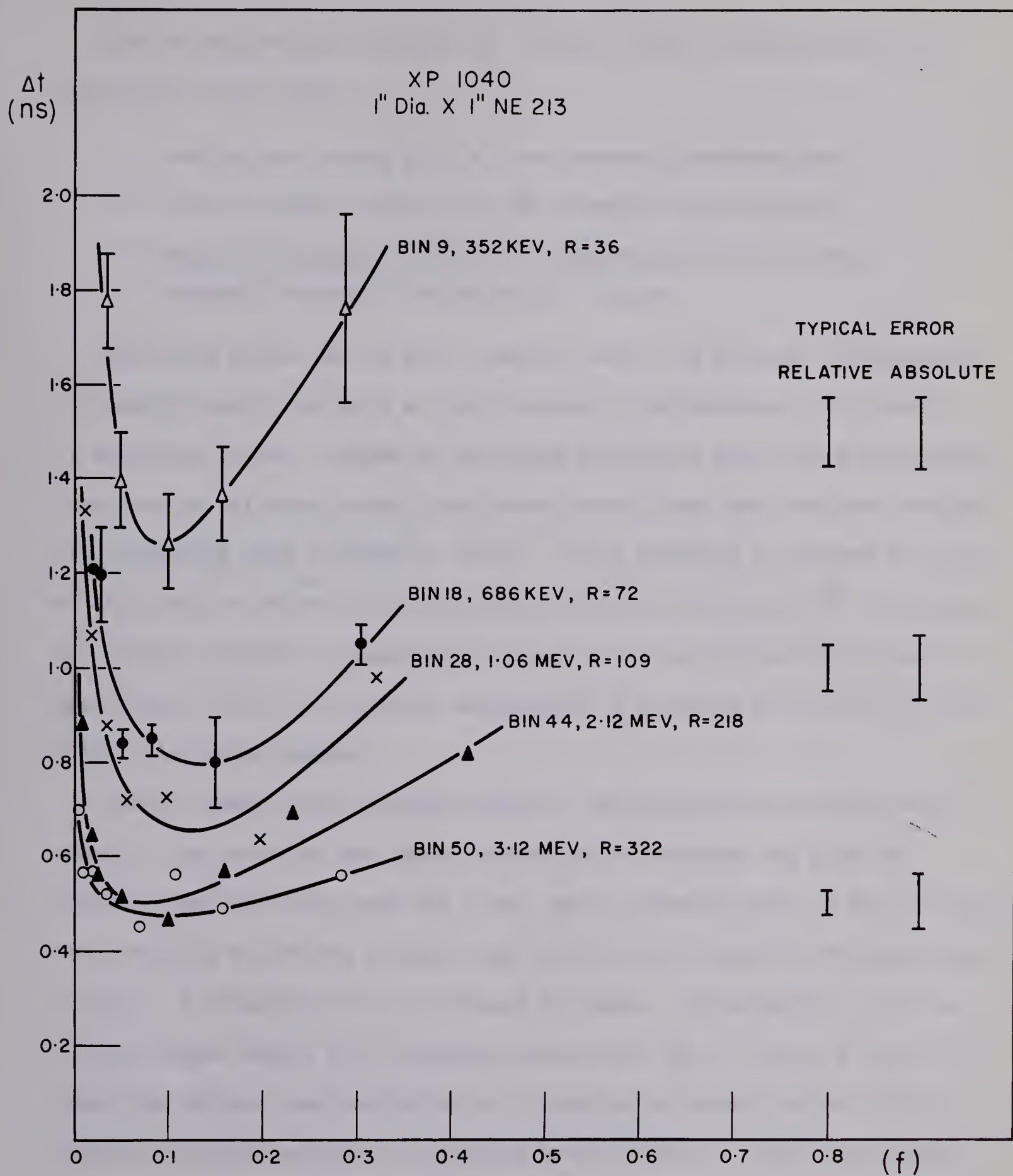BIN 50, 3·12 MEV, R = 322

(f)

Fig. 1

Let us compare three methods for deriving time information from the phototube current pulse.

1. Leading edge timing with a fixed threshold discriminator

2. Fast cross-over timing with the clipping stub technique

3. Timing at the optimum fractional triggering threshold with a constant fraction of pulse height trigger.

The first method is the most commonly used. The greatest disadvantage to leading edge timing with a fixed threshold discriminator is the walk or amplitude effect. Pulses of different amplitudes cross the discriminator threshold at different times (small ones later, large ones earlier) causing the triggering time to shift or "walk." It is possible to correct for most of this walk by either analog or on-line computer technqiues[7,8]. Although the on-line computer two-parameter method is the more effective of the two approaches, difficulty is still encountered in removing all effects of the walk at low pulse heights.

Even if ideal walk correction could be obtained, another problem would remain. The choice of the fixed discriminator threshold can give the optimum time resolution only for a very small dynamic range of pulse heights. For instance, to achieve optimum time resolution for the 352 keV pulse height in Fig. 1 a threshold of 35 keV should be chosen. Unfortunately, for the 3.12 MeV pulse height this threshold will be too low. In Fig. 2, curve (3) shows the optimum time resolution as a function of energy (pulse height) found at the 10% fractional triggering level in Fig. 1. Curve (1a) shows the time resolution that would be obtained with a 35 keV threshold on a fixed

Figure 2. Intrinsic time resolutions obtainable
with the system in Figure 1 for three different
timing methods.

INTRINSIC TIME RESOLUTION

(1a) ▽ THRESHOLD = 35 KeV ⎱ FIXED THRESHOLD
(1b) △ THRESHOLD = 100 KeV ⎰ DISCRIMINATOR
(2) ✕ CLIPPING STUB TYPE FAST ZERO-CROSSING DISCRIMINATOR (f = 50%)
(3) ● CONSTANT FRACTION OF PULSE HEIGHT TRIGGER (f = 10%)

Δt FWHM n SEC

10·0

1·0

0·1

0·1   1·0   10

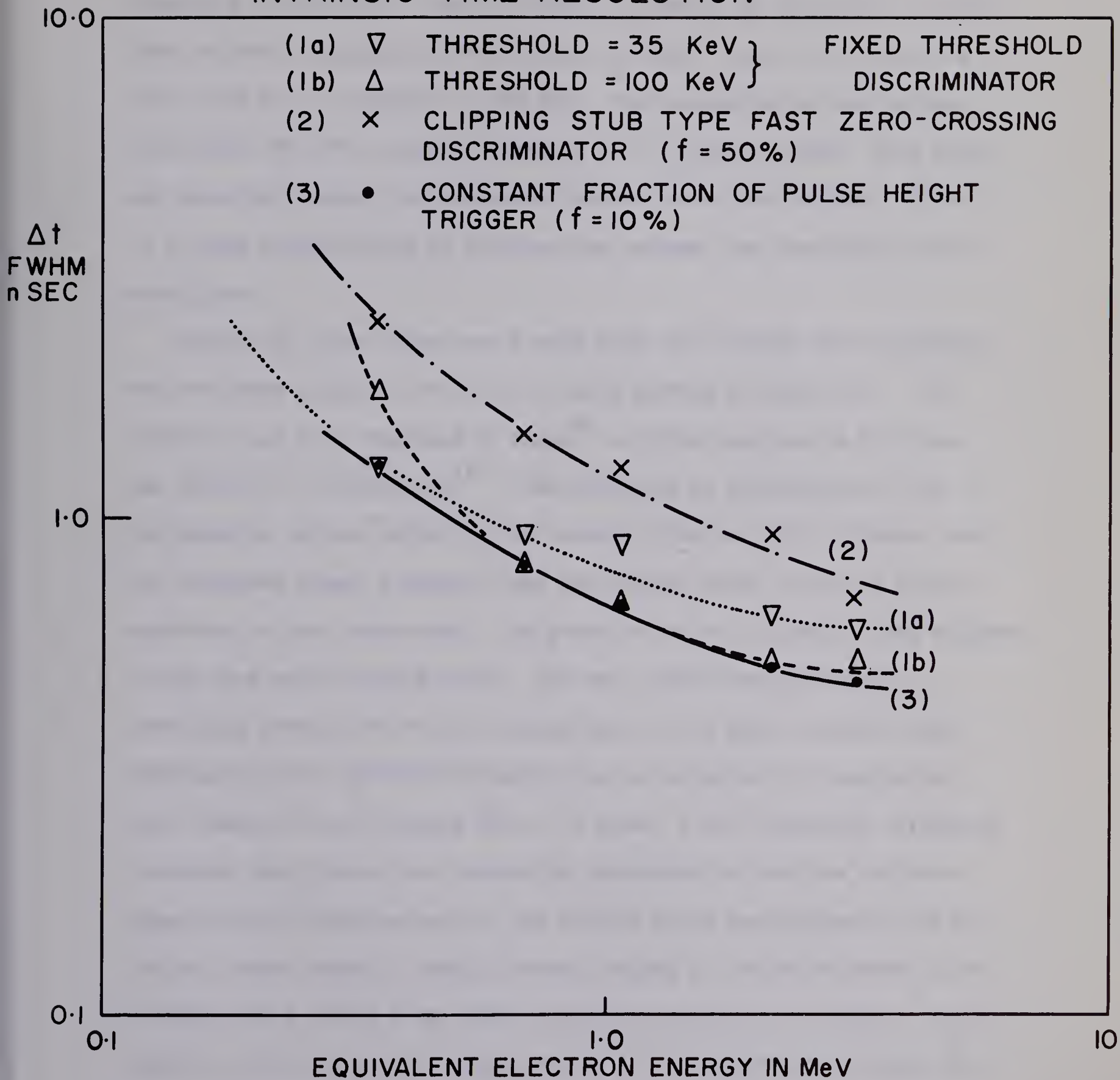EQUIVALENT ELECTRON ENERGY IN MeV

Fig. 2

threshold discriminator (ignoring walk). Clearly the resolution is worse

than optimum at energies different than 352 keV. Curve (1b) shows the

resolution for a threshold of 100 keV. The resolution is near optimum

from about 500 keV to about 2.5 MeV, a 5 to 1 dynamic range. Both below

and above this range the resolution becomes worse than optimum. Clearly,

if a large dynamic range is required, the optimum time resolution must be

sacrificed.

Method (2), fast cross-over timing with the clipping stub technique

was developed mainly to overcome the walk problem of method (1). The

technique was first employed by Orman[9] and then improved on by Wieber

and Lefevre[10] and Williams[11]. The principle is illustrated in Fig. 3.

The negative current pulse from the anode is fed to a 50 Ω clipping stub.

The reflected signal subtracts from the initial pulse to form a bipolar

pulse with a zero cross-over. The pulse is fed to a circuit which triggers

at the true zero-crossing point. The zero cross-over represents a

particular phase point on the leading edge of the anode current pulse.

Consequently this effective threshold can be adjusted by changing the

delay length of the clipping stub. To obtain a 10% fractional triggering

threshold the clipping stub should be lengthened so that the reflected

signal arrives when the tail of the initial pulse has decayed to 10% of

its full pulse height. Usually severe ringing in the pulse shape occurs

in this region making predictable operation virtually impossible. Funda-

mentally, there is another reason why it is not possible to achieve the

optimum resolution at a 10% fractional triggering level with the clipping

Figure 3. A sketch of the clipping stub technique

for the fast zero-crossing timing.

(a)

50 Ω

TRUE
ZERO – CROSSING
DISCRIMINATOR

ANODE

T_d

50 Ω CLIPPING
STUB

$2\,T_d$

UNCLIPPED PULSE
SHAPE

EFFECTIVE THRESHOLD
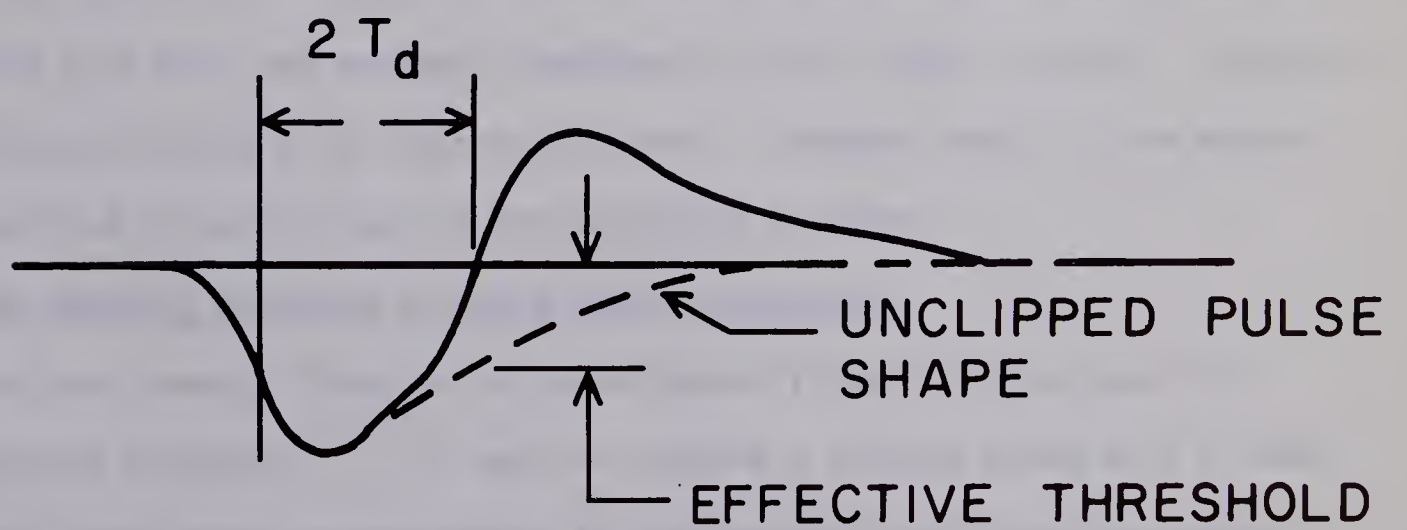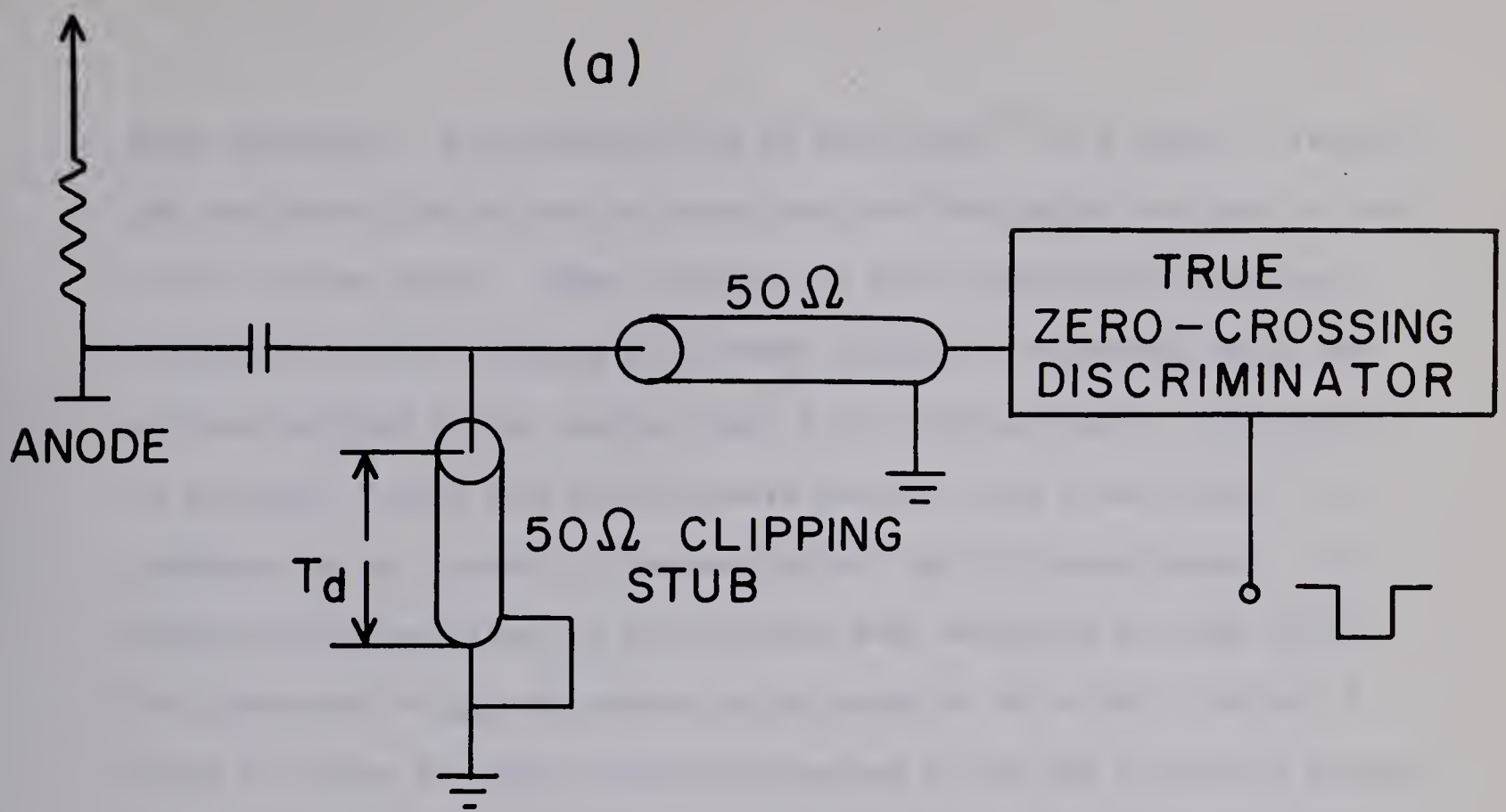
(b) CLIPPED PULSE SHAPE

Fig. 3

stub technique. As Bertolaccini et al have shown[12] the relative statistical amplitude fluctuations are very large for the region far into the tail of the current pulse. These fluctuations will contribute to the time resolution for the clipping stub method causing a broadening beyond the optimum provided by the leading edge of the current pulse. This problem is even more severe with scintillators having a long decay time. The technique is not usable for instance with a NaI(Tl) scintillator. In practice best operation for the clipping stub technique has been found for fractional triggering levels in the range of 50 to 60%. In Fig. 2, curve (2) shows the time resolution provided by the 50% fractional triggering level. Although the time resolution is far from optimum, good walk cancellation is obtained with this circuit. The walk is typically less than ± 100 psec over a 100 : 1 dynamic range[10,11].

The third method has been demonstrated to achieve optimum timing at the 10% fractional triggering level[1,2] and gives the time resolution defined by curve (3) of Fig. 2. Walk cancellation has also been found to be quite good with the constant fraction of pulse height trigger. The walk is typically within ± 120 psec over a 100 : 1 dynamic range. This method is described in more detail in the following sections.

3. The Constant Fraction of Pulse Height Technique

In the constant fraction of pulse height trigger the attenuation-subtraction technique[1,13] is used to produce a bipolar pulse with a zero-crossing phase point corresponding to the desired fractional triggering level on the leading edge of the anode current pulse. Fig. 4 illustrates the principle. Suppose a 20% fractional triggering level is required. The

Figure 4. Waveforms in the constant fraction
of pulse height trigger.

(a) INVERTED AND DELAYED ANODE PULSE

t_3 t_3

$f = 20\%$

V_1

$V_f = 0.2\,V_1$

(b) ATTENUATED ANODE PULSE

$V_2 = 0.2\,V_1$

(c) RESULTING ZERO–CROSSING PULSE

(d) CURRENT GATE

0 mA

−13 mA

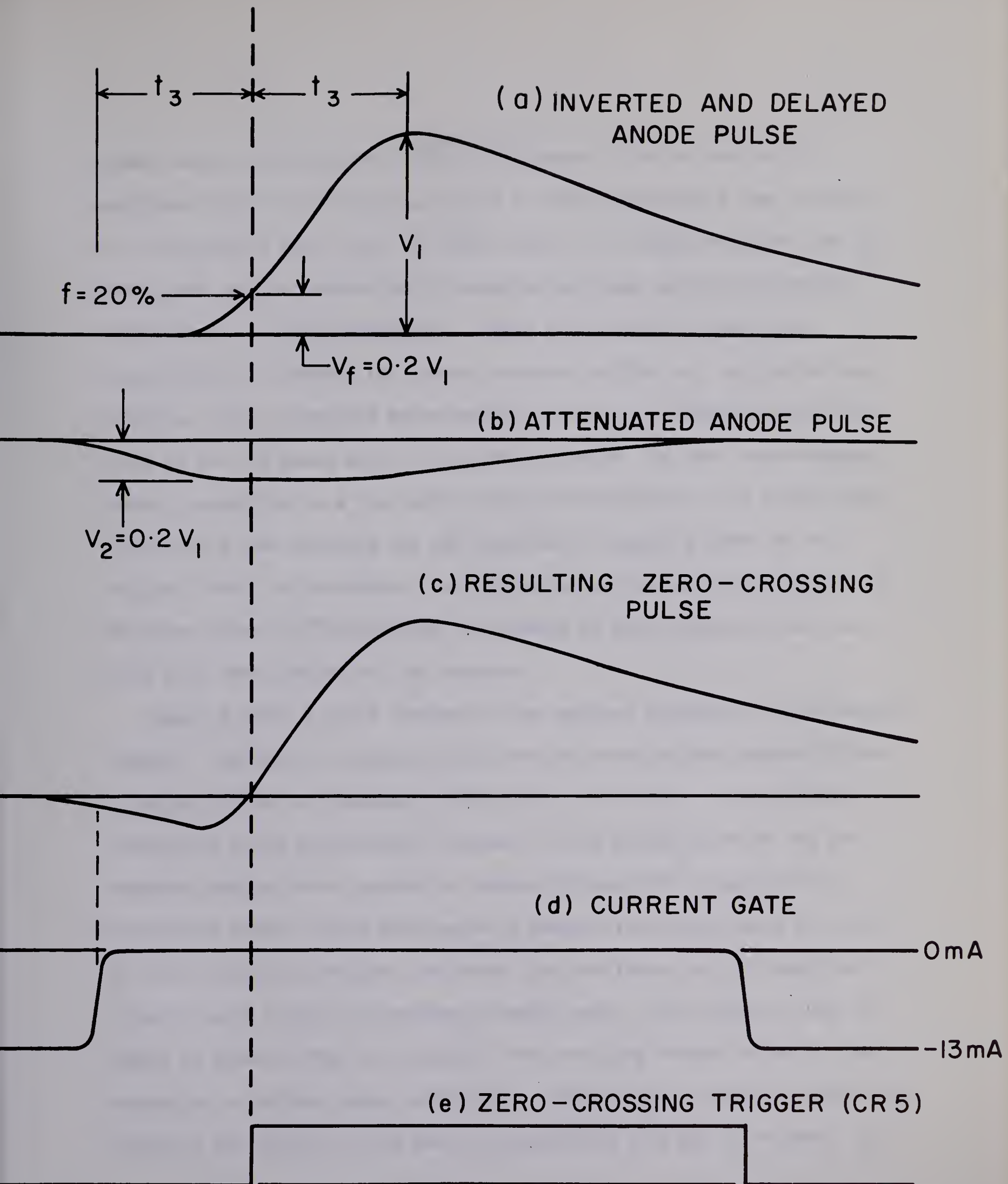(e) ZERO–CROSSING TRIGGER (CR 5)

Fig. 4

prompt anode current pulse is first attenuated to 20% of its initial amplitude (Fig. 4b). The prompt pulse is also delayed by a time interval, t_3, and inverted (Fig. 4a). The delay time t_3 is chosen such that the 20% phase point on the delayed and inverted pulse lines up with the maximum amplitude of the attenuated pulse. These two pulses are then added algebraically to produce the bipolar waveform in Fig. 4c. As can be seen from Fig. 4 the attenuated pulse exactly cancels the delayed and inverted pulse at the 20% phase point on the delayed pulse. If this zero-crossing pulse is presented to a true zero-crossing discriminator, the circuit will trigger at a time defining the 20% fractional triggering level on the original anode current pulse. In an ideal zero-crossing discriminator the 20% phase point will be selected independent of pulse amplitude and complete walk cancellation will be achieved.

Figure 5 shows a block diagram of the constant fraction of pulse height trigger. The negative current pulse from the anode of the photomultiplier is passed through a transmission line, DL1, to the input to transformer T1. Resistor R_A feeds an attenuated version of this prompt pulse to the low impedance adding point provided by diodes CR1 and CR2. Transformer T1 inverts the prompt signal and passes it through the 50 ohm delay DL3. The 46.4 ohm resistor terminates the delay line and feeds the full amplitude current signal to the low impedance summing point. The length of DL3 is chosen as shown in Fig. 4 (t_3 nsec). The resulting current pulse at the summing point is that shown in Fig. 4c. Resistor R_B is chosen to match the impedance encountered at the end of transmission line DL1 to 50 ohms. To

Figure 5. A block diagram of the constant
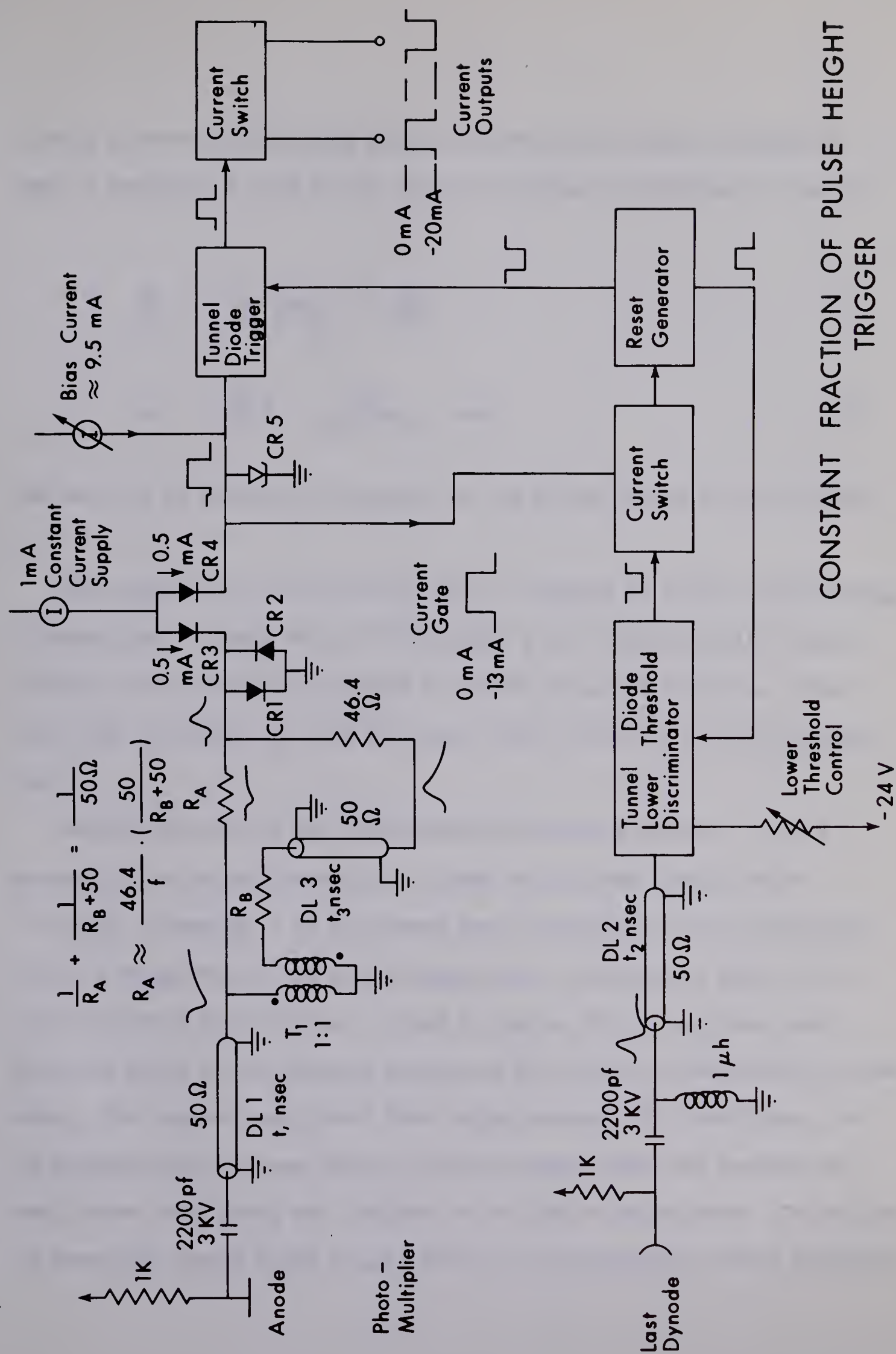fraction of pulse height trigger.

CONSTANT FRACTION OF PULSE HEIGHT TRIGGER

Fig. 5

produce a zero-crossing phase point at a desired fractional triggering level f resistors R_A and R_B are chosen according to equations (1) and (2)

$$\frac{1}{R_A} + \frac{1}{(R_B + 50)} = \frac{1}{50\Omega} \tag{1}$$

$$R_A \approx \frac{46.4}{f} \cdot \frac{50}{R_B + 50} \quad \text{ohms} \tag{2}$$

The accuracy of equation (2) depends on the proper choice of delay length t_3.

The remainder of the circuit in Fig. 5 consists of a true zero-crossing discriminator. Diodes CR3 and CR4 provide a fast current limiter stage, limiting the current pulse applied to tunnel diode CR5 to 0.5 mA. This stage also decouples CR5 from the input when it fires to its high voltage state.

Tunnel diode CR5 is the zero-crossover detecting element. In the absence of the current gate CR5 is biased to its peak current point ($\approx$ 10 mA). Normally, a 13 mA current gate overrides the bias preventing CR5 from triggering to the high voltage state. As shown in Fig. 4, the lower threshold discriminator is used to remove the current gate just after the start of the negative portion of the bipolar zero-crossing current pulse. The negative portion of this pulse prevents CR5 from firing. As the bipolar pulse crosses through zero the tunnel diode CR5 reaches the peak current bias point and triggers to the high voltage state. The following sensitive tunnel diode trigger fires at the beginning of this transition

and drives the current switch output stage. A complementary pair of current outputs is provided for driving a time-to-pulse height converter.

The current output of the last dynode is clipped with a 1 μh inductance to limit the length of the positive phase of the pulse to about 25 nsec. This signal is passed through a transmission line, DL2, and used to trigger the lower threshold discriminator. The lower threshold is variable from about 0.4 mA to 10 mA equivalent anode pulse height. The output of the lower threshold discriminator triggers a current switch which removes the gating current from CR5 and activates the reset generator. The reset generator resets all tunnel diodes 25 nsec after the lower threshold discriminator is fired, and releases them for triggering again after an additional 25 nsec dead time. The difference in delay lengths $t_1 - t_2$ is chosen so that the current gate is removed about 0.5 to 1.0 nsec after the start of the negative portion of the bipolar pulse (Fig. 4(c) and (d)). This length may vary for different phototubes.

4. Circuit for the Constant Fraction of Pulse Height Trigger

Figure 6 shows the detailed circuit for the constant fraction of pulse height trigger. The anode pulse shaping circuit differs slightly from that shown in Fig. 5 in that a monitor output has been added. This output permits observation of the bipolar pulse (Fig. 4c), and is useful for the purpose of walk adjustment[10,11,14]. With the addition of the monitor output, equations (1) and (2) must be modified to

$$\frac{1}{R_A} + \frac{1}{R_B + 50} + \frac{1}{R_C} = \frac{1}{50} \tag{3}$$

Figure 6. Circuit diagram for the constant
fraction of pulse height trigger.

CONSTANT FRACTION OF PULSE HEIGHT TRIGGER
D.A.G.   21/5/67

Fig. 6

$$R_A \simeq \frac{42}{f} \cdot \frac{50}{R_B + 50} \text{ ohms} \tag{4}$$

$$R_C = 10 \ R_A \tag{5}$$

Transformer T1 is a fast 50 Ω inverting pulse transformer manufactured by EH Research Laboratories Inc.[†] The case was removed so that the transformer could be mounted on the printed circuit board. Typical values are shown for R_A, R_B, R_C, and t_3. These values should be chosen, however, for the particular phototube type and scintillator.

The low impedance adder and limiter consisting of diodes CR1, CR2, CR3, and CR4 serves to limit the voltage developed at the junction of R5, CR1 and CR2, as well as limiting the current switched into the tunnel diode to 0.5 mA. For very small currents from R5 or R_A diodes CR1 and CR2 have a sufficiently high input impedance compared to CR3 to allow virtually all the current to switch through CR3 and CR4 into the tunnel diode CR5. As the input current increases the impedance of CR1 or CR2 quickly decreases shunting all the current to ground. Except for very small input signals CR1 and CR2 short the summing junction for R_A and R5 to ground to provide termination for DL3. The fact that over a range of $\pm$ 0.5 mA input current all the current is driven into the tunnel diode gives this input stage high sensitivity. A version of an alternate input stage which provides about a factor of 6 less sensitivity was also tried[11,14]. The lack of sensitivity was found to reduce seriously the dynamic range for good walk cancellation at the low pulse height end of the range. Higher sensitivity

[†]EH Research Laboratories, Inc., 163 Adeline St., Oakland California, U.S.A. Transformer type ZT 5-5X.

is required for the constant fraction of pulse height trigger because the bipolar pulse driving the zero cross-over discriminator has a factor of approximately 5 less undershoot preceding the zero-crossing point than is encountered in the clipping stub technique. The 1.4 mA flowing through R6 into R5 ensures matching of the quiescent voltage at CR1 and CR2 to the peak voltage of tunnel diode CR5.

Transistor Q1 provides the adjustable constant current supply for biasing the cross-over tunnel diode CR5. This type of supply was used to minimize the effect of changing power supply voltages on the zero-crossing walk adjustment. Diode CR6 is a 6V zener diode. CR7 compensates for the temperature variation of the base-emitter voltage of Q1. CR8 provides a first order compensation for the temperature variation of the tunnel diode peak current bias point. Resistor R12 is used to adjust the cross-over bias for minimum walk.

An attenuation-subtraction processing was also used on the input to the lower threshold discriminator because it was found to reduce the walk in the lower threshold triggering time by about a factor of two. This improvement is due to the sharper slope provided near the axis at the cross-over point. The shaping circuit is similar to that used for the anode except that no diode adder and limiter stage is used. Tunnel diode CR12 provides the lower threshold discrimination. The threshold is adjusted by R21. Resistor R20 is used to trim the bias so that CR12 does not free run when R21 is at a minimum.

The gating and reset circuits function as follows. Transistor Q2 normally conducts 13 mA to provide the current gate on CR5. When CR12 triggers to the high voltage state the negative pulse turns Q2 off switching the current into Q3. After a 25 nsec delay the current from Q3 turns on Q5 which in turn resets CR12. At the same time a 10 mA current is switched into Q6 to reset CR10. The resetting of CR12 returns the gating current to reset CR5.

The triggering of the cross-over tunnel diode, CR5, and the function of the current gate have already been described. Tunnel diode CR10 is a high sensitivity discriminator set to trigger as low as possible on the pulse from CR5. Diode CR9 decouples the two tunnel diodes once CR9 has fired. While this trigger was found necessary when slower diodes were used in place of CR5 it is probably not essential in the present circuit. Removal of this trigger would permit coupling CR5 directly to R35 and removal of Q6, R33 and R34. Also the collector of Q4 should be connected directly to ground.

Transistors Q7, Q8, Q9, and Q10 form a set of current switches. Two current outputs are provided. The negative output is quiescently at 0 mA and switches to -20mA during the output pulse. The positive pulse switches from -20mA to 0mA for the duration of the pulse. Catching diodes prevent Q9 and Q10 from saturating when the outputs are not loaded. Both outputs are capable of driving 50 ohm cables with a rise time of about 2 nsec. The pulse duration is approximately 20 nsec.

5.   Walk Adjustment

A novel technique for walk adjustment has been outlined by other workers[10,11]. The monitor output is observed on a fast oscilloscope (preferably a sampling oscilloscope for fine adjustment) while triggering the oscilloscope with the output of the constant fraction of pulse height trigger. The walk adjustment is trimmed until all pulses are observed to cross the zero pulse height axis at the same time. A finer adjustment can be made by performing a two parameter measurement of time vs. pulse height. This is often possible in neutrom time-of-flight experiments[8].

6.   Performance

The performance of this circuit was found to be identical to that of the prototype circuit previously reported[1,2]. Figure 7 shows a typical walk curve. This curve was measured with a light pulser exciting the photocathode of an RCA 8575 photomultiplier. Note that the walk is within $\pm$ 120 psec over a 100 : 1 dynamic range. Operation is limited at the high current end by phototube space charge saturation, and at low current by the discriminator sensitivity.

The circuit has been in operation at this laboratory for some time in neutrom time-of-flight experiments. It has proven to be highly successful in providing optimum time resolution over a wide dynamic range as well as giving very symmetrical peak shapes in the time-of-flight spectrum. To date all the tests have been made with fast scintillators such as Naton, NE213, and NE218, or with a fast light pulser. It would be interesting to check the

Figure 7. The walk curve measured for the constant
fraction of pulse height trigger for f = 10%. The
arrows indicate Compton edge energies for the γ rays
from a ^{22}Na source detected in a Naton scintillator.
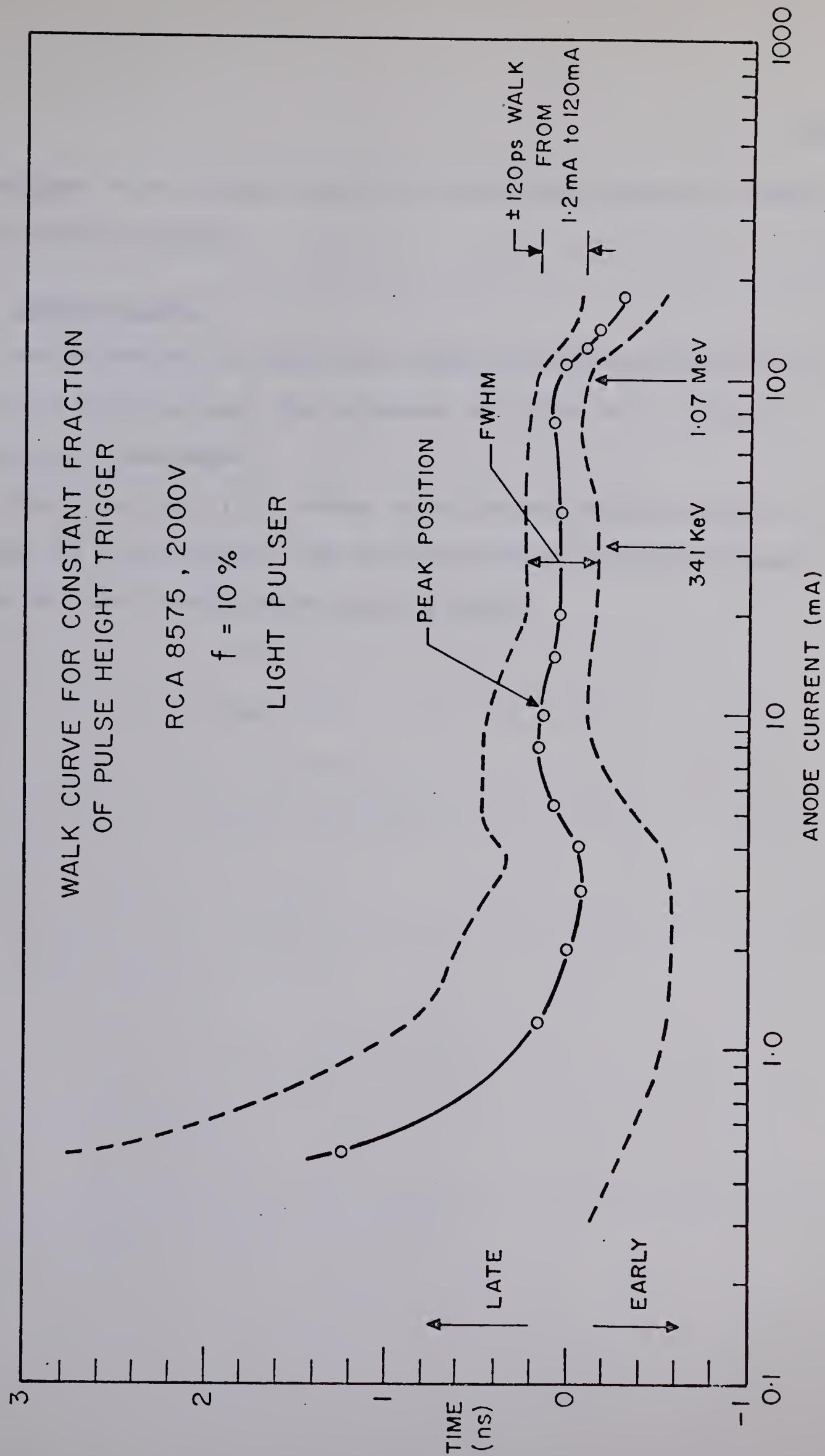From reference 1.

Fig. 7

usefulness of the constant fraction of pulse height trigger for timing with NaI(Tl) detectors.

7. Acknowledgements

The authors wish to thank Mr. R. Popik for the construction of the circuits described here. The assistance of L. Holm and J. Elliott is gratefully acknowledged.

One of us (D.A.G.) is indebted to the National Research Council of Canada for a Studentship. This work was supported in part by a grant from the Atomic Energy Control Board of Canada.

References

1) D. A. Gedcke and W. J. McDonald, A Constant Fraction of Pulse Height Trigger for Optimum Time Resolution, Nucl. Instr. and Meth. (in press).

2) D. A. Gedcke and W. J. McDonald, Bull. Amer. Phys. Soc., AF10, Vol. 12, No. 5 (1967) 636.

3) W. J. McDonald and D. A. Gedcke, Time Resolution Studies on Large Photomultipliers, Nucl. Instr. and Meth. (in press).

4) G. Present, A. Schwarzchild, I. Spirn and N. Wotherspoon, Nucl. Instr. and Meth. 31 (1964) 71.

5) W. Bartl and P. Weinzierl, Rev. Sci. Instr. 34 (1963) 252.

6) A. Schwarzchild, Nucl. Instr. and Meth. 21 (1963) 1.

7) R. E. Bell and M. H. Jørgensen, Can. J. Phys. 38 (1960) 652;
R. E. Bell, in Alpha-, Beta- and Gamma-Ray Spectroscopy (ed. K. Siegbahn, North Holland Publ. Co., Amsterdam, 1965) Ch. 17, 925.

8) G. C. Neilson, W. J. McDonald, D. A. Gedcke, and W. K. Dawson, Detection System for a Fast Neutron Time-of-Flight Spectrometer (to be submitted to Nucl. Instr. and Meth.)

9) P. Orman, Nucl. Instr. and Meth. 21 (1963) 121.

10) D. L. Wieber and H. W. Lefevre, IEEE Trans. Nucl. Sci. NS-13, No. 1 (February 1966) 406.

11) C. W. Williams, ORTEC Instruction Manual, 264 Photomultiplier Timing Discriminator and Preamplifier (1967).

12) M. Bertolaccini, C. Bussolati, S. Cova, S. Donati, and V. Svelto, Nucl. Instr. and Meth. 51 (1967) 325.

13) D. A. Gedcke, M.Sc. Thesis, University of Ottawa (1964).

14) D. A. Gedcke and W. J. McDonald, A Fast Zero-crossing Discriminator for Time Pickoff with Pulsed Beams, Nucl. Instr. and Meth. (in press).

Appendix C

A FAST ZERO-CROSSING DISCRIMINATOR FOR TIME
PICKOFF WITH PULSED BEAMS

This appendix is a complete preprint of a paper accepted for pub-
lication as a letter to the editor in Nuclear Instruments and Methods.
The paper was written in co-authorship with Dr. W. J. McDonald, July
1967.

                              Abstract

        A fast zero-crossing discriminator has been designed for use

as a pulsed-beam time pickoff in time-of-flight experiments. Use

of the zero-crossing technique minimizes the effect of fluctuating

beam conditions on the time information. The walk was measured to

be within ±65 psec from 100mV to 3.5 volts input pulse height. The

threshold is variable from 100mV to 500mV. Observed jitter in the

pulsed beam timing is ≤40 psec. Operation is independent of pulse

shape making this discriminator useful for other applications.

In time-of-flight experiments with pulsed beam accelerators the beam pulse arrival is commonly used to provide the zero time information. A cylindrical capacitor is placed a short distance ahead of the accelerator target. As the beam pulse passes through the cylinder, a current is induced in the wire connected to the capacitor. This current is amplified and applied to a fast discriminator to define the beam pulse arrival time at the target.

If a conventional fixed threshold discriminator is used to detect the beam pulse, fluctuations in the pulse height cause shifts in the time spectrum (walk effect). These short term fluctuations are difficult to avoid in a pulsed beam system. For long experiments, long term drifts in the beam conditions can also produce a time shift. These shifts cause resolution broadening and make time calibrations less reliable over the duration of an experiment.

In order to avoid these problems, a fast discriminator has been designed to trigger at the zero cross-over point on the bipolar current pulse from the time pickoff capacitor.

Fig. 1 shows the discriminator circuit. A positive bipolar pulse at the input is fed through a 50 ohm cable to the junction of R1 and R2. R1 feeds the lower threshold tunnel diode CR1. With the lower threshold control, CR1 can be biased to trigger anywhere from 100mV to 500mV on the leading edge of the input pulse. The L.T. zero trim is adjusted as low as possible consistent with the requirement that the discriminator does not free run in the absence of an input pulse.

Figure 1. The circuit diagram for the fast
zero-crossing discriminator. Better output
operation was achieved with R23 = 2.2K,
R25 = 150 Ω, R29 = 6.8K, and R27 = 1K.

FAST ZERO-CROSSING DISCRIMINATOR

D.A.G.   28/5/67
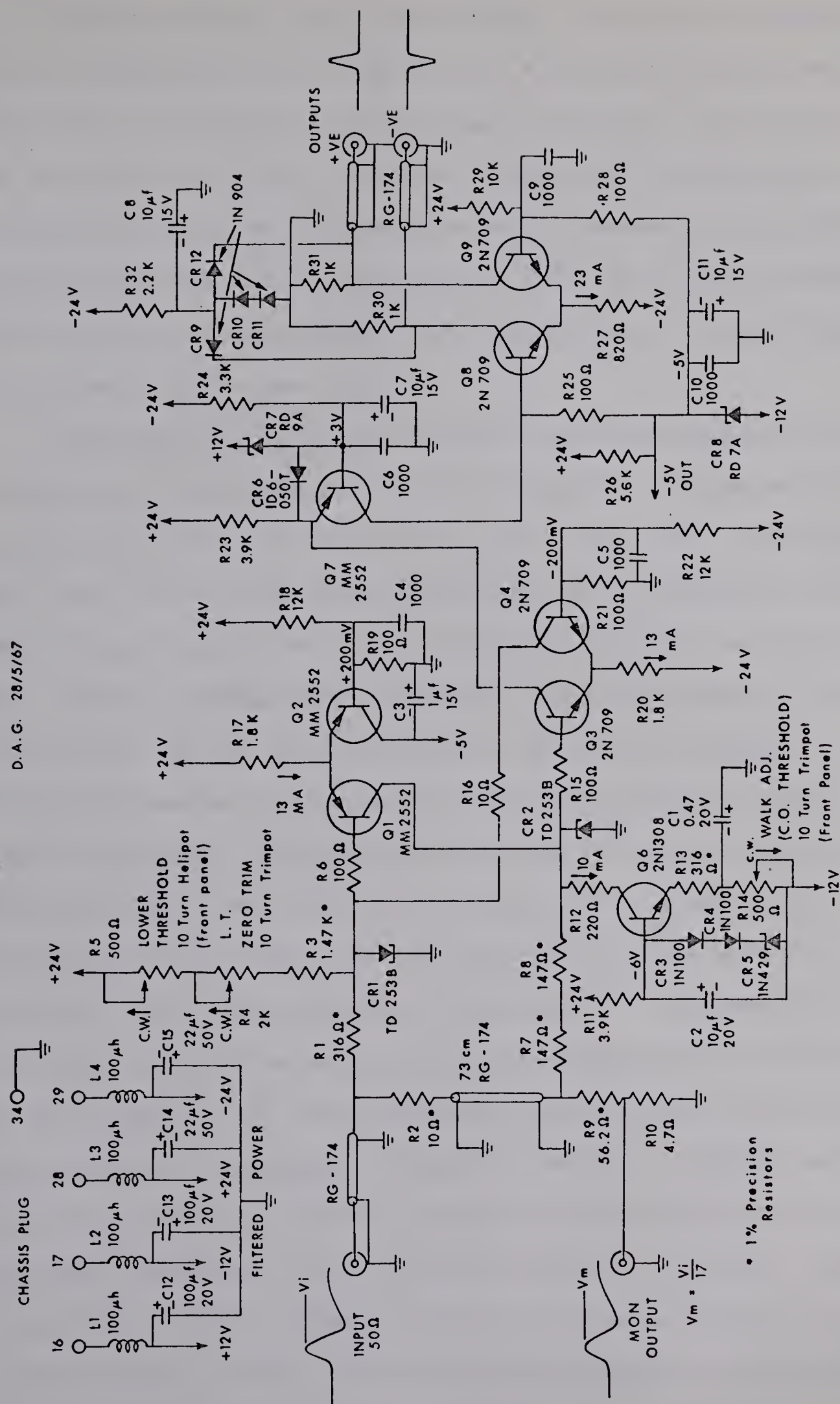
The input pulse is also passed through a 50 ohm delay terminated by the combination of R7, R8, R9 and R10. The zero-crossing tunnel diode CR2 is fed by R7 and R8. Constant current source Q6 biases CR2 at the peak current point. Diode CR3 compensates the base-emitter voltage of Q6 while CR4 provides first order compensation of the temperature variation of the peak current of CR2. R14 is used to adjust the cross-over tunnel diode bias for minimum walk over the amplitude range covered by the input pulse.

Transistors Q1, Q2, Q3 and Q4 form a current gate and reset circuit similar to that designed by C.W. Williams [1]. Transistor Q1 normally conducts 13mA into CR2 preventing the tunnel diode from triggering. When the lower threshold tunnel diode CR1 is triggered to its high voltage state, Q1 is turned off removing the gating current from CR2. CR2 is prevented from triggering by the positive phase of the input pulse. As the input pulse crosses through zero voltage, the bias on CR2 reaches the peak current point and CR2 triggers to the high voltage state. Triggering of CR2 causes the 13 mA current in Q3 to switch to Q4. This causes the resetting of CR1, which in turn, turns on Q1 to reset CR2. The resetting time is of the order of 4 nsec. The short pulse produced at the collector of Q3 passes through Q7 to Q8. Q8 is turned on during this pulse causing the 23 mA flowing in Q9 to switch to Q8. Two complementary current pulses are produced at the outputs. The negative output switches from a quiescent zero mA to -20 mA during the pulse. The positive output switches from a quiescent -20mA level to zero mA for the duration of the pulse. The outputs may be left unloaded or driven into 50 ohm or 93 ohm cables. In the unloaded condition, the 20mA current is caught by either diode

CR9 or CR12. A 1 volt output of roughly triangular shape is produced
on a 50 ohm cable. The rise and fall times are approximately 2 nsec.
and the fwhm is 4 nsec.

Long delay cables are often used in the stop channel of a time-of-flight system to delay the beam pulse time pickoff for arrival after
the start pulse from the neutron detector. The 20mA output current
level was chosen to allow for the large attenuation through such long
delay cables.

The monitor output [1] provides an attenuated version of the input
pulse. The attenuation factor is approximately 17. The monitor output
may be left unloaded when not used.

Fig. 2 shows the walk characteristics of the zero-crossing discriminator. The test circuit is shown in fig. 3. A Tektronix 109 pulser
(600 cps) was used with short charging lines. The output was attenuated and clipped to produce a bipolar pulse with a leading edge to
cross-over time of 1 nsec as shown in figures 2 and 3. The output of
the zero-crossing discriminator triggered a sampling oscilloscope while
the shift of the cross-over point at the monitor output was observed as
a function of pulse height [1,2]. The walk is seen to be within ±65 psec
down to the minimum threshold of 100mV. The walk was not measured above
3.5 volts. Experience with similar types of zero-crossing discriminators
[1,2,3] indicates that the walk is negligible at higher pulse heights.
Consequently, it is anticipated that the walk characteristics should
be good up to 10 volts making this circuit useful for other applications.
Since the discriminator is completely DC coupled and the resetting is
reasonably independent of pulse shape, the circuit may be used for high
counting rates, and wider pulse widths. The minimum pulse pair resolu-

Figure 2. Walk characteristics for the fast
zero-crossing discriminator. The test pulse
had a 1 nsec leading edge to cross-over time.

FAST ZERO - CROSSING
DISCRIMINATOR WALK

INPUT
PULSE
HEIGHT
mV

1.0 n sec

±65 p sec
WALK

10000

1000

100

LATE
TRIGGERING

EARLY
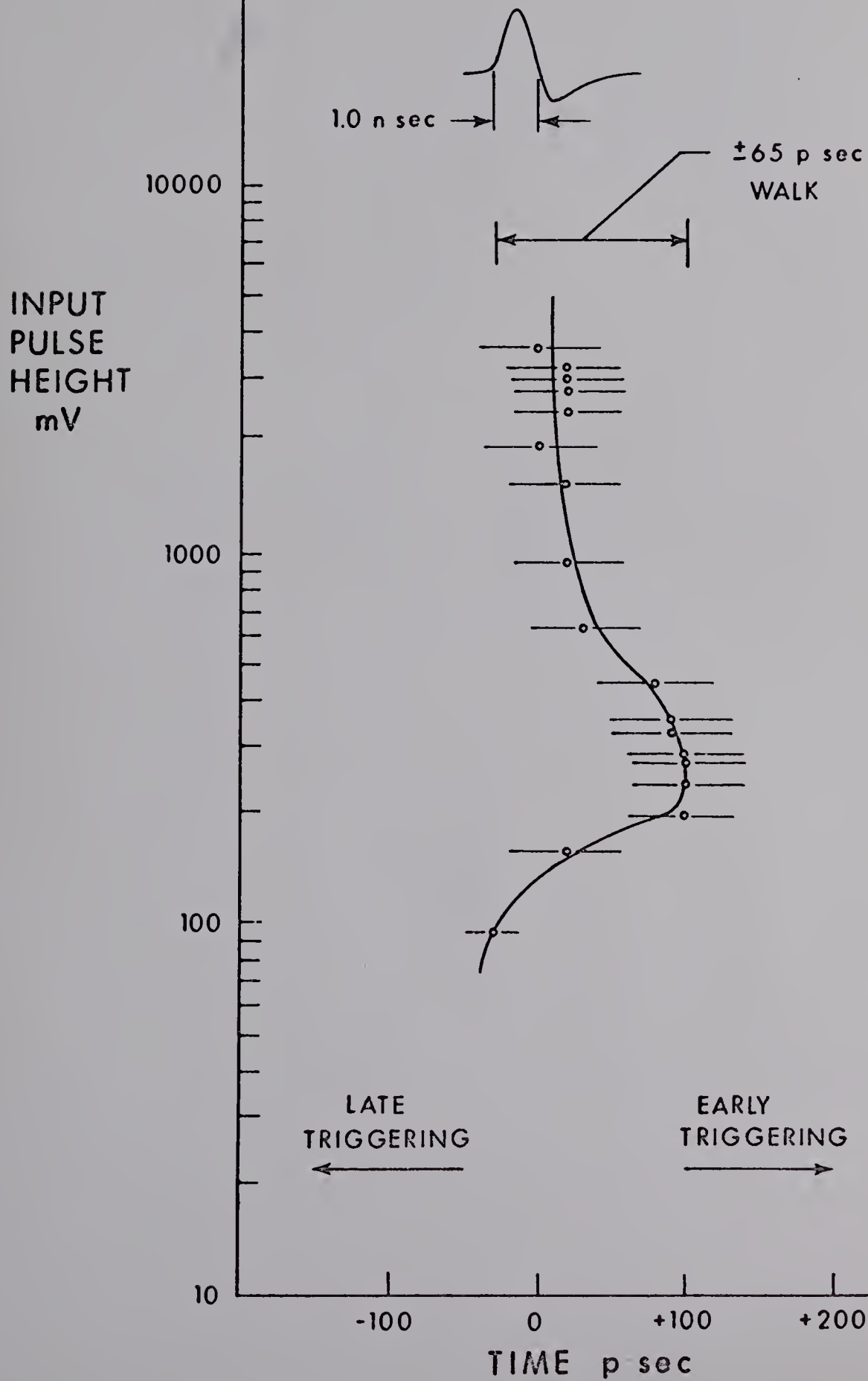TRIGGERING

10

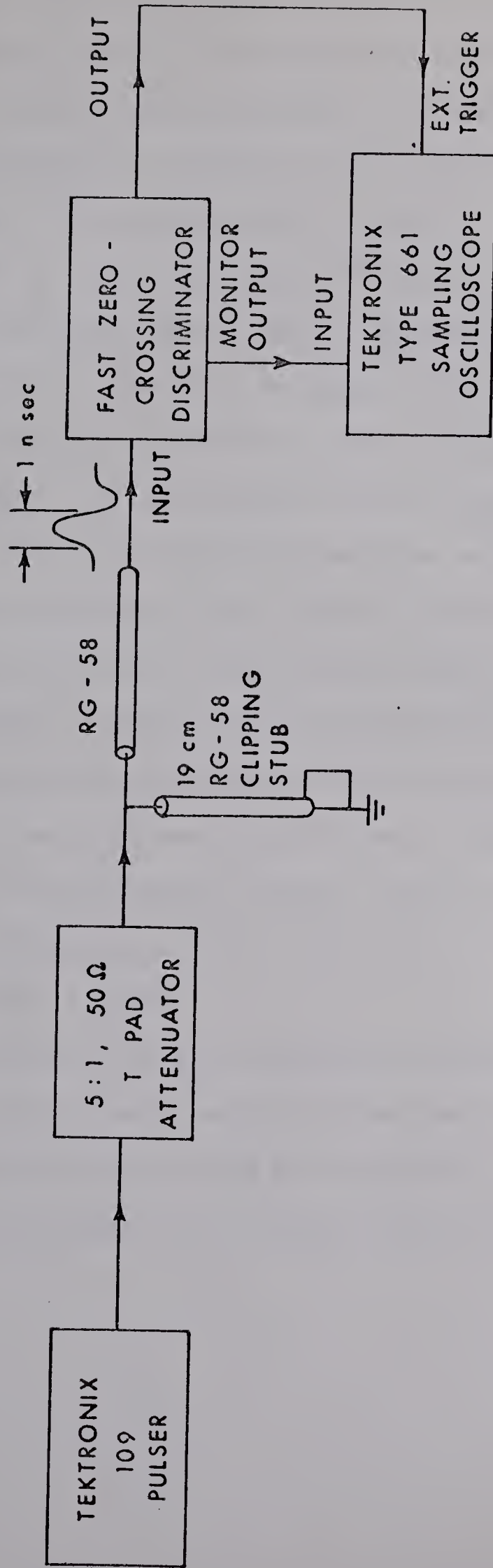-100   0   +100   +200

TIME p sec

Figure 3. Block diagram of the system used
for the walk measurements.

PULSER WALK TEST

tion time when triggering on noise was observed to be 17 nsec.

Fig. 4 shows the system used to test the operation of the discriminator as a pulsed beam time pickoff. A pulsed 4.5MeV proton beam from the University of Alberta Van de Graaff and Mobley bunching system was used. The beam pulse width was 400 ± 50 psec and the repetition rate was 1 MHz. The signal from time pickoff #2 was fed to the control room via a 50 ohm cable. Two Hewlett-Packard fast amplifiers were used. Two 50 ohm attenuators were used to adjust the output of the second amplifier as close as possible to its maximum value ($\simeq$850mV). The discriminator output triggered the sampling oscilloscope. The other time pickoff capacitor output was fed directly to the sampling oscilloscope input. With a 1.5μA average beam current, the timing jitter observed at the cross-over point on the oscilloscope was within 40 psec. The same test was performed with the monitor output of the discriminator providing the input to the oscilloscope. In this mode, the time jitter was within 20 psec. This jitter may be largely due to the oscilloscope trigger, since the operating manual for the 661 oscilloscope specifies a time jitter of "less than 30 psec" for the sweep trigger.

The characteristics of the discriminator as measured above should be more than adequate for present day pulsed beam applications. Experience using the discriminator with the University of Alberta neutron time-of-flight spectrometer has confirmed that the performance is satisfactory.

Figure 4. The system used for the test of the fast zero-crossing discriminator time resolution in operation as a pulsed beam time pickoff.

TEST OF PULSED BEAM PICKOFF
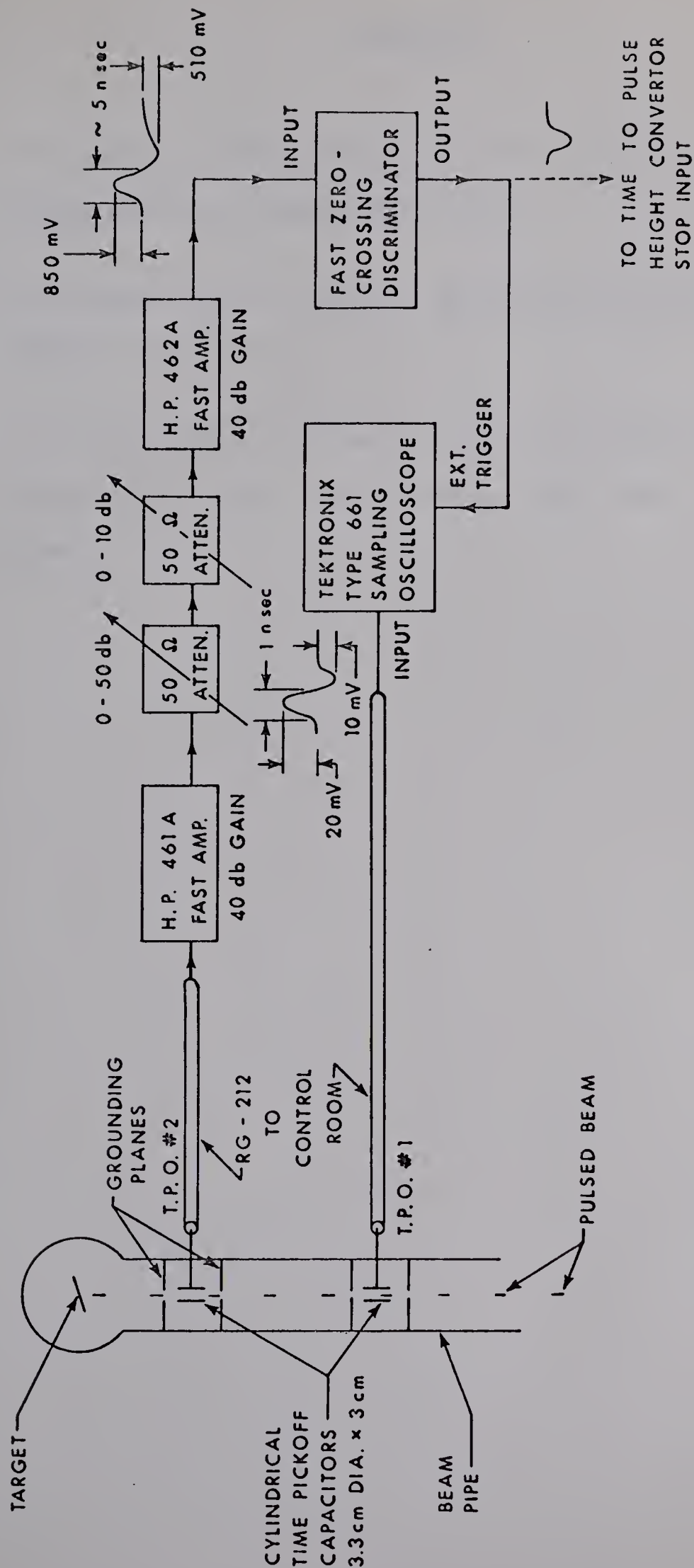
REFERENCES

1) C.W. Williams, ORTEC Instruction Manual, 264 Photomultiplier Timing Discriminator and Preamplifier (1967).

2) D.L. Wieber and H.W. Lefevre, IEEE Trans. Nucl. Sci. NS-13, No. 1 (February 1966) 406.

3) D.A. Gedcke and W.J. McDonald, A Constant Fraction of Pulse Height Trigger for Optimum Time Resolution, Nucl. Instr. and Meth. (in press).

B29878